

# Studying the jet geometry and brightness temperature of BL Lacertae objects observed at 43 GHz

Bachelorarbeit am Lehrstuhl für Astronomie  
von  
Jonas Andreas Walter Ringholz



Fakultät für Physik und Astronomie  
Julius-Maximilians-Universität Würzburg

Würzburg, den 22. Dezember 2014

*Verantwortlicher Hochschullehrer:*

Prof. Dr. M. Kadler



---

## Zusammenfassung

Aktive Galaxien Kerne (AGN) sind von höchstem wissenschaftlichen Interesse insbesondere die in radio-lauten AGN beobachteten extragalaktischen Jets und die Erklärung der hier beobachteten Phänomene. Im Standardmodell der AGN nach [Antonucci \(1993\)](#) wird angenommen, dass sich um das supermassive schwarze Loch einer Galaxie eine Akkretionsscheibe ausbildet. Senkrecht zu dieser bildet sich entlang der Rotationsachse ein Strom aus hoch relativistischen geladenen Teilchen, der als Jet bezeichnet wird. In Folge der Beschleunigung der geladenen Teilchen im Magnetfeld wird Synchrotronstrahlung emittiert. [Blandford & Königl \(1979\)](#) und [Königl \(1981\)](#) formulierten Ende der 1970er und Anfang der 1980er Jahre ein Modell zur Beschreibung der beobachteten Jet-Strahlung.

Das Modell basiert auf der Annahme eines kegelförmigen und frei expandierenden Teilchen-Jets. Sie gehen davon aus, dass sowohl die Magnetfeldstärke als auch die Energiedichte der Elektronen entlang der Jetachse abnehmen und deren Gradienten dabei mit einem Potenzgesetz beschrieben werden können. Dabei gingen [Blandford & Königl \(1979\)](#) von einem Exponenten von  $b = -1$  für die magnetische Feldstärke und für  $n = -2$  für die Elektronenergiedichte aus. [Königl \(1981\)](#) erweiterte das Modell auf variable Exponenten, mit  $-1 > b > -2$  und  $-0.6 > n > -3$ . [Kadler et al. \(2004\)](#) berechnete aus den Annahmen der Modelle das Verhalten des Gradienten der Helligkeitstemperatur  $T_b \propto r^s$ . Der Exponent  $s = l + n + b(1 - \alpha_s)$  setzt sich aus den Exponenten  $l$  für den Gradienten des Durchmessers,  $b$  und  $n$  sowie dem Spektralindex  $\alpha_s$  zusammen.

In der vorliegenden Arbeit wurden die Radiodaten bei 43 GHz für 11 BL Lacertae Objekte hinsichtlich der oben genannten Eigenschaften untersucht. Dafür wurden die Daten der einzelnen Quellen mit kreisförmigen und elliptischen Gausskomponenten modelliert, um die Gradienten des Durchmessers und der Helligkeitstemperatur zu bestimmen. In der Analyse werden die gemessenen Exponenten  $s$  und  $l$  mit den Annahmen von [Blandford & Königl \(1979\)](#) und [Königl \(1981\)](#) verglichen.

Als zentrales Ergebnis der Studie konnte festgestellt werden, dass für alle Quellen des Samples, außer das Objekt 2200+420, welches auf Skalen von  $d_{core} \gtrsim 2$  mas einen signifikant größeren Wert aufweist und separat als individuelle Eigenschaft diskutiert wird, im Rahmen der Unsicherheiten  $l < 1$  gemessen wird. Der mittlere Wert für  $l$  berechnet sich für die studierten Quellen dabei zu  $l \approx 0.91$  und der Median zu  $l \approx 0.78$ . Es lässt sich daraus ableiten, dass extragalaktische Jets auf den beobachteten Skalen stärker kollimiert sind als in den oben genannten Modellen angenommen wurde. Hinsichtlich des Gradienten der Helligkeitstemperatur finden sich drei Quellen (0716+714, 0954+658, 1749+096) im Sample, bei denen unter Berücksichtigung ihrer Streuung Exponenten im Bereich  $s \approx -2.5$  gemessen werden. Alle anderen Objekte, ausgenommen 2200+420, weisen einen Exponenten im Bereich  $-1.4 > s > -3$  auf, wie von [Königl \(1981\)](#) angenommen. Des weiteren zeigen einige Objekte wie zusätzlich zum Potenzverhalten einen Exzess im Gradienten der Helligkeitstemperatur und einen Dip im Gradienten des Durchmessers. Aus einem Vergleich mit Radiodaten bei 15 GHz sowie der Analyse der Kinematik, kann

---

abgeleitet werden, dass der Anstieg der Helligkeitstemperatur an der Position im Jet zu sehen ist, an welcher eine stationäre Komponente beobachtet wird.

Für die Quelle 2200+420 findet sich hinsichtlich der Exponenten  $l$  und  $s$  eine signifikante Abweichung von gemessenen Mittelwerten. Auf größeren Skalen, d.h. für  $d_{core} \gtrsim 2$  mas sind sowohl  $s$  als auch  $l$  etwa einen Faktor 2 steiler. In Übereinstimmung mit Daten bei 15 GHz wird  $l \approx 2.3$  und  $s \approx -4.9$  gemessen. Der Jet öffnet sich auf diesen Skalen also stärker und schneller und kann nicht mit einer kegelförmigen Jetgeometrie beschrieben werden.

---

## Abstract

Active galactic nuclei (AGN) are of utmost scientific interest especially extragalactic jets observed in radio-loud AGN and the explanation of their observed features. In the standard model of AGN according to Antonucci (1993) it is assumed that the supermassive black hole of a galaxy is surrounded by an accretion disc. Perpendicular to this accretion disc a jet of relativistic charged particles is built along the rotation axis. Because the charged particles are accelerated and confined in the magnetic field, synchrotron radiation is emitted. Blandford & Königl (1979) and Königl (1981) presented a model to describe the observed jet radiation. The model is based on the assumption of a conical and free expanding particle jet. It is assumed, that both the magnetic field and the electron energy density decrease along the jet axis. Their gradients can be described by a power law. Blandford & Königl (1979) suppose a power law index of  $b = -1$  for the decrease of the magnetic field and of  $n = -2$  for the electron energy density. Königl (1981) expands the model with respect to variably power law indices with  $-1 > b > -2$  and  $-0.6 > n > -2$ . With these assumptions Kadler et al. (2004) calculated the behavior of the brightness temperature  $T_b \propto r^s$ . The power law index  $s = l + n + b(1 - \alpha_s)$  depends on  $l$  for the diameter gradient,  $b$ ,  $n$  and the spectral index  $\alpha_s$ .

In the current study the 43 GHz radio data of 11 BL Lacertae objects are analyzed. For this reason the data of each individual source were model fitted with circular and elliptical Gaussian components to determine the diameter and brightness temperature gradients. In the study the measured power law indices are compared with the assumptions of Blandford & Königl (1979) and Königl (1981).

The main result of this study is that for all sources of my sample, except 2200+420, which shows a significant greater value and will be discussed as individual feature, the measured  $l < 1$ , when all uncertainties are taken into account. The average value of  $l$  of all studied sources can be calculated to  $l \approx 0.91$  and the median to  $l \approx 0.78$ . From this it can be derived, that extragalactic jets are much more collimated at the observed parsec scales as assumed in the previous models. With respect to the brightness temperature gradient there are three sources (0716+715, 0954+658, 1749+096) with a measured power law index of  $s \approx -2.5$ , when taking the scattering of their data points into account. The other sources, except 2200+420, have measured power law indices in the interval  $-1.4 > s > -3$ , which can be described by Königl (1981). There are also sources such as 0219+428, which show an underlying power law with an excess in the brightness temperature gradient and a dip in the diameter gradient. If one compares this feature with radio data at 15 GHz and an analysis of the jet kinematics, one can derive, that the jet shows an increase of brightness temperature at this position, at which a stationary component can be observed. The source 2200+420 shows with respect to the power law indices  $l$  and  $s$  a significant deviation from the measured averages. At higher scales meaning for  $d_{core} \gtrsim 2$  mas both  $s$  and  $l$  are twice as precipitous. In conformity with data at 15 GHz the values are  $l \approx 2.3$  and  $s \approx -4.9$ . At this scales the jet opens stronger and faster and it is not possible to describe the jet with a conical geometry.



# Contents

<b>1. Scientific context</b>	<b>3</b>
1.1. Active galactic nuclei and jet models	3
1.1.1. Radio loudness	3
1.1.2. Line emission	4
1.1.3. Jet kinematics	5
1.1.4. Fanaroff-Riley classification	6
1.1.5. BL Lacertae objects	7
1.1.6. Unification model	7
1.1.7. Radiative processes	11
1.1.8. Basic jet models	14
1.2. Very long baseline interferometry	18
1.2.1. Radiointerferometry	18
1.2.2. Monitoring programs	21
<b>2. Modeling physical parameters along parsec scale radio jets</b>	<b>23</b>
2.1. Model fitting of VLBI data	23
2.2. Previous studies of brightness temperature gradients in AGN jets	24
2.3. Sample selection and data reduction	24
<b>3. Results</b>	<b>29</b>
3.1. Sample results	29
3.2. Individual source studies	37
3.3. Conclusion and Outlook	46
<b>A. Appendix</b>	<b>47</b>
A.1. Figures	47
A.2. Tables	86
<b>List of Figures</b>	<b>97</b>
<b>List of Tables</b>	<b>103</b>
<b>Bibliography</b>	<b>105</b>
<b>Danksagung</b>	<b>107</b>



# 1. Scientific context

## 1.1. Active galactic nuclei and jet models

Active Galactic Nuclei (AGN) are one of the most luminous objects in our universe. Observation of different wavelengths show, that the radiation emitted from AGN is a broadband spectrum. The first AGN was detected in 1943 by [Seyfert \(1943\)](#) and in the early days of AGN observation the several subclasses of AGN were classified as completely different objects. Nowadays all AGN can be diverted into subclasses, which can be unified in one AGN model.

Within this model it is assumed that AGN are the nuclei of an active galaxy with a supermassive black hole in the center surrounded by an accretion disc of charged particles. According to [Antonucci \(1993\)](#) around the black hole, is also a hot narrow line region (NLR) in a range  $100 - 1000$  pc and a density of  $10^3 - 10^6 \text{ cm}^{-3}$ , which emits a narrow line spectrum, a cold dust torus in a range of  $1 - 10$  pc and a hot broad line region (BLR) in a range of about  $0.01 - 0.1$  pc and a density of about  $10^{10} \text{ cm}^{-3}$ , which emits a broad line spectrum. In some cases the AGN form an extragalactic jet, along the rotation axis of the AGN, perpendicular to the plane of the accretion disc. This jets are streams of high relativistic charged particles, which can reach a length up to megaparsec scales ([Ghisellini \(2011\)](#)).

### 1.1.1. Radio loudness

One first possibility to classify active galactic nuclei is to divide them into sources, which are radio-loud or radio-quiet, meaning that some sources show a higher or lower ratio of their radio flux to optical flux. [Kellermann et al. \(1989\)](#) gave a classification of radio-loud and radio-quiet galaxies with respect to the ratio  $R_{r-o}$  of the radio flux  $S_r$  and the optical flux  $S_o$ .

$$R_{r-o} = \frac{S_r}{S_o} \tag{1.1.1}$$

To separate these two classes, a source can be classified as radio-quiet, if the ratio is:

$$0.1 < R_{r-o} < 1 \tag{1.1.2}$$

and a source is said to be radio loud, if the ratio obtains:

$$R_{r-o} > 10 \tag{1.1.3}$$

Wilson & Colbert (1995) described, that the radiation in the radio-band of radio-quiet galaxies can mostly be explained with thermal radiation, which came from the core of mostly spiral galaxies. If one observes radio loud sources, the radiation in the radio regime can not be explained with thermal radiation as in the case of radio-quiet objects. In this case high resolution radio observations show, that these objects form a jet along the rotation axis of the AGN. Wilson & Colbert (1995) assumed, that the host galaxies of these object are mostly elliptical galaxies. These galaxies arise in consequence of the merger of two single galaxies. The jet is built up of relativistic particles, which are accelerated and confined by a magnetic field. Because of this acceleration the particles, mostly electrons, emit synchrotron radiation, which will be described in section 1.1.7 in detail. According to Sheikhnezami et al. (2012) the particles have their origin in the accretion disc and the jet is formed by several magnetohydrodynamic processes, which are not fully understood in detail yet.

Because of symmetric reasons always two jet are built in a radio-loud AGN one parallel and the other one anti parallel along the rotation axis of the accretion disc. So both are perpendicular to the accretion disc. The jets are aligned by two radio cores, which are optically thick for synchrotron radiation ( $\tau > 1$ ) and emit primarily radiation due to radiative losses caused by inverse Compton scattering.

The shape of a jet is defined with respect to Bridle & Perley (1984) as a feature, which is in minimum one part wide and four parts long. The length can range up to megaparsec scales (Ghisellini (2011)).

### 1.1.2. Line emission

Another distinctive feature of AGN is the different emission spectrum of several AGN types. There are AGN, which show both narrow and broad emission lines and there are types of AGN, which only show narrow emission lines. In some cases these objects show broad emission lines, when the observation is done with a specific polarization illustrated by Antonucci & Miller (1985).

It is assumed that the broad lines in the spectrum are the consequence of the emission in a very dense and hot gas with a density up to  $d \approx 10^9 \text{cm}^{-3}$  (Sulentic et al. (2000)). The forbidden narrow line spectrum is assumed by Sulentic et al. (2000) to be emitted in a very low dense gas, because the forbidden lines are the consequence of electric quadrupole transitions, which can only occur in very low dense gases with a density of  $10^3 \text{cm}^{-3} < d < 10^6 \text{cm}^{-3}$ .

If a source does not show broad lines, this means that the region, in which the emission proceeds is covered by another medium. In AGN this medium is a dust torus, which is shown in figure 1.3. This dust torus absorbs the most intensity of the broad emission lines and also much of the continuum radiation and only the narrow lines appear in the

line of sight. So the narrow line region has larger distance to the black hole than the dust torus.

### 1.1.3. Jet kinematics

If one observes an extragalactic jet with VLBI resolution in the radio regime, one can identify individual emission regions. These components can move in time along the jet axis. Observing a source over several years allows to track the components for this time and the projected distance this individual emission region moved outwards during this period can be calculated. If one knows the redshift of the source, in addition the covered distance can be calculated with  $x = \theta r$ , where  $\theta$  is the angle between the jet axis and the line of sight. With that the apparent speed  $\beta_{app}$  of the jet can be computed. In much cases the observed speed is multiples of the speed of light. This phenomenon is called apparent superluminal motion. This is an projection effect and can be explained by arguing, that the angle between the jet axis and the line of sight is small and the components of the jet move with a speed close to the speed of light. If a component emits light at one point of the jet and moves forward in the jet and emits also radiation, this radiation will arrive only a bit later as the light from the first point, because the emitting particles move with almost the same speed as the emitted photons. If this motion is projected on the sky plane, the speed seems to be higher than the speed of light. If the speed  $\beta_{app}$  of the superluminal motion and the angle  $\theta$  is known, the real speed  $\beta$ , in units of  $c$ , of the jet can be calculated in terms of Robson (1996) with equation 1.1.4:

$$\beta_{app} = \frac{\beta \sin \theta}{1 - \beta \cos \theta} \quad (1.1.4)$$

Another feature in the jet kinematic is the relativistic boosting respectively Doppler boosting. The effect explains, that in some radio-loud AGN especially blazars only one jet is visible and the other jet, the counterjet, vanishes, because it is deboosted. This effect is the consequence that the particles move relativistic, so their emitted flux is effected by relativistic time dilatation. The result is that the observed flux  $S_o$  is energy boosted in respect to that flux emitted in a rest frame  $S_e$ . Robson (1996) calculates the boosting in equation 1.1.5

$$S_o = S_i [\gamma(1 - \beta \cos \theta)]^{-3} \quad (1.1.5)$$

Where  $\gamma = (1 - \beta^2)^{-1/2}$  is the Lorentz factor. If one takes also the spectral energy distribution in to account, the equation 1.1.6 for the ratio of the flux of approaching (jet) and receiving (counter jet) jet becomes the following shape:

$$R = \left( \frac{1 + \beta \cos \theta}{1 - \beta \cos \theta} \right)^{(2-\alpha)} \quad (1.1.6)$$

Here  $\alpha$  is the spectral index. If the conterjet is deboosted this much, it is possible that

the incident flux of the counterjet is as high as the background noise of the observing telescopes. So the counterjet does not appear in the VLBI data.

#### 1.1.4. Fanaroff-Riley classification

The Fanaroff-Riley-Classes, which firstly were described by [Fanaroff & Riley \(1974\)](#), are classes of radio loud AGN and a subclass of radio galaxies. Radio galaxies are radio-loud AGN, with a very large angle between jet axis and line of sight. Object classified as Fanaroff-Riley 1 objects are radio galaxies, where the flux distribution of the jet is dominated by the core of the jet. Furthermore, the jets are relative broad and the jets dissipate in so called plumes at the end of the jets as one can see in figure 1.1.

Fanaroff-Riley 2 objects are distinguished by FR1 objects by a lobe dominated emission, which in the most cases emerge in consequence of a shock, when the particle jet hits the intergalactic medium. The jet of Fanaroff-Riley 2 galaxy is a narrow collimated one as shown in figure 1.2.

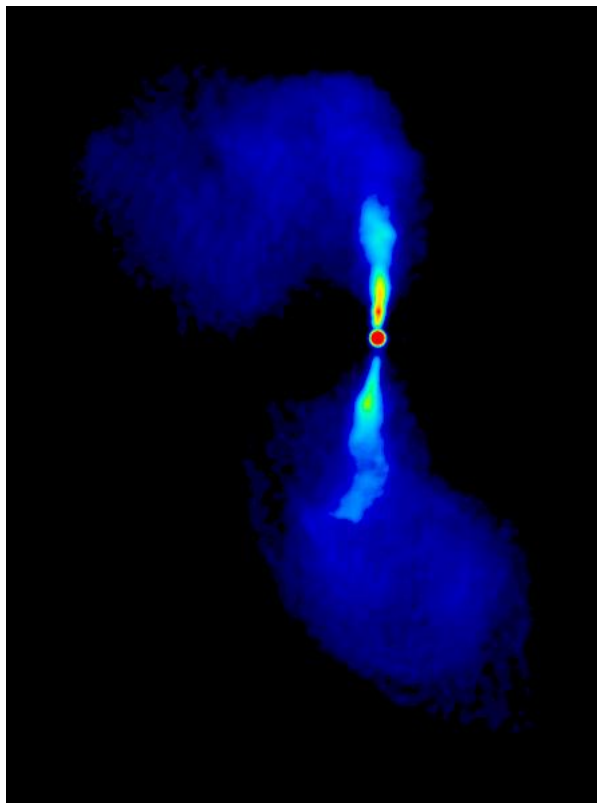


**Figure 1.1.:** The figure shows the Fanaroff Riley Class 1 object 3C 272P1 observed with the VLA at a wavelength of 6 cm. The data were imaged by [Laing & Bridle \(1987\)](#). Here the red color describes high flux and blue one low flux. One can regard the high flux in the core (red) and the plumes at the end of the jet (blue)

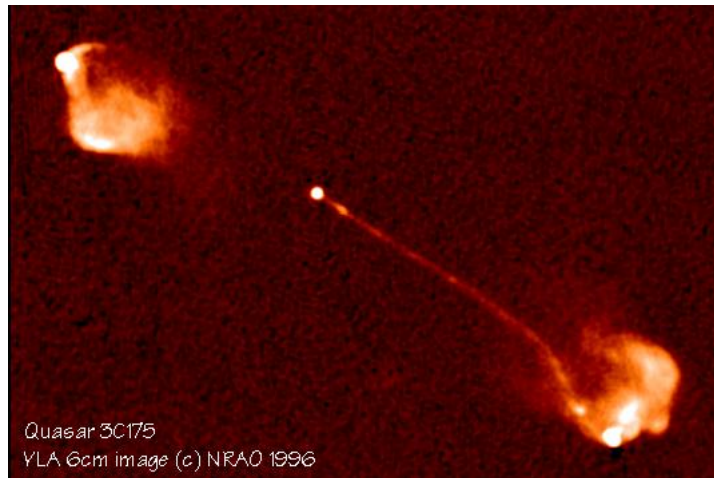


**Figure 1.2.:** The figure shows the Fanaroff Riley Class 2 object 3C 175 observed 1996 with the VLA at a wavelength of 6 cm and a resolution of 0.35 arcsec. Image courtesy of NRAO/AUI and investigated by [Bridle et al. \(1994\)](#). One can regard the bright lobes at the end of the jet and one narrow jet

### 1.1.5. BL Lacertae objects

BL Lac objects are sources, which are radio-loud in terms of [Kellermann et al. \(1989\)](#). These sources show neither narrow lines nor broad lines in their spectrum. The spectra of BL Lac objects are continuous spectra, which are normally relatively flat and do not show other features. The major part of the electromagnetic spectrum follows a power law. Some sources, classified as BL Lacs, show some small emission lines. Based on this emission lines, one can figure out that these objects are indeed extragalactic because of their redshifted emission lines. With respect to [Stein et al. \(1976\)](#) most of these sources show high variability and polarization behavior in the most parts of their electromagnetic spectrum. A significant feature is, that these objects only show one jet, which is Doppler boosted in the direction of observation. The counter-jet is not visible, because of Doppler deboosting in the other direction as explained in section 1.1.3. This means BL Lac objects are sources with a jet, which is pointed almost in our direction and the source is seen under a small angle with respect to the jet axis. Hence some BL Lacs occur as compact point-sources.

According to [Stein et al. \(1976\)](#) there are also X-ray selected BL Lac objects, which show BL Lac attributes in the X-ray band.

### 1.1.6. Unification model

All classes of AGN can be united in one unification model. The concept of this model is illustrated in figure 1.3 and the different types of AGN with their characteristics are listed in table 1.1 as described by [Urry & Padovani \(1995\)](#). For the following description

I follow the portrayal of [Antonucci \(1993\)](#). The characteristics, observed in all types of AGN, is the fact that all AGN are built up of a supermassive black hole, that is orbited by an accretion disc at a distance of  $r \approx 10^{-3}$  pc. [Antonucci \(1993\)](#) argues also, that the disc has a density of about  $n \approx 10^{15} \text{ cm}^{-3}$ . Around the accretion disc in a range of 0.01 – 0.1 pc to the black hole, the broad line region (BLR), can be located. This is a gas cloud with a particle density of  $n \approx 10^{10} \text{ cm}^{-3}$ . A cold dust torus next to the broad line region in a distance of 1 pc to a few 10 pc can also be seen. The torus has a density of  $n \approx 10^3 - 10^6 \text{ cm}^{-3}$ . The last region within this model is the hot narrow line region (NLR) pictured also in figure 1.3. The distance to the black hole is about 100 – 1000 pc and the particle density  $n \approx 10^3 - 10^6 \text{ cm}^{-3}$ . The low density allows the forbidden electron transition in gas atoms, which leads to the forbidden narrow emission lines.

Now there are three distinctive features for AGN. The first is the radio loudness of AGN, the second the luminosity and the other is the angle between the jet axis and the line of sight.

If one has a look at radio quiet sources in terms of [Kellermann et al. \(1989\)](#) there are on the one hand the Seyfert galaxies, which have a low luminosity and on the other hand the Quasi-stellar objects (QSO) with a high luminosity. As one can see in table 1.1 these two AGN types can additionally be distinguished in respect of their emission behavior. Seyfert 2 galaxies and QSO Type 2 have only narrow emission lines, meaning the angle between the jet axis and the line of sight is of a high magnitude and the dust torus covers the broad line region. Seyfert 1 galaxies and QSO Type 2 objects possess both narrow and broad line emission lines. These objects are observed under a smaller angle and the torus do not cover the BLR.

The radio loud object can also be distinguished in almost the same way as the radio quiet ones as one can recognize in table 1.1 and in figure 1.3. The best way to explain these individual classes of radio-loud AGN is to start at large angle between jet axis and line of sight and go to smaller angles. Under a large angle, the BLR is not visible, and one sees a narrow line radio galaxy (NLRG), which can additionally be differentiated in luminosity and their radio morphology as discussed before. That is the analogue to the Seyfert 2 galaxies and the QSO type 2. If an object is observed under a smaller angle, the BLR is visible. These objects are called broad line radio galaxies (BLRG), which can also be differentiated in luminosity and their radio morphology. These are the analogue to the Seyfert 1 galaxies and the QSO Type 1. If one observes a source at very small angles, these objects are classified as Blazars and appear as compact unresolved objects. Blazars can also be differentiated in BL Lac objects, which show no emission lines as discussed before and flat spectrum radio quasars (FSRQ) showing both broad and narrow line emission and have also a higher luminosity as BL Lacs.

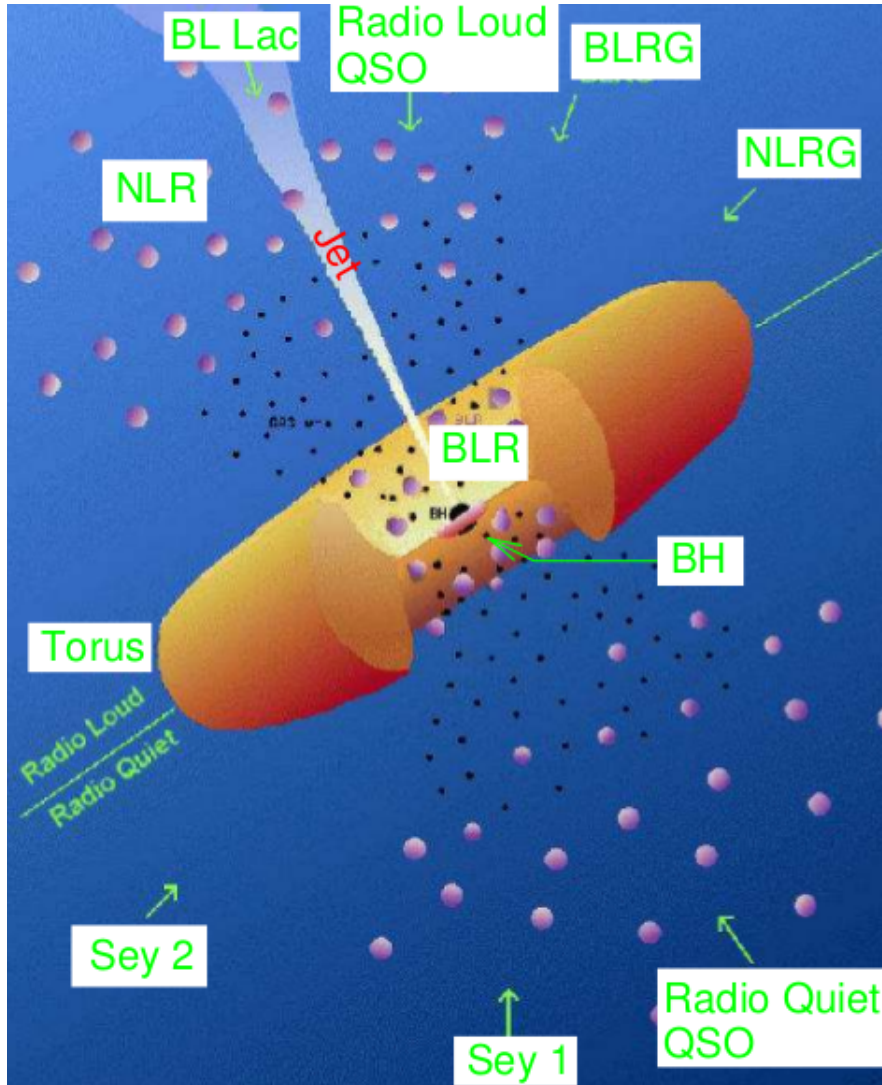


**Figure 1.3.:** shows the Unification model by Urry & Padovani (1995) with modifications from Matthias Kadler. The upper part illustrate the case of a radio loud AGN and the lower side shows a radio quiet AGN. Here BH is the black hole, BLR is the broad line region, NLR means the narrow line region, Sey1 and Sey2 are the Seyfert 1 and Seyfert 2 galaxies, BLRG and NLRG are the broad line and narrow line radio galaxies

**Table 1.1.:** Overview: Unification Model AGN, by M. Kadler. Here RQ means radio-quiet and RL radio-loud. B stands for broad lines and N for narrow lines.

Type	Radio Loudness	Emission Lines	Luminosity	Jets	Radio Morphology
Seyfert 1	RQ	B+N	Low	No	-
Seyfert 2	RQ	N	Low	No	-
QSO Type 1	RQ	B+N	High	No	-
QSO Type 2	RQ	N	High	No	-
BLRG	RL	B+N	Low	Yes	FR1
	RL	B+N	High	Yes	FR2
NLRG	RL	N	Low	Yes	FR1
	RL	N	High	Yes	FR2
BL Lac	RL	-	Low	Yes	Compact
FSRQ	RL	B+N	High	Yes	Compact

### 1.1.7. Radiative processes

Since in extragalactic jets many radiative processes are present it is necessary to understand basic concepts first. Therefore in this section different radiative processes will be discussed. The most relevant process for my study are synchrotron losses due to charged particles being accelerated in the magnetic field of the jet. Close to the radio core radiative losses due to inverse Compton scattering become relevant and have to be considered. In section 1.1.8 I will introduce the jet models by Blandford & Königl (1979) and Königl (1981), modeling the broadband spectrum from AGN jets.

**Synchrotron Radiation** Synchrotron radiation is emitted by charged relativistic particles, which are accelerated in a magnetic field.

To describe the accomplishment of synchrotron radiation, I follow the argumentation of Rybicki & Lightman (1979).

In conclusion with the assumption that  $|\vec{v}| = \text{const}$  and there is no acceleration parallel to the magnetic field, the acceleration perpendicular to the magnetic field follows from equation 1.1.7:

$$\frac{d\vec{v}_\perp}{dt} = \frac{q}{cm\gamma} \vec{v}_\perp \times \vec{B} \quad (1.1.7)$$

The solution of this equation is a circular motion in the plane perpendicular to the magnetic field with the rotation frequency  $\omega_B$  respectively the centripetal acceleration  $a_\perp$ :

$$a_\perp = \omega_B v_\perp = \frac{\omega_L v_\perp}{\gamma} = \frac{qBv_\perp}{\gamma mc} \quad (1.1.8)$$

Here  $\omega_L = \frac{qB}{mc}$  is the Larmor frequency. Using Larmors Formula for relativistic particles, one can calculate the total power, emitted by one single electron:

$$P = \frac{2q^2\gamma^4}{3c^2} (a_\perp^2 + \gamma^2 a_\parallel^2) = \frac{2q^4\gamma^2 B^2}{3c^5 m^2} v_\perp^2 \quad (1.1.9)$$

Under the assumption of an isotropic velocity distribution with respect to the angle between the magnetic field and the and the velocity direction, the computation leads to equation 1.1.10:

$$P = \frac{4}{3} \sigma_T c \beta^2 \gamma^2 U_B \quad (1.1.10)$$

In this equation  $\sigma_T = \frac{8\pi q^4}{3m^2 c^4}$  is the Thomson cross section and  $U_B = B^2/8\pi$  the magnetic field energy density. One can note that in the Thomson cross section the mass is squared in the denominator, meaning only particles with small mass can regarded in first order for the jet model. So only light particles like electrons were considered. There are also other models, which include also hadronic particles as in the model by

Mannheim (1993). For the following the assumptions of Königl (1981) hold and only leptons are considered.

Because we consider relativistic particles, the radiation is beamed in the direction of the velocity  $v_{\perp}$  in the shape of a cone. These conical radiation has an opening angle of  $\theta = \frac{1}{\gamma}$ . Like one can see in figure 1.4 the observer registered a doppler shifted radiation pulses with a length of  $\tau = \frac{1}{\gamma^2 \omega_L}$ . For this short pulse follows with respect to Heisenbergs uncertainty relation a broad band emission spectrum with a peak at the characteristic frequency of  $\omega_c = \frac{1}{\tau} = \gamma^2 \omega_L$ .

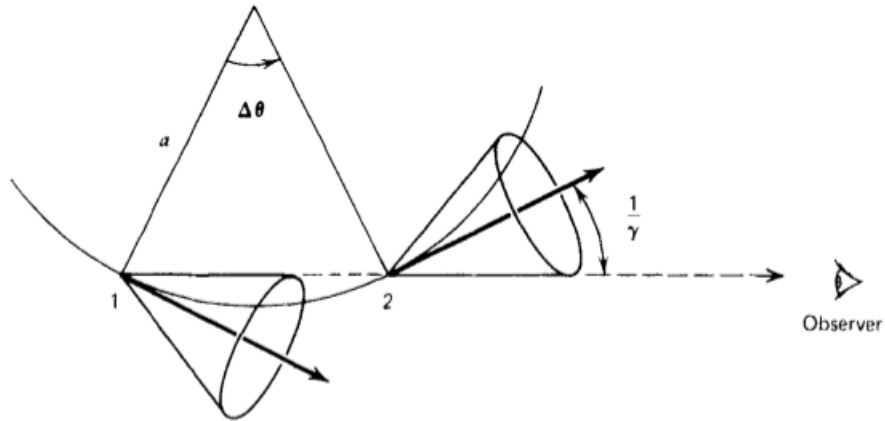


**Figure 1.4.:** Figure 6.2. from Rybicki & Lightman (1979), beamed radiation of synchrotron radiation

To get the spectrum, which is emitted by all electrons of one jet one must know the distribution  $n_e(\gamma)$  of electrons. For the known energy distribution the total spectrum can be computed out of the one electron spectrum:

$$P_{\nu} = \int_1^{\infty} P_{\nu}(\gamma) n_e(\gamma) d\gamma \quad (1.1.11)$$

The electrons can have different origins. At the one hand the electrons can be subject of a thermal distribution. The other case, which is of much more relevance is the non thermal distribution, which means that the electron distribution  $n_e(\gamma) \propto \gamma^{-p}$  follows a power law. So the spectrum can be written in form of equation 1.1.12

$$P_{\nu} = \int_1^{\infty} P_{\nu}(\gamma) n_0 \gamma^{-p} d\gamma \quad (1.1.12)$$

The next assumption is that the spectrum of one single electron, which has a special velocity, is given as the power of one electron computed in equation 1.1.10. The expansion to the following equation is, that this power depends now on a frequency and velocity depending distribution function  $\Phi_{\nu}(\gamma)$ . This function is normalized over all frequencies. The spectrum gets the form of equation 1.1.13:

$$P_\nu(\gamma) = \frac{4}{3}\sigma_T c \beta^2 \gamma^2 U_B \Phi_\nu(\gamma) \quad (1.1.13)$$

Now one can make the approximation that the electrons emit only at their characteristic frequency  $\omega_c$  as calculated before. The distribution function becomes the shape of a delta-function  $\Phi_\nu(\gamma) = \delta(\nu - \gamma^2 \nu_L)$ . For this assumption the spectrum of synchrotron radiation can finally be computed to the following equation:

$$P_\nu = \frac{2c\sigma_T n_0 U_B}{3\nu_L} \left( \frac{\nu}{\nu_L} \right)^{-\frac{p-1}{2}} \quad (1.1.14)$$

The power law index in equation 1.1.14 is the spectral index  $\alpha = \frac{p-1}{2}$ . So if one assumes a power law distribution for the energy of electrons also the spectrum of the synchrotron radiation follows a power law.

**Inverse Compton effect** The inverse Compton effect describes the scattering of a photon with a relativistic electron. In this process the photon gets the most of the energy of the scattered electron. The photon is almost emitted in the electrons direction of motion. The scattered electron must possess an energy of  $E \ll m_0 c^2$ . Here  $m_0$  is the rest mass of an electron. If the energy of the photons apply to  $h\nu E \ll (m_0 c^2)^2$  (Klein-Nishina regime) the energy loss of the electrons becomes the following (Rees (1967)):

$$-\frac{dE_c}{dt} = c\sigma_T \epsilon_{rad} \left( \frac{E}{m_0 c^2} \right)^2 \quad (1.1.15)$$

Here  $\sigma$  is the Thomson cross section,  $h$  the Planck constant and  $\epsilon_{rad}$  the energy density of the primary radiation. If one consider photons with energies of  $h\nu E \gg (m_0 c^2)^2$  (Thomson regime) the form of the equations changes to the following (Rees (1967)):

$$-\frac{dE_c}{dt} = \frac{3}{8}c\sigma_T \int \epsilon_{rad}(\nu) \left( \frac{m_0 c^2}{h\nu} \right)^2 \log \left( \frac{2Eh\nu}{m_0^2 c^4} + \frac{1}{2} \right) d\nu \quad (1.1.16)$$

The origin photons for the inverse Compton scattering can on the one hand be primeval black body radiation of the the galactic background radiation and on the other hand synchrotron radiation, which is produced in an extragalactic jet. So the relativistic electrons produce synchrotron photons and can also do inverse Compton scattering with these photons. This process can be repeated frequently in some cases, especially if the electron density is high enough. Such a case of a region with a high electron density is the radio core of an extragalactic jet, which is assumed to be optical thick to synchrotron radiation, meaning all synchrotron radiation, which is produced in this region is scattered in consequence of the inverse Compton effect. Because of the high electron density, this scenario can proceed several time. This circumstance leads to the inverse Compton catastrophe, which is required to explain high brightness temperatures, which will be

explained next.

The brightness temperature is the assumed temperature of an observed source at a specific frequency, which the source would have if it is supposed to be a black body. For a study with the Very Long Baseline Array (VLBA) [Kovalev et al. \(2005\)](#) gave an expression to calculate the brightness temperature for VLBI resolutions. The expression is given by equation 1.1.17:

$$T_b = \frac{2 \ln 2 S_{core} \lambda^2 (1+z)}{\pi k_B \theta_{maj} \theta_{min}} \quad (1.1.17)$$

In this equation  $S_{core}$  is the flux of one model fitted VLBI component (core), which is explained in section 2.1.  $\theta_{maj}$  and  $\theta_{min}$  are the full width at half maximum (FWHM) of one elliptic Gaussian VLBI component along the major and minor axes, which is also explained in chapter 2.1.  $k_B$  is the Boltzmann constant,  $z$  is the redshift of the source and  $\lambda$  the observed wavelength.

In the following chapters only the brightness temperature distribution of synchrotron radiation should be taken into account. [Kellermann & Pauliny-Toth \(1969\)](#) gave an upper limit for brightness temperature, which can be the consequence of synchrotron radiation. The upper limit ranges between  $10^{11} \text{K} < T_b < 10^{12} \text{K}$ . Higher brightness temperatures, which are also measured in my analyzed data are in most cases originated to the core region of the sources. This effect can be explained by the inverse Compton catastrophe.

[Kellermann & Pauliny-Toth \(1969\)](#) give a relation between the ratio of inverse Compton intensity and synchrotron intensity and the ratio of the radiation and magnetic energy density. This can be written in terms of the maximum observed brightness temperature  $T_{max}$ .

$$\frac{L_C}{L_S} = \frac{1}{2} \left( \frac{T_{max}}{10^{12} \text{K}} \right)^5 f_c \left( 1 + \frac{1}{2} f_c \left( \frac{T_{max}}{10^{12} \text{K}} \right)^5 \right) \quad (1.1.18)$$

Here  $f_c$  is the characteristic cutoff frequency of the radio spectrum measured in MHz. It is in the regime of  $f_c \approx 10^{5 \pm 1}$ . So one can note, that if  $T_{max}$  is between  $10^{11} \text{K}$  and  $10^{12} \text{K}$  synchrotron and inverse Compton losses are in the same magnitude. If  $T_{max}$  is much higher than  $10^{12} \text{K}$  the inverse Compton losses become catastrophic.

### 1.1.8. Basic jet models

In the discussion about my data later on, the results shall be discussed with respect to the following jet models. [Blandford & Königl \(1979\)](#) consider a narrow conical jet with an half opening angle of  $\varphi$  and the axis of the jet has an angle of  $\theta$  towards the line of sight. The velocity  $\beta_j$  is constant throughout the whole jet. They also assume, that the magnetic field has only a magnetic field perpendicular to the jet axis, which follows a power law along the jet axis with  $B \propto r^{-1}$ . Electrons can be ejected continuously and

emit synchrotron radiation with a spectral index of  $\alpha = 0.5$ . Furthermore they argue that there is a thermal equilibrium and so the electron energy density  $N$  is in equipartition with the magnetic energy density. Under this assumptions one can calculate that the energy density of the electrons follows also a power law. The electron energy density is given in equation 1.1.19:

$$N = k_e \Lambda \frac{B^2}{8\pi} = \frac{k_e \Lambda}{8\pi} B_0^2 r^{-2} = N_0 r^{-2} \quad (1.1.19)$$

Where  $k_e$  is a constant  $< 1$ ,  $r$  is the radio core distance and  $\Lambda = \ln(\gamma_{e\max}/\gamma_{e\min})$ . With the maximal ( $\gamma_{e\max}$ ) and minimal ( $\gamma_{e\min}$ ) lorentz factor of the considered electrons. König (1981) expands this assumptions in this way, that the magnetic field has also a component parallel to the jet axis, that follows a power law with power law index -2. Meaning the power law index of the whole magnetic field varies between  $-1 > b > -2$ . He also predicted that the power law index of the electron energy density has the following relation if the spectral index is set to  $\alpha_s = 0.5$ :

$$n = -\frac{17 + 7b}{5} \quad (1.1.20)$$

The consequence is the variation of  $n$  between  $-0.6 > n > -2$ . He predicted also that the spectral index for synchrotron radiation  $\alpha_s$  ranges between  $0 > \alpha_s > -1$ .

Königl (1981) calculated the spectrum of an unresolved conical jet. For the calculations for the jet he computed the smallest distance at which optical thin synchrotron radiation with  $\alpha_s = \alpha_0$  can be observed. Setting  $\alpha_0 = -0.5$  the distance can be calculated to:

$$r_M \approx [1.6 \cdot 10^6 D_j^{-1} (\gamma_j \beta_j)^{-6} K_1 B_1^{11} \varphi \csc \theta]^{1/(-11b-n-7)} \text{pc} \quad (1.1.21)$$

Where  $B_1$  is constant with respect to the magnetic field and  $b$  is the power law index for the magnetic field.  $K_1$  is the constant of proportionality in the power law of electron energy density and  $n$  the power law index.  $D_j$  here is the Doppler factor. Also the frequency of the radiation, which is emitted at the distance  $r_M$  can also be calculated for a spectral index  $\alpha_0 = -0.5$ :

$$\nu_{sM} \approx 6.9 \cdot 10^7 (1+z)^{-1} [(1.6 \cdot 10^6 K_1 \varphi \csc \theta)^{-3b-2} D_j^{-8b-n-5} (\gamma_j \beta_j)^{-4b-2n-2} B_1^{-(3n+1)}]^{1/(-11b-n-7)} \text{Hz} \quad (1.1.22)$$

Now König (1981) computed in equation 1.1.23 the flux density of an unresolved jet, meaning in the jet especially in the outer regions no small flux features can be resolved.

$$S_{ob}(\nu) = \frac{(1+z) D_j^2}{4\pi D_l^2} \int_{r_{min}}^{r_{max}} \epsilon \left[ \frac{(1-z)\nu}{D_j} \right] \pi (r\varphi)^2 dr \quad (1.1.23)$$

Here  $D_l$  is the luminosity distance to the source and  $D_j$  is the Doppler factor. The emissivity of the electrons follows from the assumption of power law distributed electrons

with  $N(\gamma_e) = K_e \gamma_e^{-(-2\alpha_e+1)}$ :

$$\epsilon \left[ \frac{(1-z)\nu}{D_j} \right] = (1+z)^{\alpha_e} D_j^{-\alpha_e} \nu_s^{\alpha_e} C_1(\alpha_e) K_e B^{1-\alpha_e} \quad (1.1.24)$$

Where  $\alpha_e = \alpha_s - 0.5$  is the power law index of the injected electrons. The constants of this equation were calculated by [Blumenthal & Gould \(1970\)](#). With these assumptions [Königl \(1981\)](#) calculated the synchrotron spectrum of the unresolved jet, which is given by equation 1.1.25

$$S_{obs}(\nu_s) = \begin{cases} S_{obs}(\nu_{sM})(\nu_s/\nu_{sM})^{\alpha_{s1}} & \nu_{sM}(r_u/r_M)^{-k_m} \lesssim \nu_s \lesssim \nu_{sM} \\ S_{obs}(\nu_{sM})(\nu_s/\nu_{sM})^{\alpha_{s2}} & \nu_{sM} \lesssim \nu_s \lesssim \nu_{sM}(r_u/r_M)^{k_b} \end{cases} \quad (1.1.25)$$

Where  $k_m = ((3 - 2\alpha_e)b + 2n + 2)/(2\alpha_e - 5)$ ,  $k_b = -(3b + 2)$ ,  $\alpha_{s1} = (4 - b - 5k_m)/(2k_m)$  and  $\alpha_{s2} = -\alpha_0 + k_s/k_b$ . [Königl \(1981\)](#) consider also the special case of the flux density at the frequency  $\nu_{sM}$ . Therefor he introduced the short cut  $k_s = -(1 - \alpha_0)b - n - 3$ . The flux density becomes the shape of equation 1.1.26:

$$S_{obs}(\nu_{sM}) \approx 3 \cdot 10^4 [C_1(-\alpha_0)/C_1(-0.5)] (1+z)^{(1+\alpha_0)} D_{l9}^{-2} D_j^{(2-\alpha_0)} \varphi^2 K_1 B_1^{(1-\alpha_0)} \nu_{sM}^{\alpha_0} r_M^{-k_s} / k_s \text{ Jy} \quad (1.1.26)$$

With respect to this assumptions of the models [Kadler et al. \(2004\)](#) expand the model of [Blandford & Königl \(1979\)](#) and [Königl \(1981\)](#) to a expression for the behavior of the brightness temperature gradient of an extragalactic jet. He calculated with these assumption, that also the brightness temperature gradient follows a power law:

$$T_b \propto r^s \quad (1.1.27)$$

With  $s < 0$ . If one assumes an optical thin synchrotron radiation with  $j_\nu \propto n_e B(\nu/\nu_B)^\alpha$  and a constant Lorentz factor, the power law index  $s$  can be determined to:

$$s = l + n + b(1 - \alpha_s) \quad (1.1.28)$$

Here  $\alpha_s$  is the spectral index of the assumed synchrotron radiation.  $l$  is the power law index, which describes the power law behavior of the diameter gradient.  $b$  is the power law index with respect to the magnetic field and  $n$  is the index with respect to the electron energy density. All values are defined negative except  $l$ . These several power laws can be written as shown in equation 1.1.29

$$D \propto r^l \quad B \propto r^b \quad N \propto r^n \quad (1.1.29)$$

Here  $D$  is the diameter,  $B$  the magnetic field and  $N$  the electron energy density. Now

one can compute the canonical value of  $s$  with respect to the restrictions of [Blandford & Königl \(1979\)](#) and [Königl \(1981\)](#), which gave different values for  $l$ ,  $b$ ,  $n$  and  $\alpha_s$  as discussed before. All canonical values are shown in table [1.2](#).

**Table 1.2.:** The canonical values of [Blandford & Königl \(1979\)](#) and [Königl \(1981\)](#) and the expansion with respect to brightness temperature by [Kadler et al. \(2004\)](#)

Power law index	<a href="#">Blandford &amp; Königl (1979)</a>	<a href="#">Königl (1981)</a>
$\alpha$	-0.5	$0 \geq \alpha \geq -1$
$b$	-1	$-1 \geq b \geq -2$
$n$	-2	$-0.6 \geq n \geq -2$
$d$	1	1
$s$	-2.5	$-1.4 \geq s \geq -3$

## 1.2. Very long baseline interferometry

### 1.2.1. Radiointerferometry

Radioastronomy can be done with single dish telescopes or with radiointerferometry, the synchronization of several single dish telescopes.

The angular resolution for a telescope, is given by [Bass \(1995\)](#) and can be obtained with the Rayleigh criterion, which describes that two sources can just be resolved, if the principal diffraction maximum of one source agree with the minimum of the other. Equation 1.2.1 give this angular resolution  $\theta$ :

$$\theta = 1.22 \frac{\lambda}{D} \quad (1.2.1)$$

Here  $\lambda$  is the wavelength of the observed radiation and  $D$  the diameter of the telescope dish. The numerical factor 1.22 is the consequence of the calculation of the first minimum around two just resolved objects. In this calculation a Bessel function is taken into account to solve this problem. 1.22 is approximately the first zero of the first kind Bessel function of order one, which is additionally divided by  $\pi$ .

To enhance the angular resolution of a radio telescope, the observation can be done at shorter wavelength, but this is sometimes not possible, because one wants to observe an object at this special wavelength, because of special features of the object in this wavelength regime. The other possibility is to enlarge the diameter of the antenna dish. The largest steerable telescopes are the Green Bank Telescope in the USA and the Effelsberg Telescope in Germany. Both have an antenna diameter of about 100 meters. With  $D = 100$  m and the wavelength of  $\lambda = 0.70$  cm, which was used for my observation data, one can calculate the angular resolution of a single dish telescope to  $\theta \approx 17.61$  arcsec. The other way is to synchronize several single dish telescopes to a radiointerferometer. The angular resolution of an interferometer is limited by the biggest distance (baseline) between two telescopes.

The objects of my study were observed with the VLBA (Very Long Baseline Interferometer), which has a longest baseline of about 8600km. This leads to an angular resolution of about  $\theta \approx 0.20$  mas, which is 5 orders of magnitudes higher than the value of the biggest single dish telescope.

To describe radiointerferometry in detail I follow the explanation of [Burke & Graham-Smith \(2010\)](#). At first step it is regarded to know, how a single dish telescope works. The measured power of one telescope can be calculated to:

$$P = \int_0^\infty d\nu A_{eff}(\nu) S(\nu) \quad (1.2.2)$$

Here is  $A_{eff}$  the effective area of the antenna dish. The affective area is always smaller than the real area, because the antenna can technically not receive the whole power of the radiation, which depends on the observed frequency.  $S(\nu)$  is the flux density, which

can be calculated by integrating the whole brightness of the observed sky.

A two element interferometer after [Burke & Graham-Smith \(2010\)](#) also called Michelson interferometer is shown in figure 1.5. The two telescopes are connected by  $\vec{b}$  the baseline vector. The observed object is in the direction  $\vec{s}$ , where  $\vec{s}$  is a unit vector. In the observation of the object the two telescopes track the object, when it is moving. One of the antennas is build as reference antenna and the signal, which is detected by the second antenna, has a geometrical time delay with respect to the reference antenna, which is given by  $\tau_g = \vec{b}\vec{s}/c$ . Both signals are led in a voltage multiplier. To equalize the two signals also a variable instrumental time delay  $\tau_i$  must be inserted. In this first case  $\tau_i = 0$ . Because of the multiplication of the signals the cross-power-product is defined as time average of the product of the two signals of the antennas with the time delay  $\tau_g$ :

$$R_{xy}(\tau_g) = \langle x(t)y(t - \tau_g) \rangle = A_{eff}(\vec{s})S \cos(2\pi\nu\tau_g) = A_{eff}(\vec{s})S \cos(2\pi\vec{b}_\lambda \cdot \vec{s}) \quad (1.2.3)$$

Here  $\vec{b}_\lambda = \vec{b}/\lambda$  is the baseline vector measured in terms of wavelength. With the convolution theorem one can calculate the Fourier transformation of  $R_{xy}(\tau)$  this is also called the cross-spectrum power density:

$$S_{xy}(\nu) = A(\vec{s})S \exp(i2\pi\vec{b}_\lambda \cdot \vec{s}) \quad (1.2.4)$$

If the observed source has a finite size one can define the complex visibility function, which takes the flux of the angle size of the source into account. The visibility function can be written as:

$$V = \int A(\vec{\sigma})B_\nu(\vec{\sigma}) \exp(i2\pi\vec{b}_\lambda \cdot \vec{\sigma})d\Omega \quad (1.2.5)$$

Here  $B_\nu$  is the brightness and  $\vec{\sigma}$  is the distance vector with respect to the phase tracking vector  $\vec{s}_0$ . A new coordinate system can be implemented like one can see in figure 1.6. The origin coordinates of the baseline vector were replaced by the right handed (u,v,w) coordinates.  $\vec{w}$  has the same direction as  $\vec{s}$  and x and y are projected in the u-v-plane.  $\vec{\sigma}$  is parallel to the u-v-plane. Now equation 1.2.5 becomes the following shape:

$$V = \int_{4\pi} A(l, m)B_\nu(l, m) \exp(i2\pi(ul + vm)) \frac{dl \cdot dm}{\sqrt{1 - l^2 - m^2}} \quad (1.2.6)$$

Where  $l, m, n$  are the direction cosines of the unit vector  $\vec{s}$ . One can now realize that the visibility function V is the Fourier transformation of the Brightness  $B_\nu$ . The problem of observations with radio interferometry is that the whole u-v-plane can not be covered with the telescopes. To handle this problem the observation is done over a longer time period with the consequence, that because of the earth rotation the u-v-plane can be covered much more.

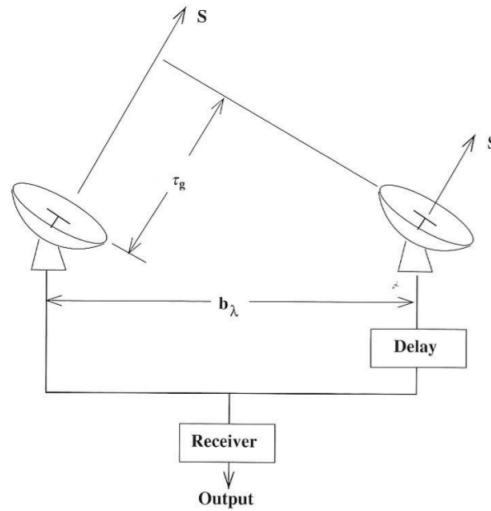


**Figure 1.5.:** Figure 5.2 of [Burke & Graham-Smith \(2010\)](#). Here the geometry of a two element Michelson interferometer is presented.  $b_\lambda$  is the baseline between the two telescopes normalized with respect to the observed wavelength.  $S$  is the vector pointing in the source direction,  $\tau_g$  is the geometrical path delay. The delay box represents an additional delay  $\tau_i$ , which can insert technical in the signal circuit.

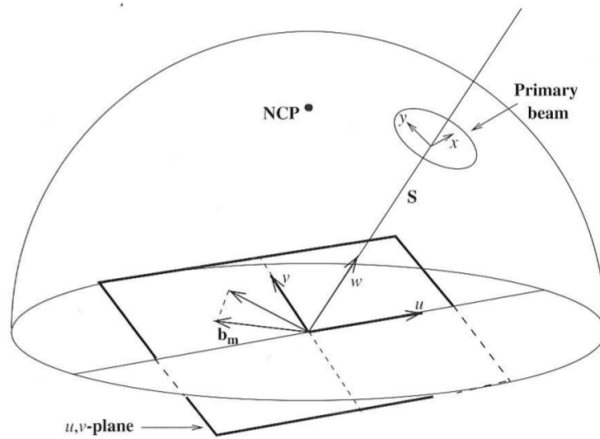


**Figure 1.6.:** Figure 5.5 of [Burke & Graham-Smith \(2010\)](#). Here the relationship of an interferometer, a source on the sky and the  $u, v$ -plain is demonstrated.  $x, y$  are the coordinate components of the offset vector  $\sigma$  to the source center, with  $x$  parallel to  $u$ . NCP is the north celestial pole.  $w$  is parallel to  $S$

### 1.2.2. Monitoring programs

**Boston University Blazar Group** The monitoring program of the Boston University Blazar Group<sup>1</sup> observes 22 flat spectrum radio quasars, 11 BL Lac objects and 3 radio galaxies. The sources are observed on average once a month, starting in 2007. The observations are performed with the Very Long Baseline Array (VLBA) at 43 GHz. The VLBA is a union of 10 radio telescopes, with each a diameter of  $d = 25$  m and identical in construction. The longest baseline between two telescopes is about 8600 km between the two telescopes on Hawaii and St. Croix on the Virgin Islands. The resolution of the observation at a frequency of 43 GHz is of about 0.2 mas. The duration of each observation is of about 40 minutes (Blasi et al. (2013)). The blazars are all  $\gamma$ -ray and X-ray selected. As explained by Williamson et al. (2014) the blazar group has also a monitoring program with the SWIFT-telescope and some other ground based infrared and optical telescopes.

**MOJAVE program** Following Lister et al. (2009) the *MOJAVE* project (*m*onitoring *of jets in active galactic nuclei with VLBA experiments*)<sup>2</sup> is a monitoring program, which observes radio jets especially the variations of brightness and polarization. All sources are located in the northern hemisphere and are associated with active galactic nuclei. The observations are also done with the VLBA, but at 15 GHz. The monitoring started in 1994 and the sample as of september 2013 comprises 127 sources, with the following selection criteria: Flux > 1.5 Jy at any time between 1994 and 2010 and declination >  $-30$ . The Interval of several observations per source ranges between once a year and once a month depending on their observed change rates.

---

<sup>1</sup><http://www.bu.edu/blazars/VLBAproject.html>

<sup>2</sup><http://www.physics.purdue.edu/MOJAVE/allsources.html>



## 2. Modeling physical parameters along parsec scale radio jets

### 2.1. Model fitting of VLBI data

To analyze the sources of my sample with respect to their brightness temperature gradient and diameter gradient, I took the calibrated data of each epoch of my sources from the homepage of the Boston University Blazar group<sup>1</sup> and analyzed this data with the program DIFMAP<sup>2</sup>, which is especially designed for synthesis imaging and model fitting of radio interferometer data. In the description I follow [Taylor \(1997\)](#) and my own experiences using DIFMAP. To explain how the fit of the brightness temperature and diameter gradient is performed, I will describe the single steps. The several flux features respectively components of each observed epoch are first fitted using spherical Gaussian model components and later on using elliptical Gaussians. To explain the fitting routine, the description is done based on the model fit of one epoch of 2200+420 as an example, which can be traced in the pictures of figure 2.2. In the first step I open the residual map as shown in figure 2.2. The bright pixels in this map represent the highest flux and the dark ones the lowest flux. Now one sets a circular Gaussian component, with the free parameters flux, major axis and position in the map. After that the program iteratively finds the best values in the parameter space for this component. After the iteration the first established model is subtracted from the u,v, plane and when opening the residual map the weaker flux features are now visible and can be fitted with another component. This iterative process is repeated until no significant flux appears in the residual map. With the complete model a clean map can be generated, which is shown in figure 2.3. After the model fitting with the circular Gaussian components, one can add two other degrees of freedom, which is the the minor axis and angular orientation of this axis. In the next the model fit is done with elliptical Gaussian Components. This elliptical model is done, because it is assumed, that the emitting jet is boosted in one direction and hence an elliptical model might in some cases represents the data better. In most cases the elliptical model fit requires less components as in the same model fit with circular components. This means that features, which are described by two circular components,

---

<sup>1</sup><http://www.bu.edu/blazars/VLBAproject.html>

<sup>2</sup>Caltech difference mapping program - version 2.4l (17 Apr 2010) Copyright (c) 1993-2008 California Institute of Technology. All Rights Reserved. Homepage: <ftp://ftp.astro.caltech.edu/pub/difmap/difmap.html>

can now be described by one elliptical component. If an elliptical component diverges with respect to the ratio of major and minor axis, meaning that it becomes zero, the component has to be set back to a circular one.

## 2.2. Previous studies of brightness temperature gradients in AGN jets

An important example of previous studies the study of Kadler et al. (2004) about NGC 1052 shall be mentioned here. He expands the jet model of Blandford & Königl (1979) and Königl (1981) with respect to the power law behavior of the brightness temperature gradient. Burd (2014) fitted 19 quazars and 2 blazars of the MOJAVE 15 GHz sample and analyzed the brightness temperature gradient. In my work I will fit 11 BL Lac objects of the Boston University 43 GHz sample and will fit the brightness temperature gradient and the diameter gradient along the jet axis with a power law and discuss these under the presumption of the jet models of Blandford & Königl (1979), Königl (1981) and its extension for the brightness temperature by Kadler et al. (2004). I will also discuss deviations from the model such as the appearance of excesses in the brightness temperature gradient that is observed in individual sources. In addition I will compare the data of selected sources with observations performed at 15 GHz from the MOJAVE monitoring program. The results will be compared with the expected canonical values derived by Blandford & Königl (1979) and Königl (1981).

## 2.3. Sample selection and data reduction

I picked out eleven BL Lac object out of the Boston University sample. The radio images of these sources can be seen in image 2.1.

The first step of my work with the data was to fit 20 epochs of all selected sources, both with circular and elliptical Gaussian components. After this step I reject all sources, which possess no extended jet, meaning, I inspect for each source, whether it is possible to fit on average a minimum of four components in each epoch. This step is necessary, because in the analysis of the fitted data one component has to be set as the radio core and in several epochs it is the case that more components are inside the core region and hence can not be regarded for the power law fit. according to these selection criterion 1055 + 018 and 1219 + 285 are no longer considered for the following analysis.

For remaining BL Lac objects all available epochs were fitted with circular and elliptic Gaussian components, as described before. The number of epochs of each source ranges between 30 and 85 epochs. All sources are shown in table 2.1 with their common names, B1950 name and their redshifts.

As a next step for each epoch of a source a core alignment is performed. Therefore the component with the smallest distance to the origin is used After this all components are

treated as a core region, which have a small core distance and at the same time show a brightness temperature  $T_b \gg 10^{12} K$ . The brightness temperature of these components can not be explained with synchrotron radiation, but is the consequence of the inverse Compton catastrophe as described in chapter 1.1. These components are not considered for the fit of the gradients.

The fit of the gradients was performed using a linear regression on logarithmic scales, meaning  $\log(T_b)$  was fitted as function of  $\log(d_{core})$ . That is done estimating the relative error of the observed flux to be 10% and the relative error for the minor and major axis to be 20%. The error of the brightness temperature is computed according the propagation of uncertainty by Gauss. The errors of the measured power law indices instead are the errors only taking into account the statistical uncertainties of the linear regression. The errors do not consider the systematic uncertainties of the brightness temperature and diameter.

The given  $\chi_{red}^2$  is a pseudo  $\chi_{red}^2$  and only indicates the deviation of the data from the model.

For the following discussion the brightness temperature gradient was fitted using the elliptical and the circular model and the diameter along the jet axis was fitted using the circular model.

**Table 2.1.:** All sources of the sample with their B1950 name, common name, redshift and reference to the redshift

B1950 Name	Common Name:	redshift	reference for redshift
0219 + 428	3C 66A	0.44	<a href="#">Furniss et al. (2013)</a>
0716 + 714	S5 0716+71	0.31	<a href="#">Nilsson et al. (2008)</a>
0735 + 178	OI 158	0.424-0.45	<a href="#">Nilsson et al. (2012)</a>
0829 + 046	OJ 049	0.174	<a href="#">Abazajian et al. (2005)</a>
0851 + 202	OJ 287	0.306	<a href="#">Stickel et al. (1989)</a>
0954 + 658	S4 0954+65	0.367	<a href="#">Rector &amp; Stocke (2001)</a>
1055 + 018	4C +01.28	0.888	<a href="#">Shaw et al. (2012)</a>
1101 + 384	Mrk 421	0.0308	<a href="#">Ulrich et al. (1975)</a>
1219 + 285	W Comae	0.103	<a href="#">Shaw et al. (2013)</a>
1749 + 096	4C +09.57	0.322	<a href="#">Stickel et al. (1988)</a>
2200 + 420	BL Lac	0.0686	<a href="#">Vermeulen et al. (1995)</a>

## 2. Modeling physical parameters along parsec scale radio jets

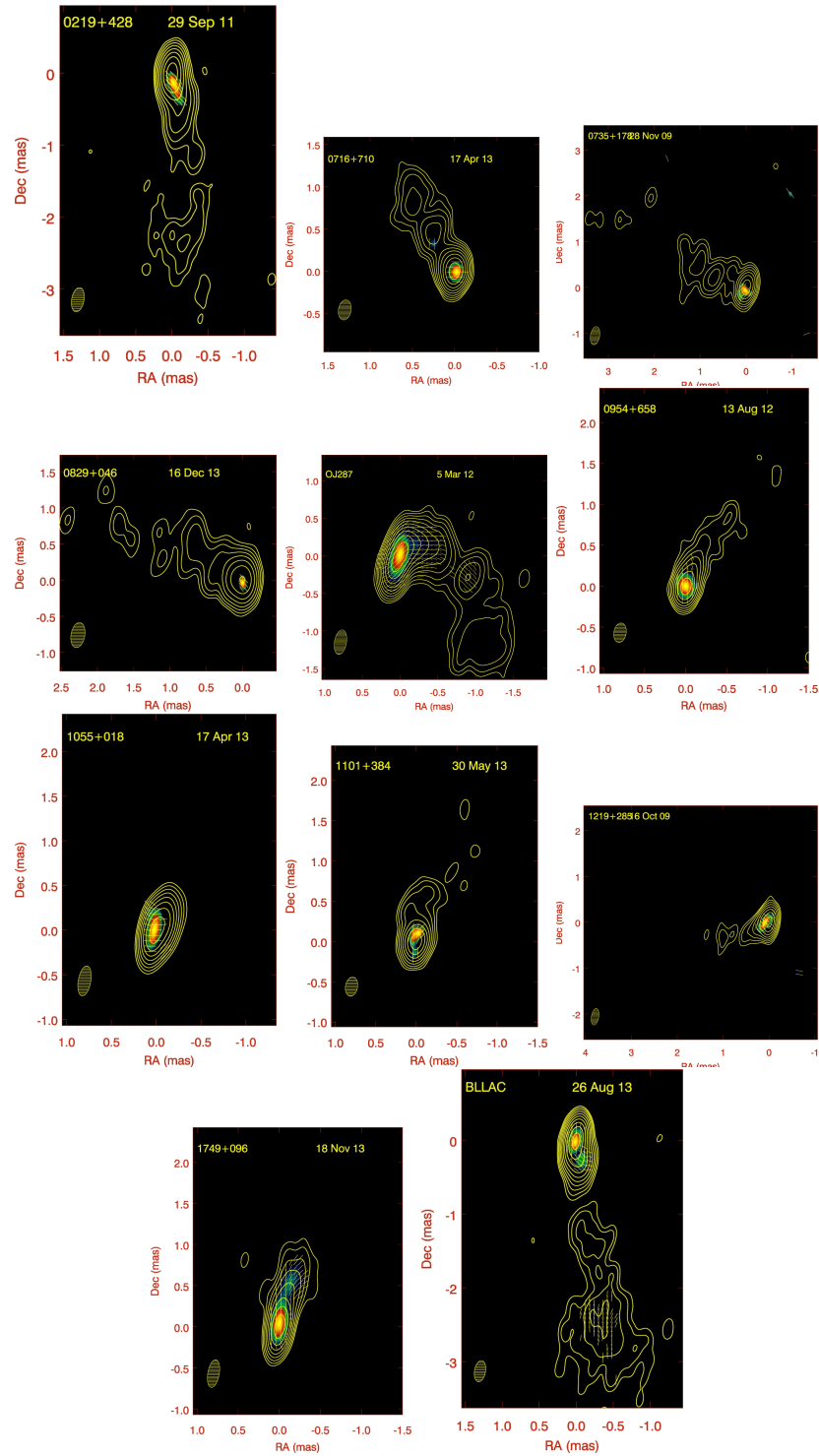


**Figure 2.1.:** Here a random picked image of each considered source of my sample is pictured with its name and the date of observation. Dec is the declination and RA is the right ascension. The images were taken from the homepage of Boston University Blazar group (<http://www.bu.edu/blazars/VLBaproject.html>)

### 2.3. Sample selection and data reduction

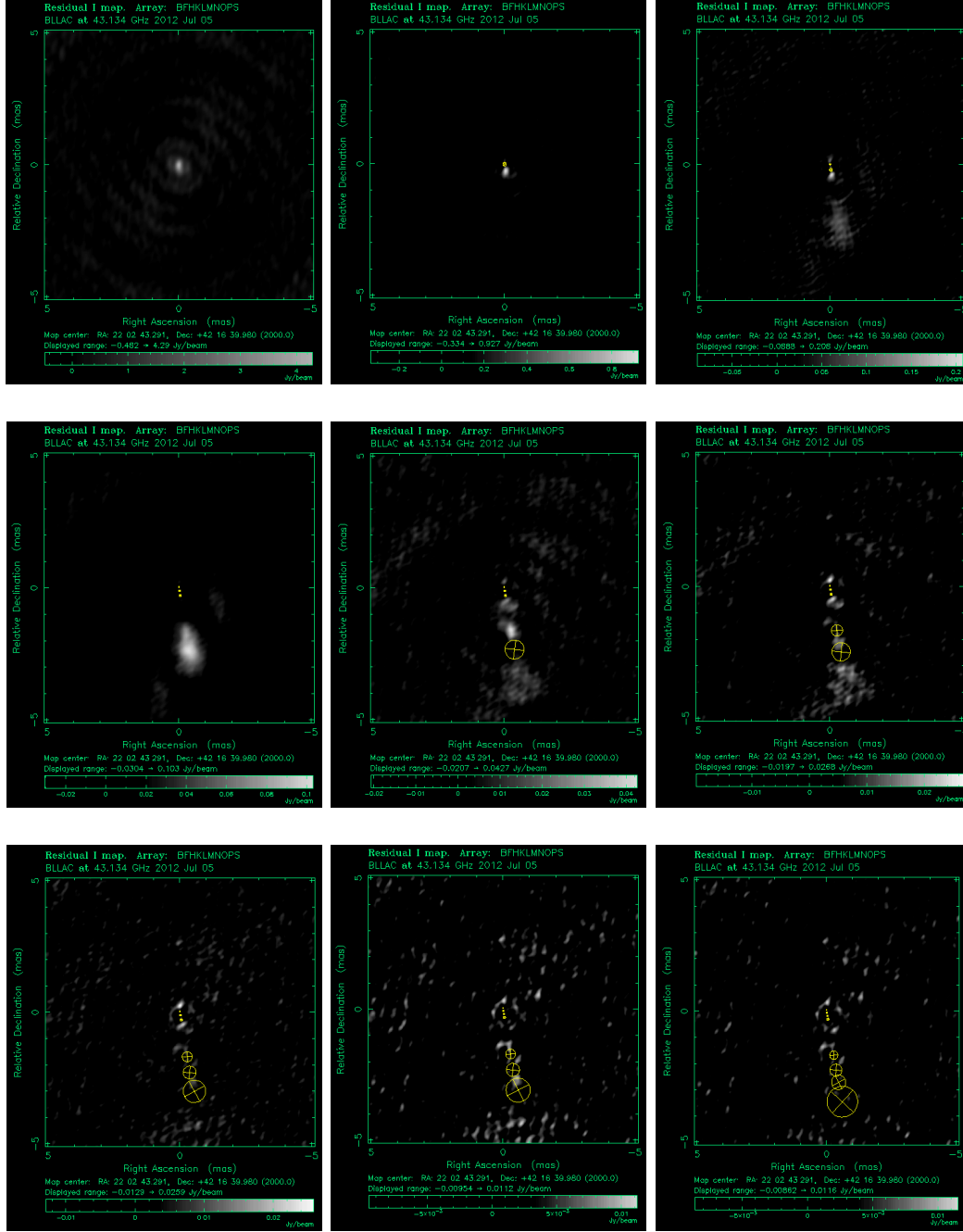
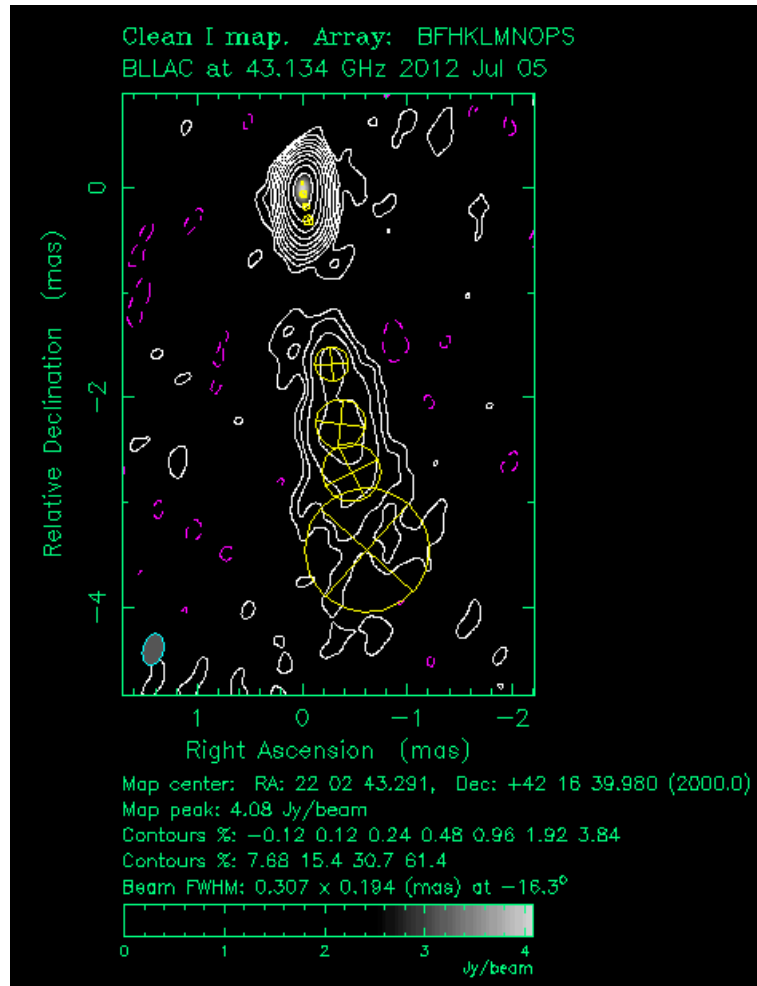


Figure 2.2.: residual maps for the several fitting steps including the fitted circular components. The time line is from left to right



**Figure 2.3.:** Clean map of 2200+420 for the epoch 2012-07-05, with the fitted model components

# 3. Results

Before discussing individual features observed in single sources, the overall and general results which are determined from this study are presented.

## 3.1. Sample results

The measured results for the 9 BL Lac objects considered in this study are summarized in table 3.1. The power law index  $l$  of the diameter gradient as well as the power law indices  $s_{ell}$  and  $s_{circ}$  for the gradient of the brightness temperature are listed. The given error respects the statistical error of the linear regression that has been used to perform the fits. Details are described in section 2.3. While the gradient of the diameter is fitted using the circular model the gradient of the brightness temperature is determined using both models, the circular and the elliptical one ( $s_{circ}$  and  $s_{ell}$ ). All plots of the diameter gradient are shown in figure 3.3. The plots of the brightness temperature gradient fitted with the circular component model are shown in figure 3.2, while the one using the elliptical model is pictured in figure 3.1. All three indices are plotted in histograms to check their distribution of abundance (see figures 3.4, 3.5, 3.6).

According to the theory of Blandford & Königl (1979) the power law index  $l$  has to be  $l = 1$  and the power law index  $s$  has to be  $s = -2.5$  or vary between  $-1.4 > s > -3$  in the case of Königl (1981).

As a main result of my work I found the index of the diameter gradient to be  $l \approx 0.91$  on average for all studied sources. The median is  $l \approx 0.78$  representing that 2200+420 shows a far larger index  $l$  than all other sources on scales  $d_{core} \gtrsim 2$  mas, which will be discussed later on as a feature found in one individual source. Within the standard deviation of  $\sigma_l \approx 0.54$  it is found that  $\langle l \rangle < 1$ . Hence the case of a conical jet predicted by Blandford & Königl (1979) and Königl (1981) does not hold for the sources studied in this work, but a stronger collimation is observed on these scales. Only 0954+658 shows within its error a pure conical jet with a power law index of  $l = 1.018 \pm 0.020$ . Fitting the brightness temperature gradient so far allows to argue that the measured indices  $s$  are consistent with  $-1.4 > s > -3$  as predicted by Königl (1981) for all sources except 2200+420. This holds for both models, the circular and the elliptical. As for  $l$  the mean, the standard deviation and the median are listed in table 3.2.

Taking a closer look at the plots of the individual objects, some sources show a high scattering of data points and show also a very high pseudo  $\chi^2$  indicating large deviations from the fit. The high scattering of the data can be the consequence of an only partially

resolved jet. In this case small components are fitted although they should be larger. Assuming that an elliptical model describes the data as good as a circular  $s_{ell}$  and  $s_{circ}$  should be the same, meaning being consistent with each other within their uncertainties. A detailed determination of the errors of the power law indices is beyond the scope of this thesis. But the found deviations between  $\langle s_{ell} \rangle$  and  $\langle s_{circ} \rangle$ ,  $\Delta s = |\langle s_{ell} \rangle - \langle s_{circ} \rangle| \approx 0.16$  can be used as a first estimation of these uncertainties.

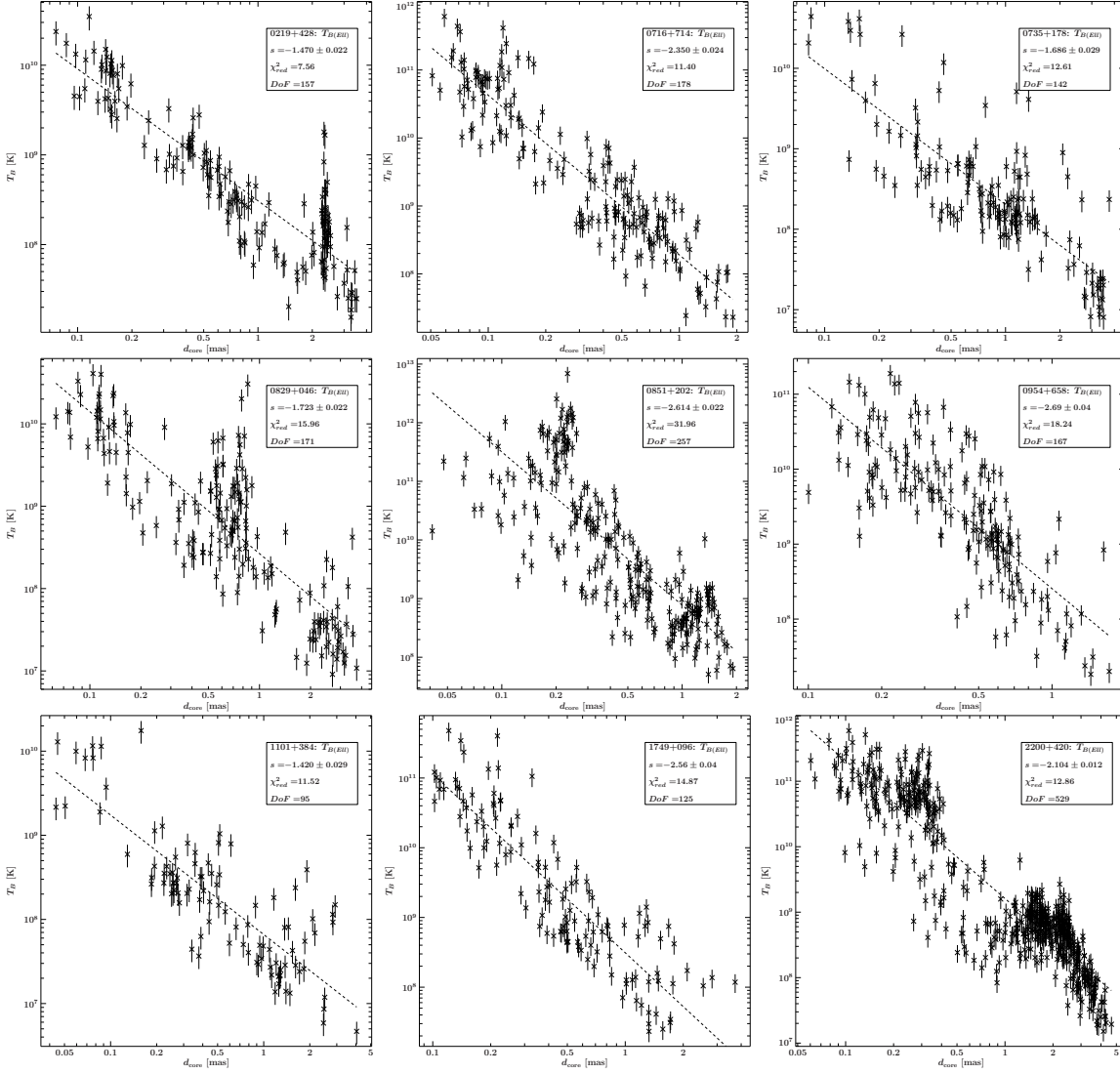


**Figure 3.1.:** The brightness temperature gradients for all considered sources of my sample are shown. The brightness temperature gradient is fitted using elliptical components. All gradients were measured at 43 GHz and were fitted assuming a pure power law with a power law index  $s_{\text{ell}}$

### 3. Results

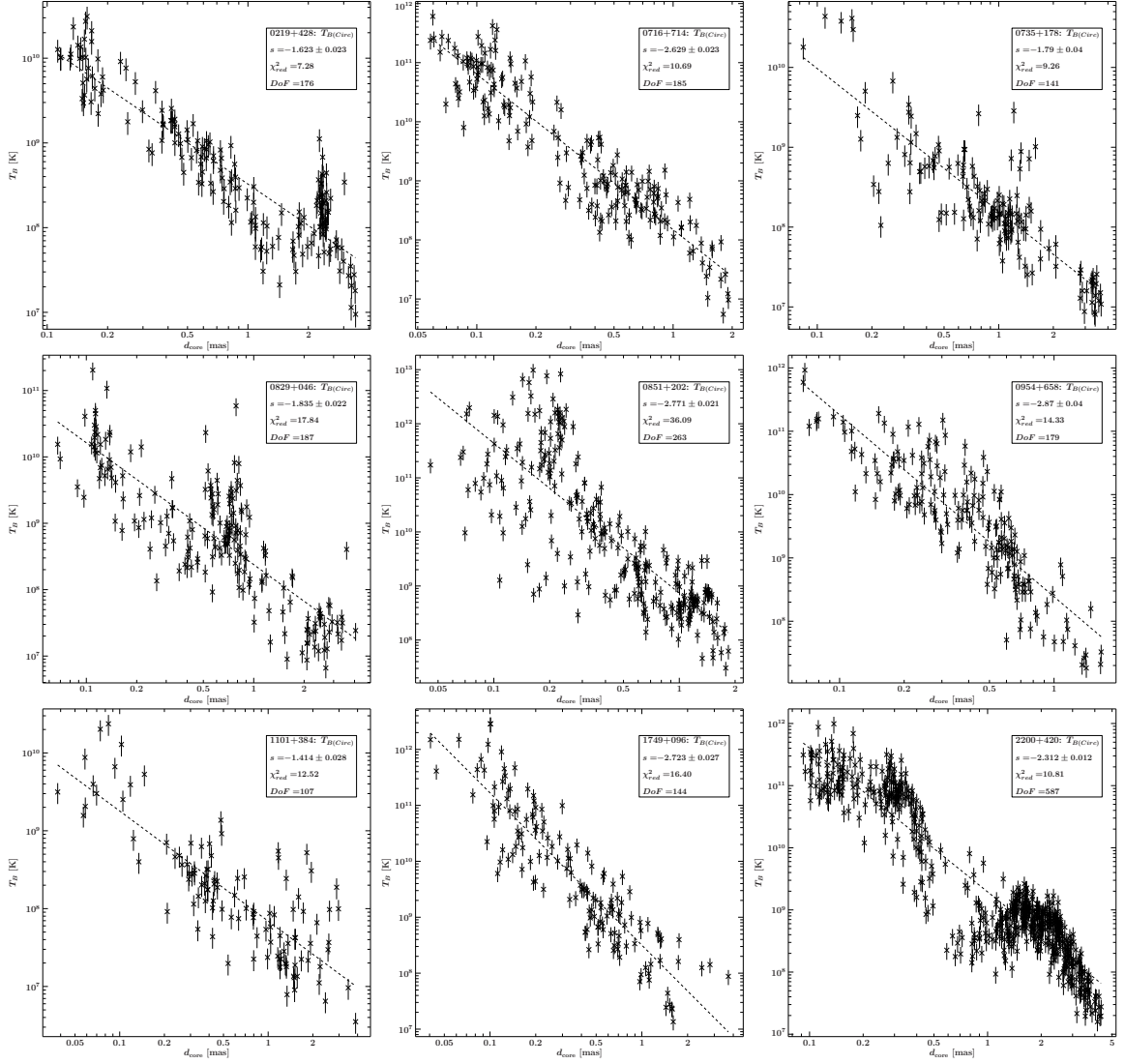


**Figure 3.2.:** The brightness temperature gradients for all considered sources of my sample are shown. The brightness temperature gradient is fitted using circular components. All gradients were measured at 43 GHz and were fitted assuming a pure power law with a power law index  $s_{\text{circ}}$

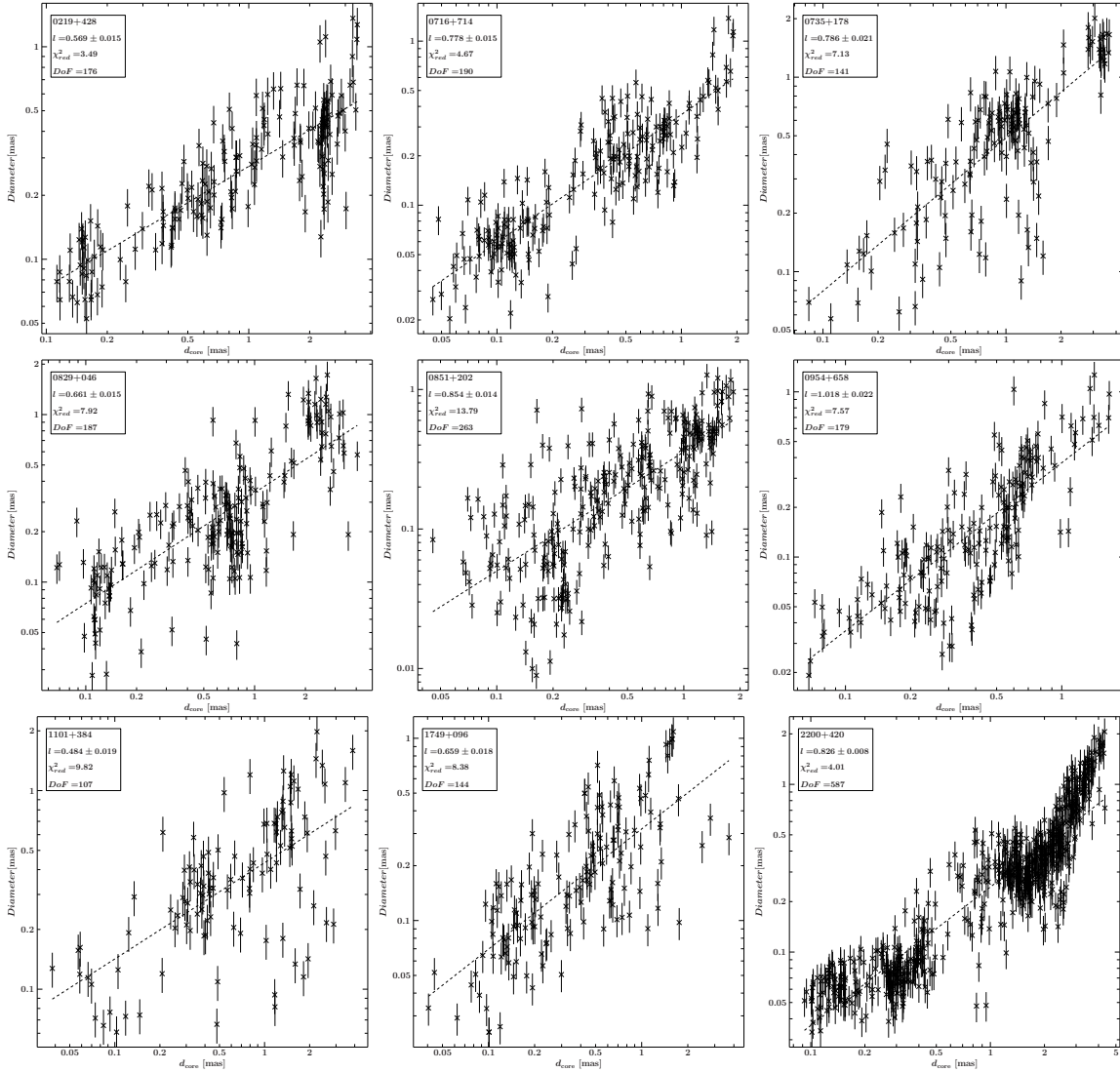


**Figure 3.3.:** The diameter gradients for all considered sources of my sample are shown. The diameter gradient is fitted using circular components. All gradients were measured at 43 GHz and were fitted assuming a pure power law with a power law index  $l$

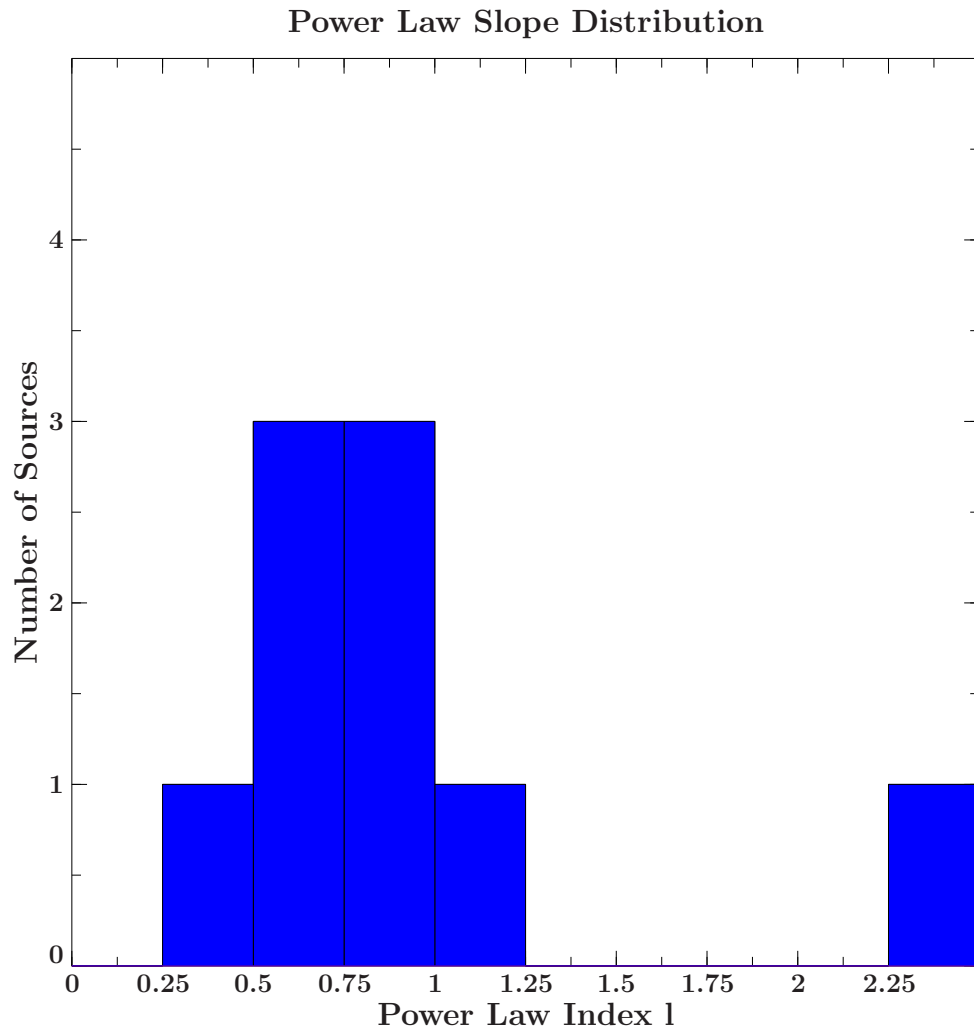


**Figure 3.4.:** The distribution of the power law index  $l$  is pictured. The binning is 0.25

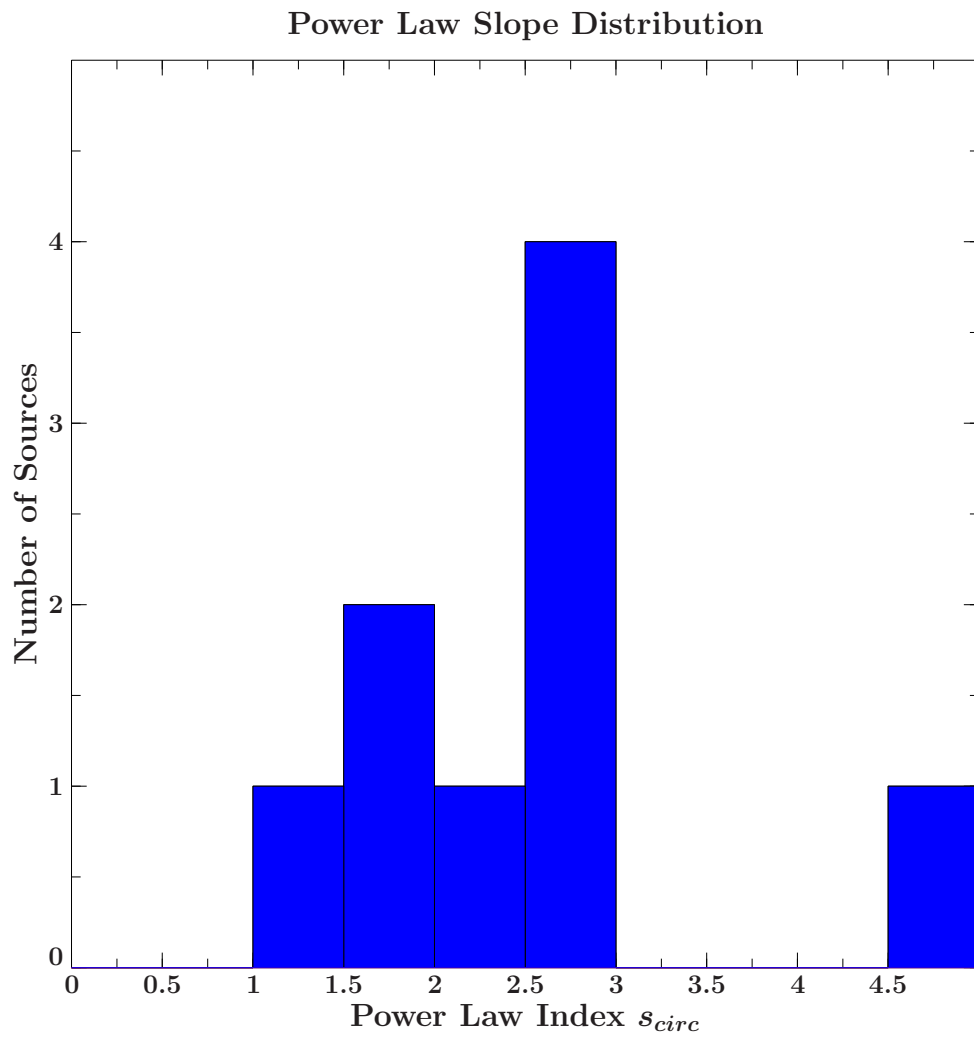


**Figure 3.5.:** The distribution of the power law index  $s_{circ}$  is pictured. The binning is 0.5

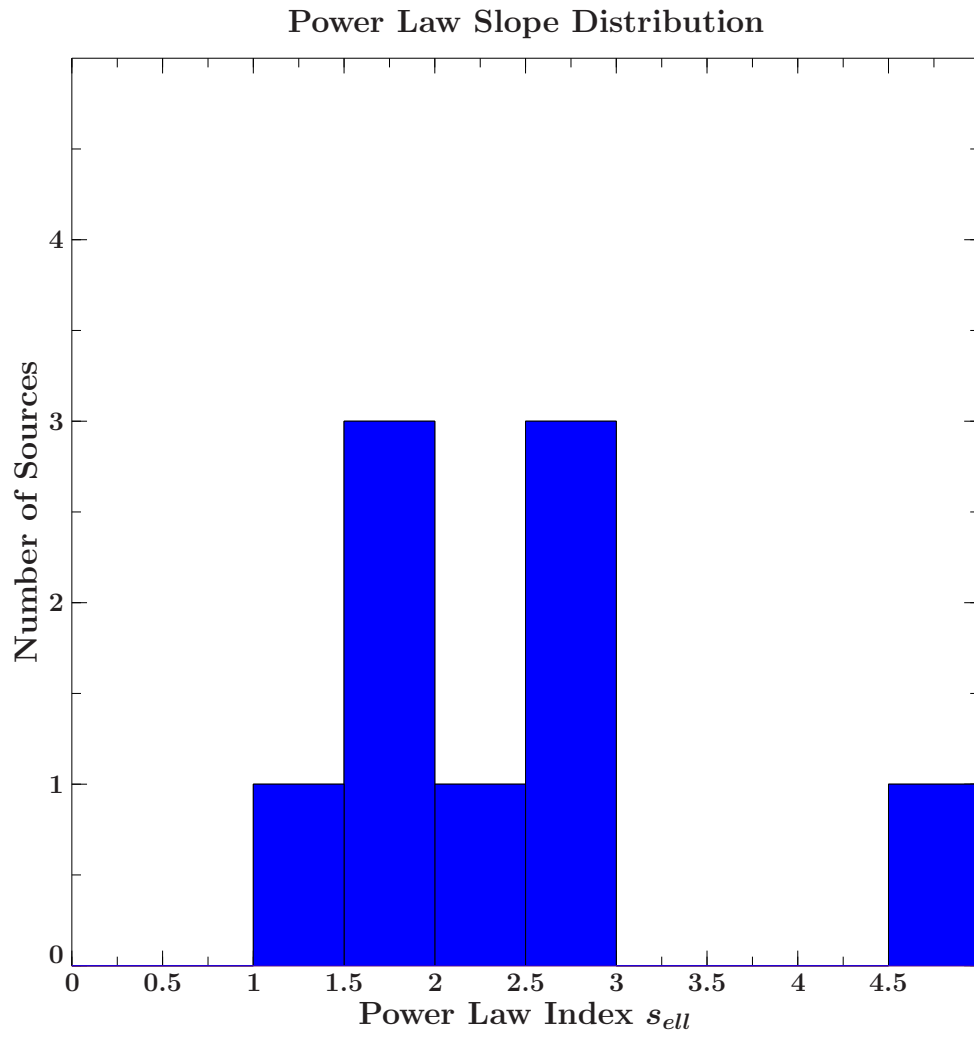


**Figure 3.6.:** The distribution of the power law index  $s_{ell}$  is pictured. The binning is 0.5

**Table 3.1.:** Power law indices  $s_{ell}$ ,  $s_{circ}$ ,  $l$  with errors for all considered sources

source	$s_{ell}$	$s_{circ}$	$l$	remarks
0219 + 428	$-1.470 \pm 0.022$	$-1.623 \pm 0.023$	$0.569 \pm 0.015$	
0219 + 428	$-1.92 \pm 0.04$	$-2.11 \pm 0.04$	$0.674 \pm 0.026$	excess ignored
0716 + 714	$-2.350 \pm 0.024$	$-2.629 \pm 0.023$	$0.778 \pm 0.015$	
0735 + 178	$-1.686 \pm 0.029$	$-1.79 \pm 0.04$	$0.786 \pm 0.021$	
0829 + 046	$-1.723 \pm 0.022$	$-1.835 \pm 0.022$	$0.661 \pm 0.015$	
0851 + 202	$-2.614 \pm 0.022$	$-2.771 \pm 0.021$	$0.854 \pm 0.014$	
0954 + 658	$-2.69 \pm 0.04$	$-2.87 \pm 0.040$	$1.018 \pm 0.022$	
1101 + 384	$-1.420 \pm 0.029$	$-1.414 \pm 0.028$	$0.484 \pm 0.019$	
1749 + 096	$-2.56 \pm 0.04$	$-2.723 \pm 0.027$	$0.659 \pm 0.018$	
2200 + 420	$-2.104 \pm 0.012$	$-2.312 \pm 0.012$	$0.826 \pm 0.008$	
2200 + 420	$-4.64 \pm 0.12$	$-4.88 \pm 0.11$	$2.29 \pm 0.08$	$d_{core} \gtrsim 2$ mas

**Table 3.2.:** The mean value the median and the standard deviation of each power law index is listed

	$ s_{ell} $	$ s_{circ} $	$l$
Mean	2.40	2.56	0.91
Standard deviation	0.96	1.01	0.54
Median	2.35	2.63	0.78

## 3.2. Individual source studies

**0219+428** shows an underlying power law but in addition an excesses in the brightness temperature gradient and a dip in the diameter gradient at a core distance of about 2 mas. This can be seen in figure 3.7. The excess includes 60 components, which is almost twice the number of epochs meaning that there is at least one component at this position in every model fitted epoch of the object. The dip in the diameter gradient is

due to the fact that this region in the jet can be described by more than one component, which have different major-axis but almost the same core distance.

This excess can be regarded as a stationary component, which does not move in time. Because the plot of the diameter gradient shows a dip, where the plot of the brightness temperature gradient shows an excess, this can also mean the jet is collimated at this position of the jet. As a consequence of this, the charge density rises and so also the brightness temperature rises immediately, when the theory of Blandford & Königl (1979) and Königl (1981) holds.

Now I compare my data with a brightness temperature and diameter gradient study of 0219+428 performed at 15 GHz. This study was done by Till Steinbring in the same way as explained in 2. He took the data of 0219+428 out of the MOJAVE sample. In comparison with the brightness temperature and diameter gradient of my data, 0219+428 shows the same excess respectively dip around the similar core-distance  $d_{core} \approx 2.5$  mas, which is pictured in the plots of figure 3.7. This agrees with the assumption of the collimation of the jet at this position.

In figure 3.8 a VLBI image of 0219+428 is illustrated. The image is stacked of 21 epochs of the MOJAVE sample with epochs between 2001 and 2013. One can see the stationary component in red color at a core distance of 2 mas. The MOJAVE team also performed a kinematic study of 0219+428. Figure 3.9 represents the separation of individual components as function of time with a linear fit to each considered component separation. The pink data points lie at a core distance of about  $d_{core} \approx 2$  mas and can be identified with the excess in the brightness temperature gradient. One can recognize in the plot that this component moves only very slowly and can almost be regarded as stationary. If the excess respectively the dip is not considered for the power law fit, the power law indices's of 0219+428 change, which is shown in table 3.1. Also the  $\chi_{red}^2$  of all values decrease and without the excess both the brightness temperature gradient and the diameter gradient can be fitted very well using a pure power law, which can be seen in plots of figure 3.7. With a  $\chi_{red}^2 = 4.39$  for the circular  $T_b$ -fit and  $\chi_{red}^2 = 2.24$  for the diameter gradient fit.

This feature observed in 0219+428 is not unique with respect to the gradients of 0219+428, also other object show these feature. In my sample the brightness temperature and diameter gradient of 0829+046 can possibly show the same feature as one can see in figures 3.1, 3.2, 3.3.

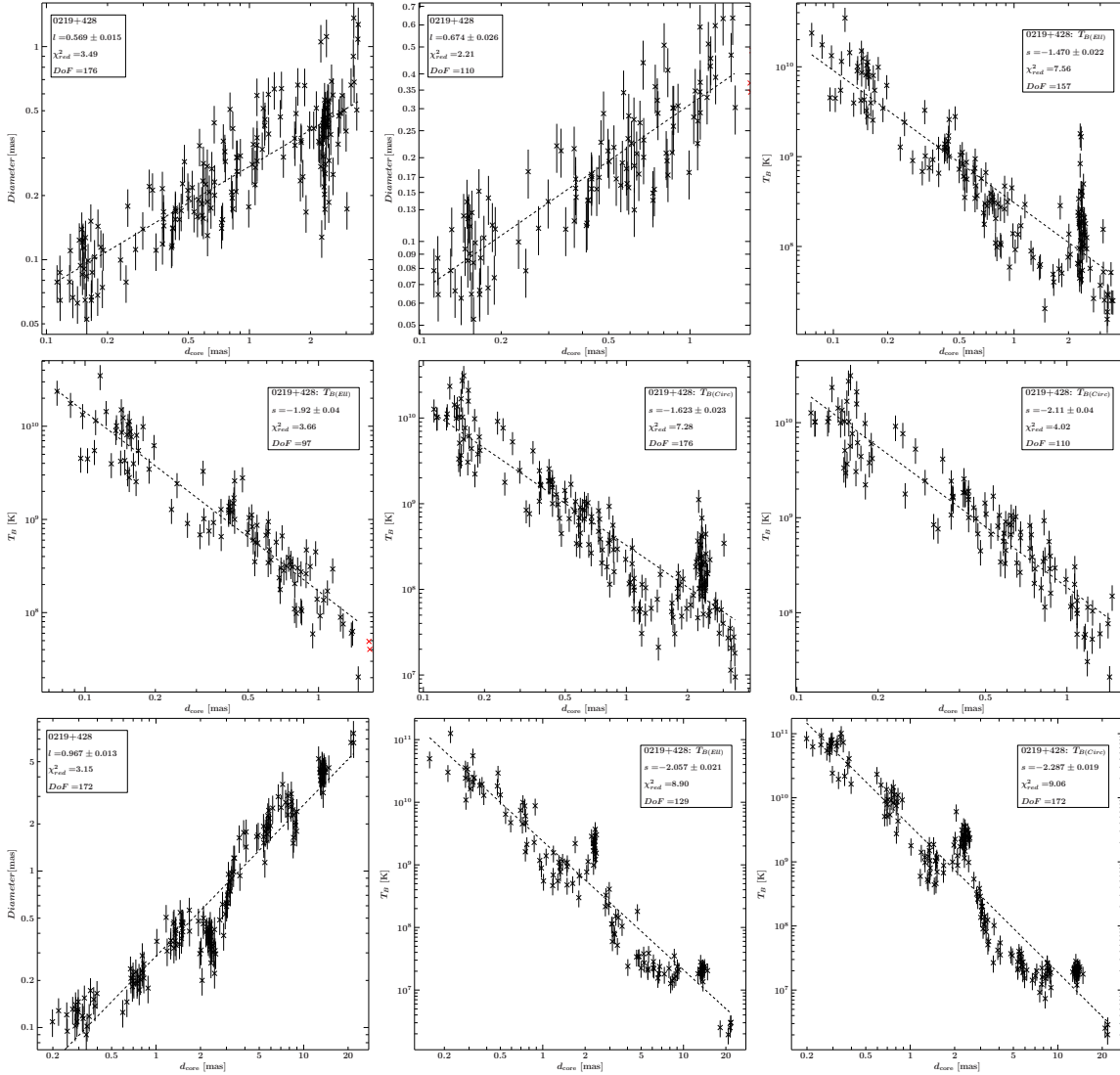


**Figure 3.7.:** From left to right: The first plot shows the fitted diameter gradient measured at 43 GHz, the second the diameter gradient measured at 43 GHz, here the excess at  $\approx 2.5$  mas is excluded. The third shows the fitted brightness temperature gradient for the elliptical model with the excess and the fourth without the excess, both measured at 43 GHz. The fifth plot shows the fitted brightness temperature gradient for the circular model with the excess and the sixth without the excess, both measured at 43 GHz. Picture 7 shows the fitted diameter gradient, picture 8 the brightness temperature gradient for the elliptical model and picture 9 the brightness temperature gradient for the circular model, all measured at 15 GHz and model fitted by Till Steinbring. The excess in the brightness temperature gradient as well as the dip in the gradient of the diameter at  $\approx 2.5$  mas can clearly be seen at both frequencies

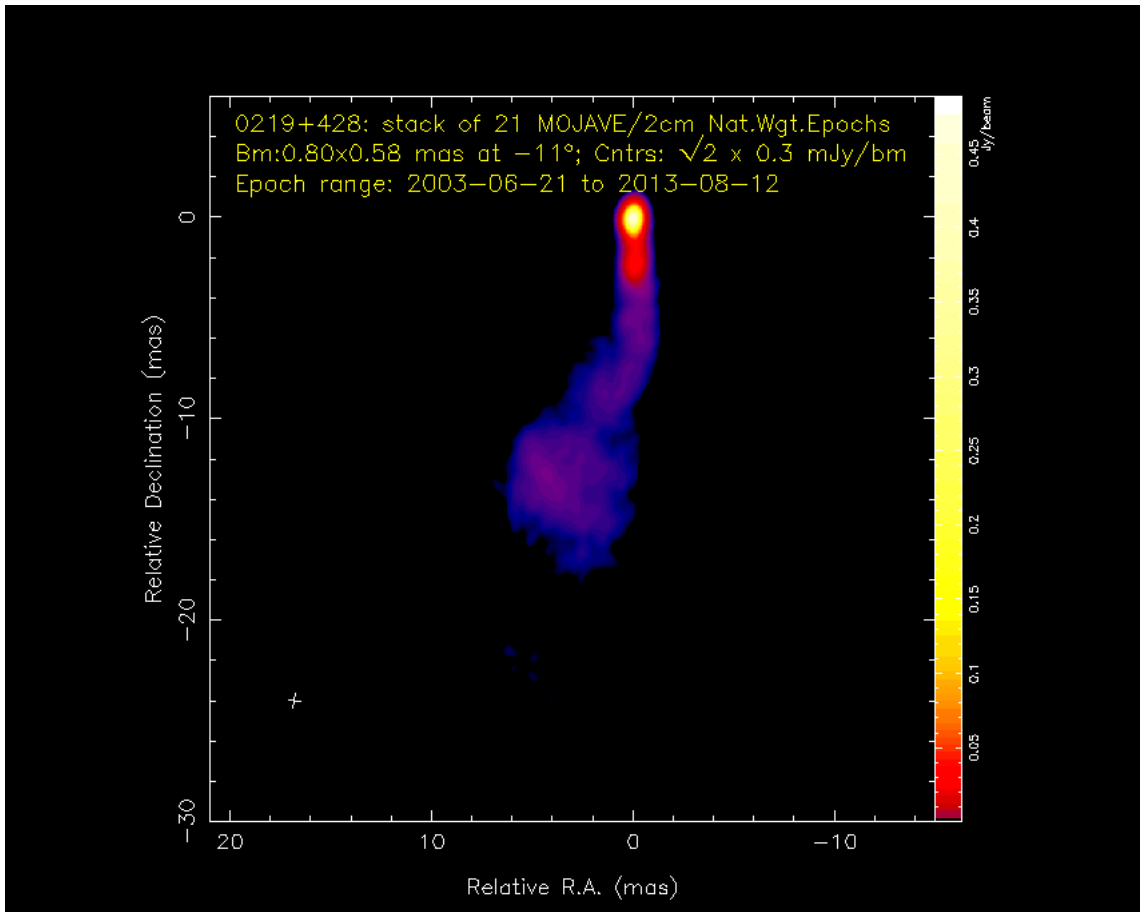


**Figure 3.8.:** Stacked image of 0219+428. The data are taken from the MOJAVE homepage (<http://www.physics.purdue.edu/MOJAVE/allsources.html>). The stacked image was generated with a stack of 21 15 GHz epochs between 2003-06-21 and 2013-8-12. The intensity is color coded.

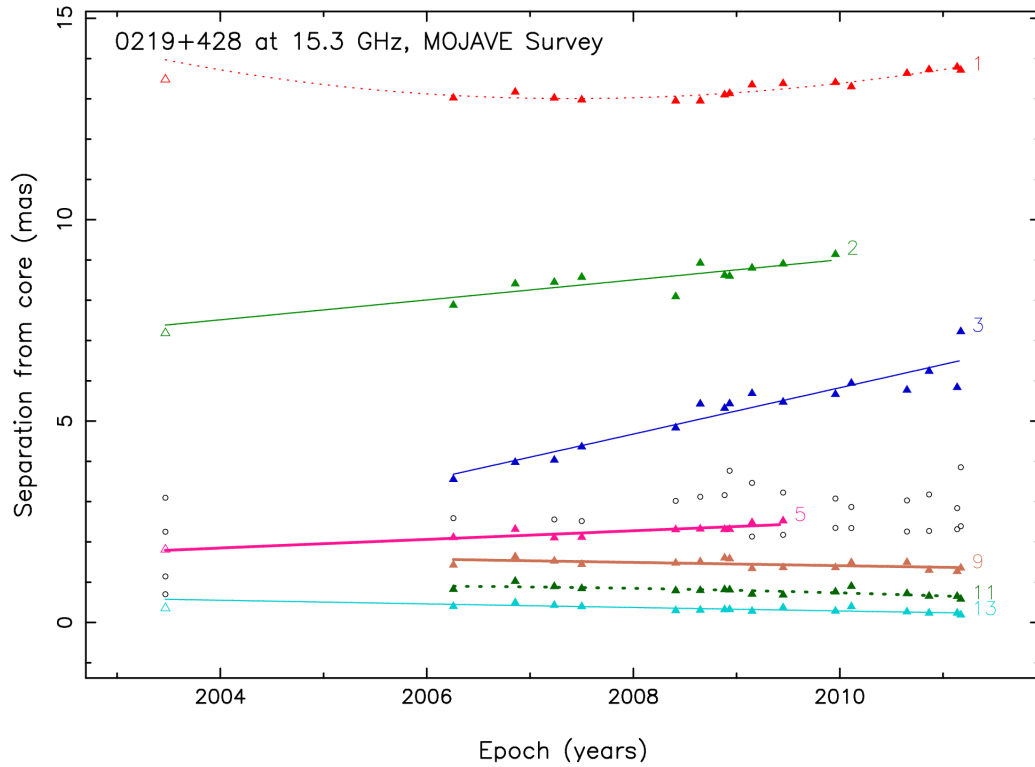


**Figure 3.9.:** The plot shows the separation from the radio core as a function of the time of individual epochs with a linear fit for each component. The pink data points and the pink line illustrate the separation of a slowly moving component at around 2 mas that could for our purpose be treated as a stationary feature. This might explain the excess in the brightness temperature gradient as well as the dip in the diameter gradient. The tracking analyzes were done with 15 GHz VLBI data of the MOJAVE sample and was taken from the MOJAVE homepage (<http://www.physics.purdue.edu/MOJAVE/allsources.html>).

**2200+420 (BL-Lac)** Both the brightness temperature gradient and the diameter gradient of BL Lac can not be described by a pure power law. In the plots of figures 3.10 one can see, that there is a cluster of data in the brightness temperature gradient between 0.1 mas and 0.4 mas, which seems to do not follow a power law. At a core distance of about 0.4 mas the brightness temperature gradient falls down and at a core distance of about 0.7 mas the brightness temperature gradient rises, but the diameter gradient has no significant deviations of a possible power law. There are no significant alternations in the slope or in curvature, of the diameter gradient as one can recognize in the brightness temperature gradient in figure A.33. At a core distance of approximately 1.5 mas it can be possible that there is a dip in the brightness temperature gradient and a excess in the diameter gradient. Falling and rising of the brightness temperature gradient can be the consequence of deboosting as described in chapter 1.1, meaning the particles are boosted in the direction of observing up to  $d_{core} \approx 0.4$  mas and were deboosted between 0.4 mas and 1 mas. According to a private discussion with M. Kadler and P. R. Burd this can be the effect of jet bending, meaning the jet axis is not linear, but rather curvy. As shown in figure 3.10 one can see that the brightness temperature and the diameter gradient follow a power law for a core distance  $d_{core} \gtrsim 2$  mas. The indices are also shown in table 3.3. One can compare this results of the power law fit with 15 GHz data of BL Lac from the MOJAVE sample, which was fitted by Till Steinbring. The power law indices are also shown in table 3.3. If one compares the values of the fits one can recognize, that the values match each other, when take the scattering of data in to account. In figure 3.11 a stacked radio image of BL Lac out of the MOJAVE sample is presented. The image shows at a core distance of 2 mas a strong opening of the jet.

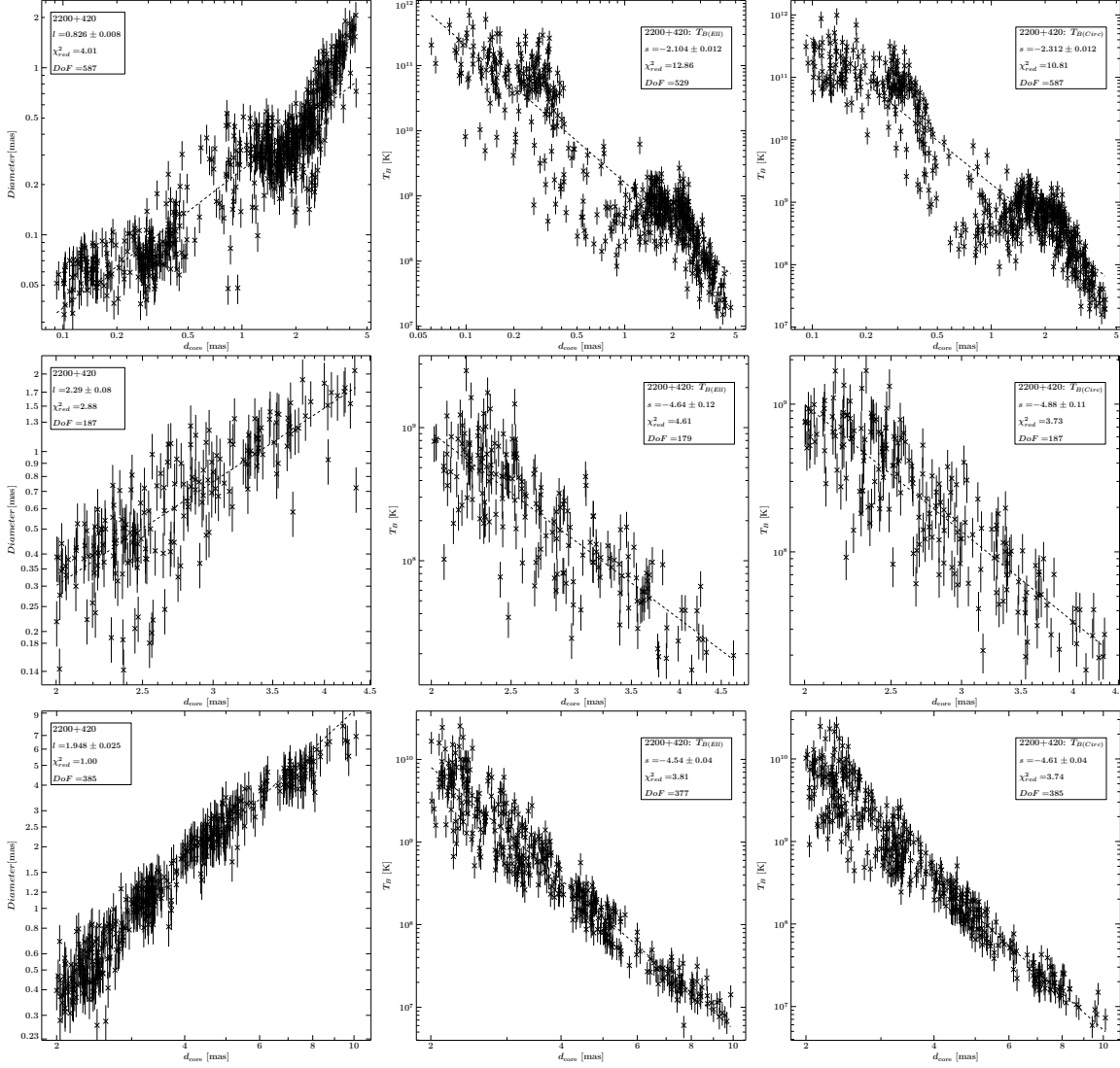


**Figure 3.10.:** From left to right. The first three plots include the power law fits of the diameter gradient and the two brightness temperature gradients measured at 43 GHz. The second three plots include the power law fits of the diameter gradient and the two brightness temperature gradients all started at  $d_{core} = 2$  mas and measured at 43 GHz. The last three plots include the power law fits of the diameter gradient and the two brightness temperature gradients all started at  $d_{core} = 2$  mas and measured at 15 GHz, model fitted by Till Steinbring.

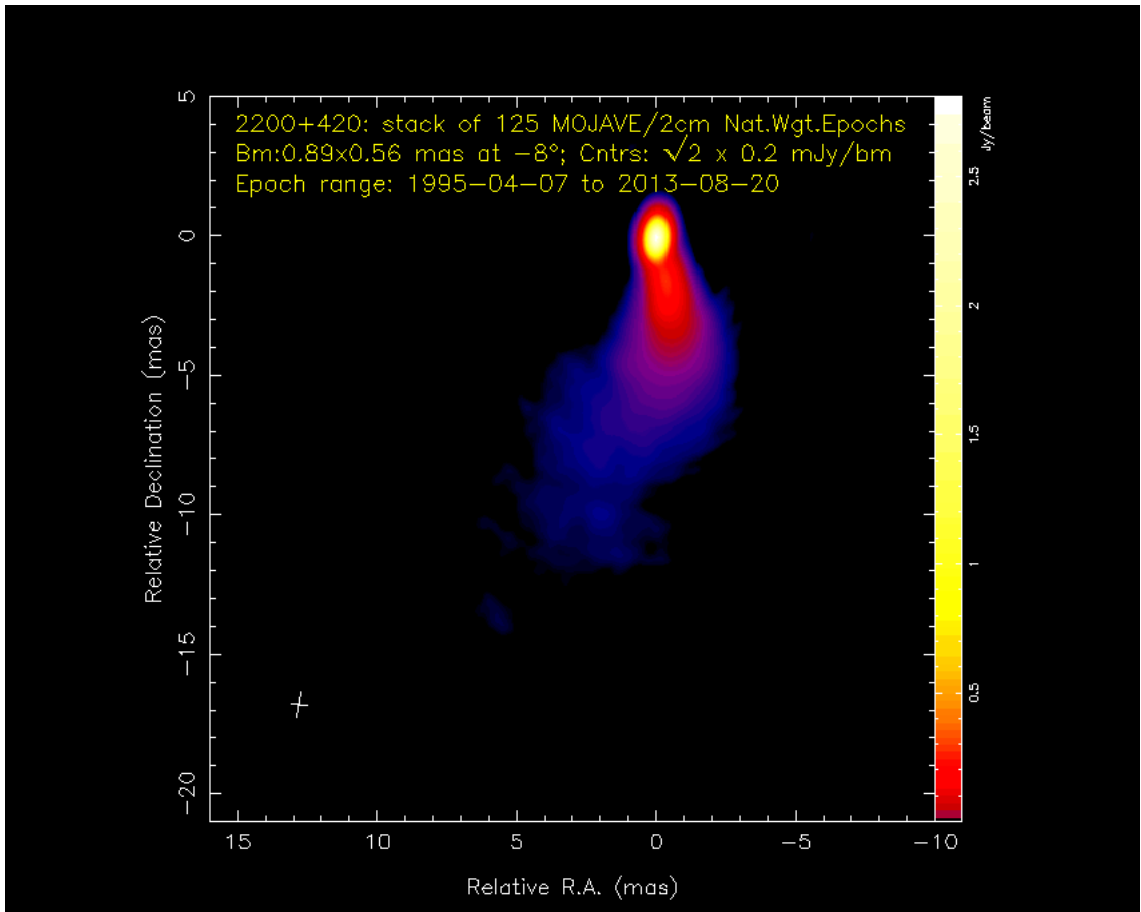


**Figure 3.11.:** Stacked image of 2200+420. The data are taken from the MOJAVE homepage (<http://www.physics.purdue.edu/MOJAVE/allsources.html>). The stacked image was generated with a stack of 125 epochs between 1995-04-07 and 2013-8-20. The intensity is color coded.

**Table 3.3.:** Power law indices  $s_{ell}$ ,  $s_{circ}$ ,  $l$  with  $\chi^2_{red}$  and degrees of freedom (DoF) for BL Lac (2200+420), measured at 43 GHz and at 15 GHz using MOJAVE data model fitted by Till Steinbring

frequency	power law index	value	$\chi^2_{red}$	DoF
43 GHz	1	2.29	2.88	187
43 GHz	$s_{ell}$	-4.64	4.61	179
43 GHz	$s_{circ}$	-4.88	13.73	187
15 GHz	1	1.948	1.00	385
15 GHz	$s_{ell}$	-4.54	3.81	377
15 GHz	$s_{circ}$	-4.61	3.74	385

### 3.3. Conclusion and Outlook

In my thesis I analyzed radio data of 11 BL Lac object of the Boston University 43 GHz sample with respect to their brightness temperature and diameter gradients. I compared the measured properties with the values predicted by [Blandford & Königl \(1979\)](#) and [Königl \(1981\)](#).

According to the jet models of [Blandford & Königl \(1979\)](#) the power law index  $l$  has to be  $l = 1$  and the power law index  $s$  has to be  $s = -2.5$  or vary between  $-1.4 > s > -3$  in the case of [Königl \(1981\)](#). As a main result of my work I found the index of the diameter gradient to be  $l \approx 0.91$  on average for all studied sources. The median is  $l \approx 0.78$  representing that 2200+420 shows a far larger index  $l$  than all other sources on scales  $d_{core} \gtrsim 2$  mas. Within the standard deviation of  $\sigma_l \approx 0.54$  it is found that  $\langle l \rangle < 1$ . Hence the case of a conical jet predicted by [Blandford & Königl \(1979\)](#) and [Königl \(1981\)](#) does not hold for the sources studied in this work, but a stronger collimation is observed on these scales. Fitting the brightness temperature gradient so far allows to argue that the measured indices  $s$  are consistent with  $-1.4 > s > -3$  as predicted by [Königl \(1981\)](#) for all sources except 2200+420. This holds for both models, the circular and the elliptical.

0219+428 shows an underlying power law but in addition an excesses in the brightness temperature gradient and at the same core distance a dip in the diameter gradient at a core distance of about 2 mas. Comparing my data with a study of 0219+428 performed at 15 GHz by Till Steinbring and kinematic study of 0219+428 performed by the MOJAVE team, this excess can be regarded as a stationary component, which does not move in time and contracts the jet at this position. In the region afterwards the jet expands with the same power law as before.

The source 2200+420 shows a significant deviation from the measured averages with respect to the power law indices  $l$  and  $s$ . At higher scales meaning for  $d_{core} \gtrsim 2$  mas both  $s$  and  $l$  are twice as precipitous. In conformity with data at 15 GHz the values are  $l \approx 2.3$  and  $s \approx -4.9$ . At this scales the jet opens stronger and faster and it is not possible to describe the jet with a conical geometry.

At a next step my data will be compared with data at other wavelengths to proof, whether the power law indices are frequency depended. In the group of Matthias Kadler there are already studies on the run especially the bachelor thesis of [Burd \(2014\)](#) and studies done by Till Steinbring. The data, being analyzed are taken out of the MOJAVE 15 GHz sample and of the 43 GHz sample of the Boston University. Some of the sources are present in both samples, so a comparison between the two frequency bands can be done.

Furthermore, the calculation of the errors according the fitted power law indices  $s$  and  $l$  has to be performed in great detail.

# A. Appendix

## A.1. Figures

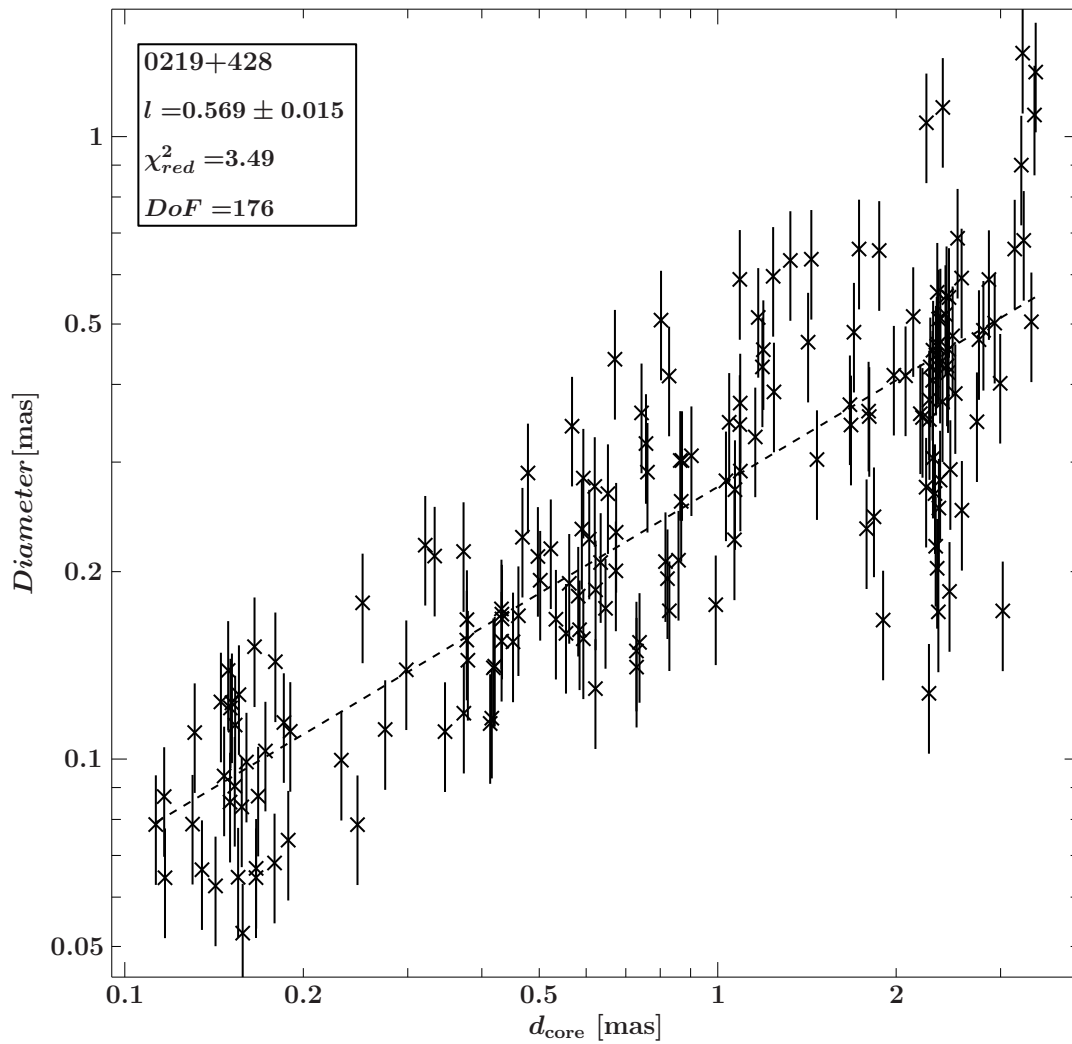


**Figure A.1.:** Diameter gradient, measured at 43GHz of 0219+428 fitted with a pure power law included excess, with power law index  $l$ ,  $\chi^2_{red}$ : reduced chi-squared, DoF: Degrees of freedom

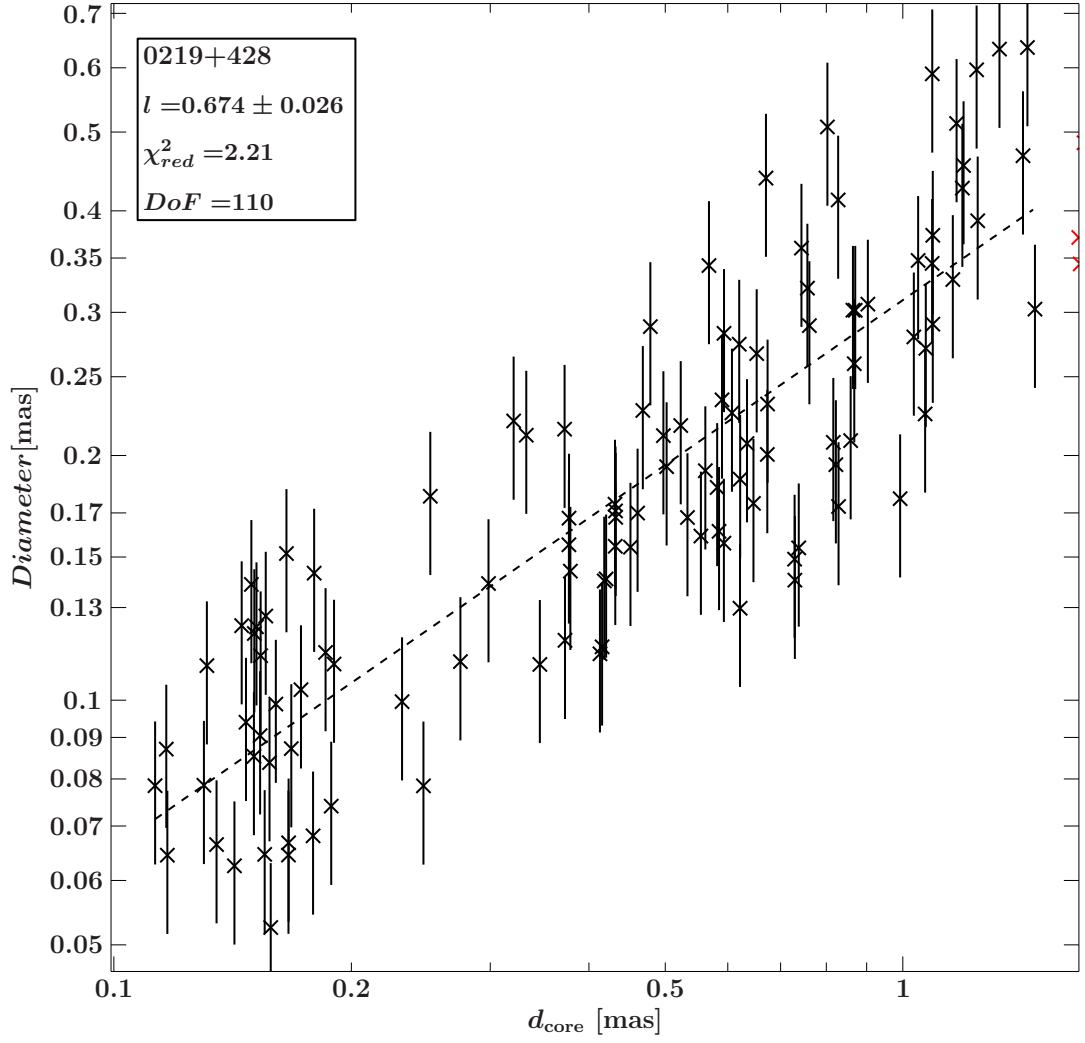


**Figure A.2.:** Diameter gradient, measured at 43GHz of 0219+428 fitted with a pure power law excluded excess, with power law index  $l$ ,  $\chi^2_{red}$ : reduced chi-squared, DoF: Degrees of freedom

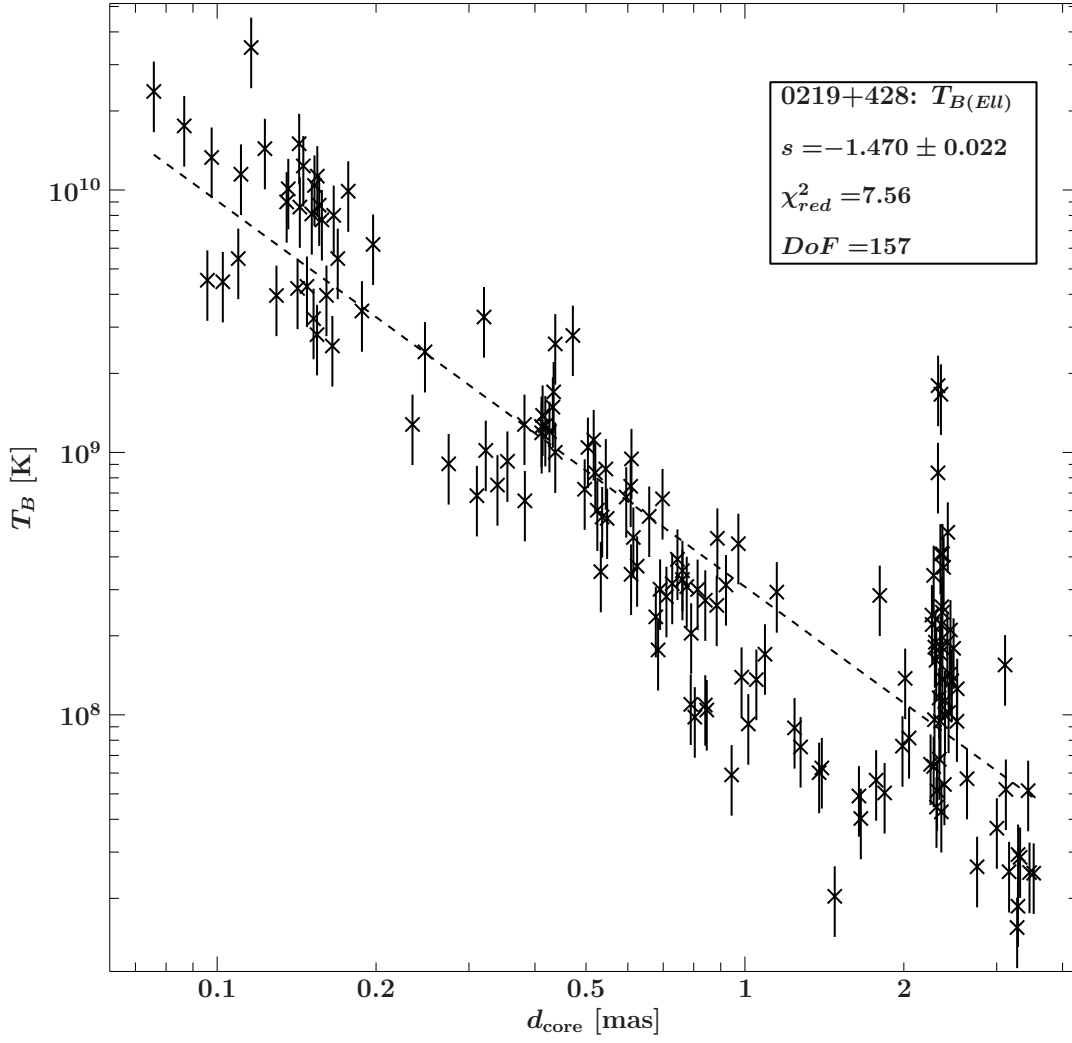


**Figure A.3.:** Brightness temperature gradient of the elliptic model, measured at 43GHz of 0219+428 fitted with a pure power law included excess, with power law index  $s$ ,  $\chi^2_{red}$ : reduced chi-squared, DoF: Degrees of freedom

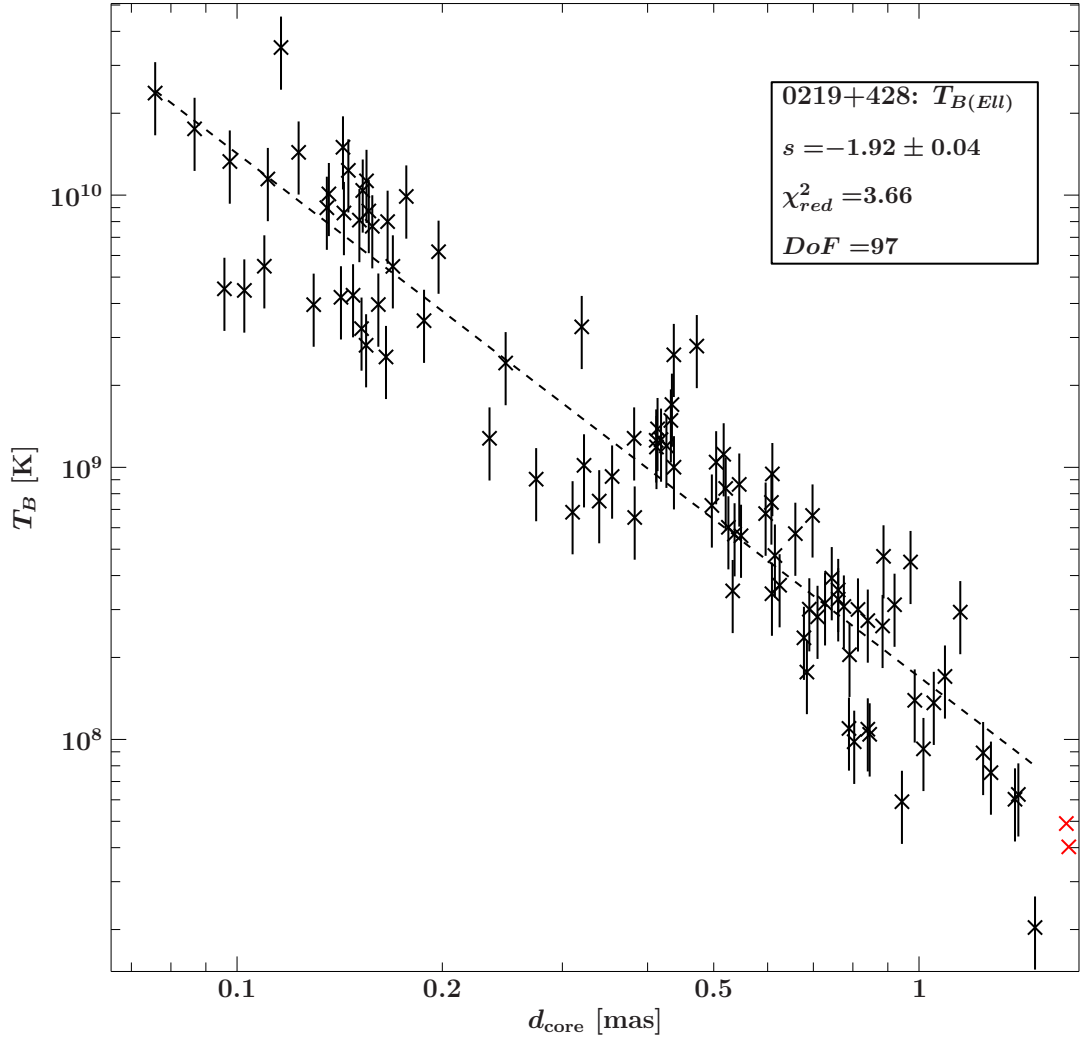


**Figure A.4.:** Brightness temperature gradient of the elliptical model, measured at 43GHz of 0219+428 fitted with a pure power law excluded excess, with power law index  $s$ ,  $\chi^2_{red}$ : reduced chi-squared, DoF: Degrees of freedom

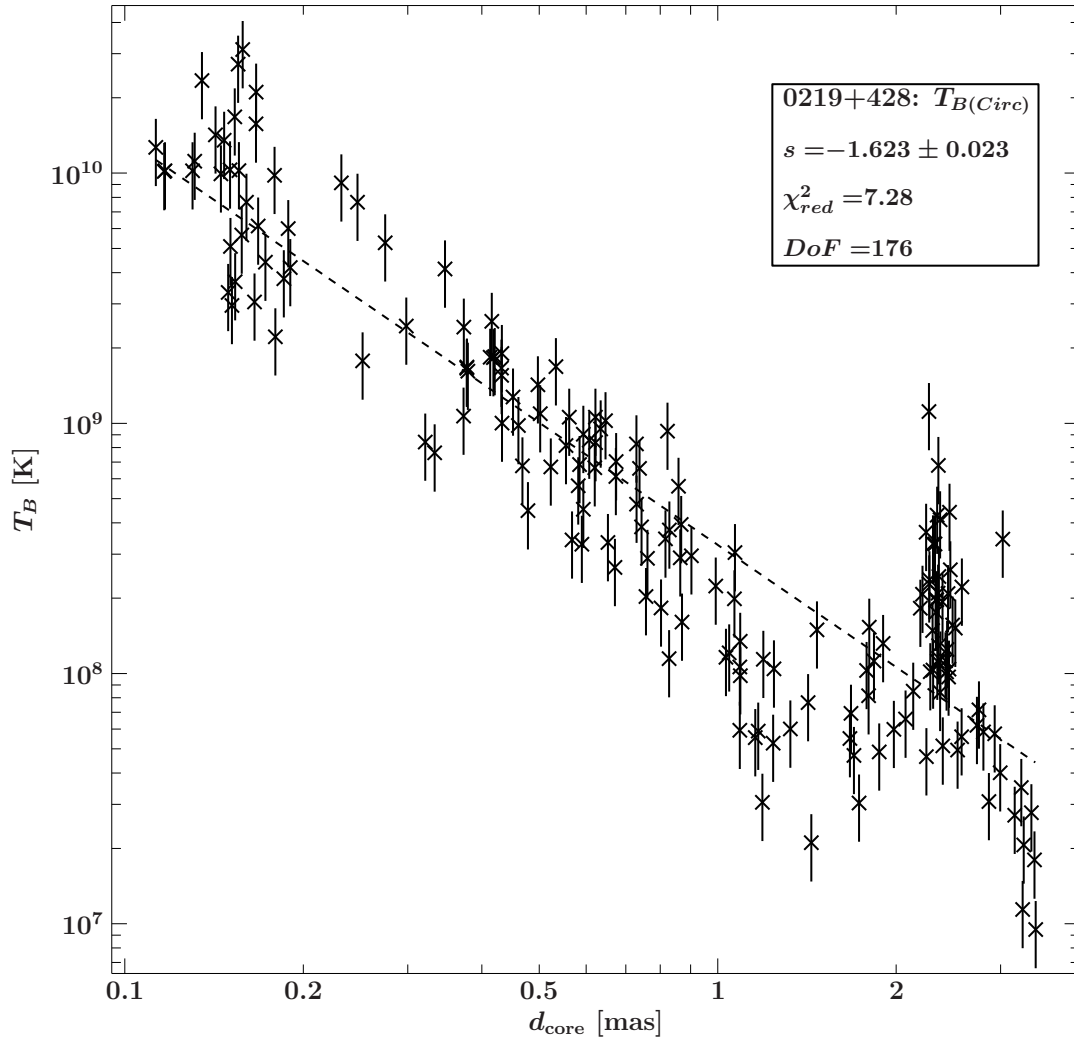


**Figure A.5.:** Brightness temperature gradient of the circular model, measured at 43GHz of 0219+428 fitted with a pure power law included excess, with power law index  $s$ ,  $\chi^2_{red}$ : reduced chi-squared, DoF: Degrees of freedom

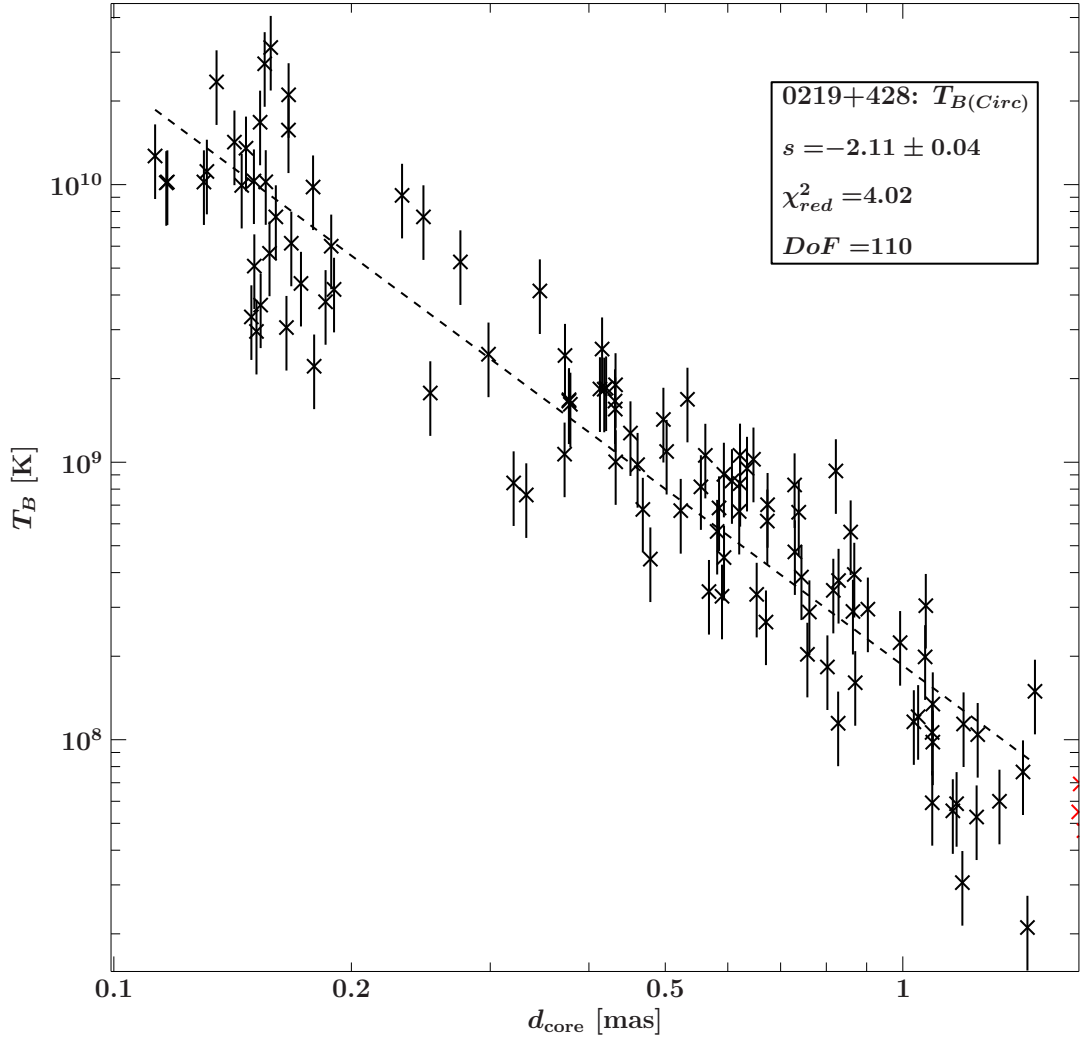


**Figure A.6.:** Brightness temperature gradient of the circular model, measured at 43GHz of 0219+428 fitted with a pure power law excluded excess, with power law index  $s$ ,  $\chi^2_{red}$ : reduced chi-squared, DoF: Degrees of freedom

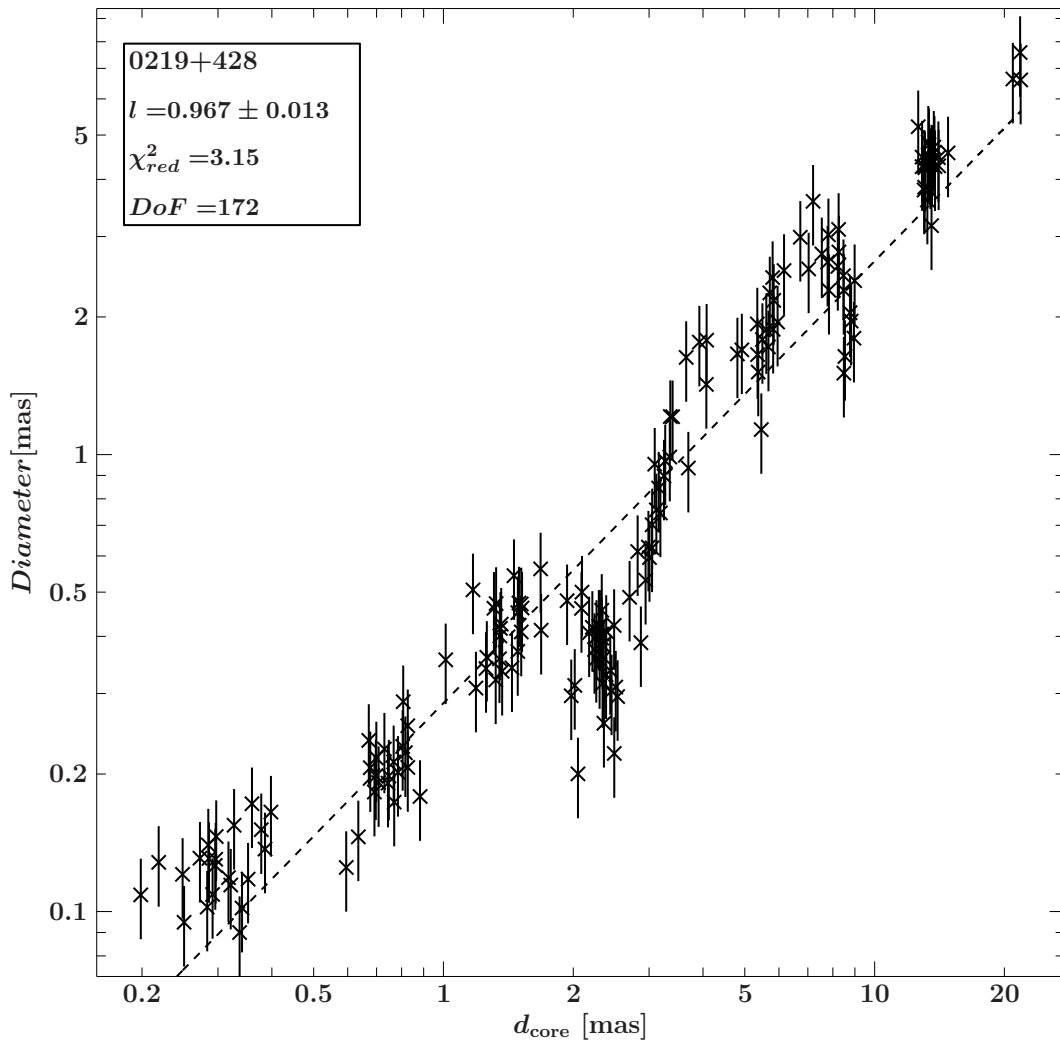


**Figure A.7.:** Diameter gradient, measured at 15GHz of 0219+428 fitted with a pure power law included excess, with power law index  $l$  by Till Steinbring,  $\chi^2_{red}$ : reduced chi-squared, DoF: Degrees of freedom

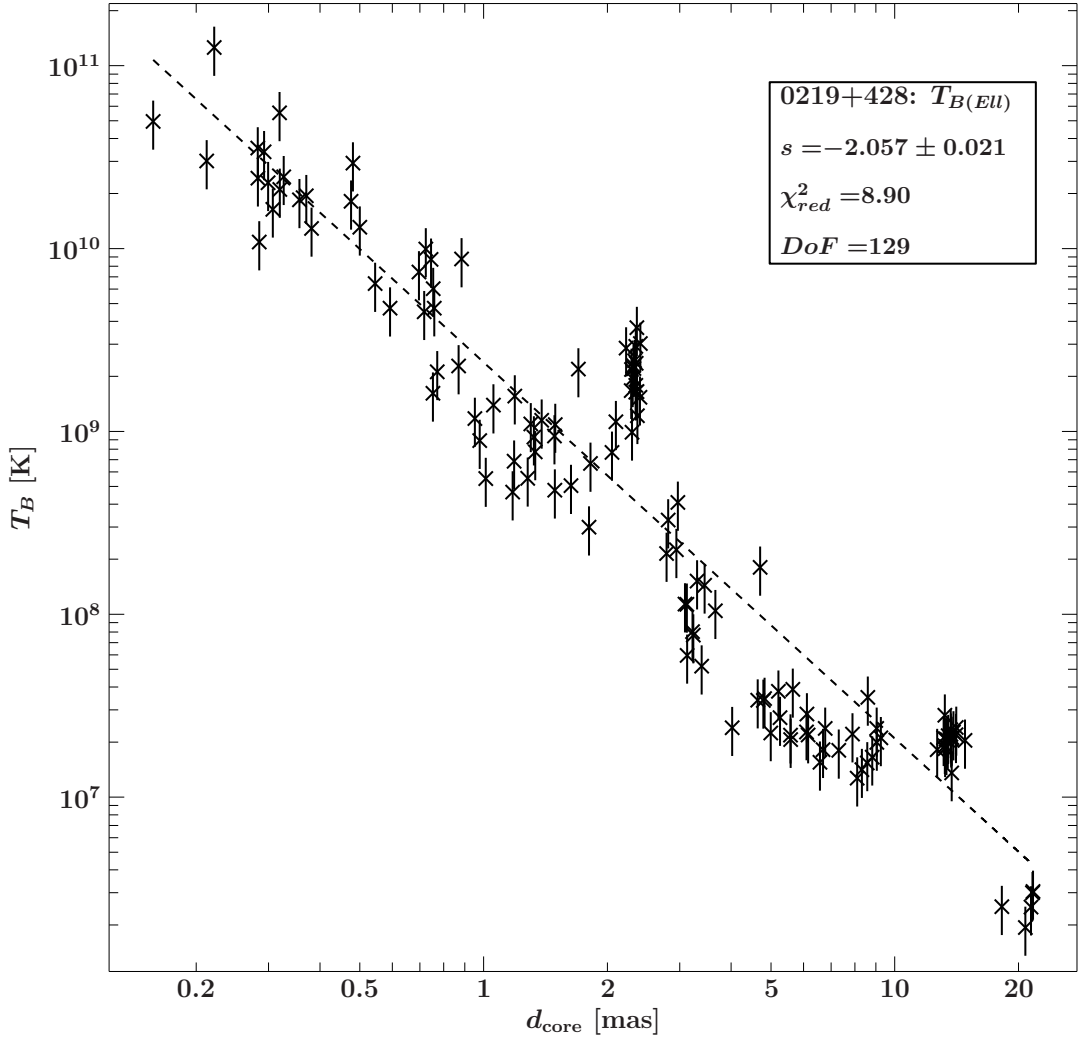


**Figure A.8.:** Brightness temperature gradient of the elliptical model, measured at 15GHz of 0219+428 fitted with a pure power law included excess by Till Steinbring, with power law index  $s$ ,  $\chi^2_{red}$ : reduced chi-squared, DoF: Degrees of freedom

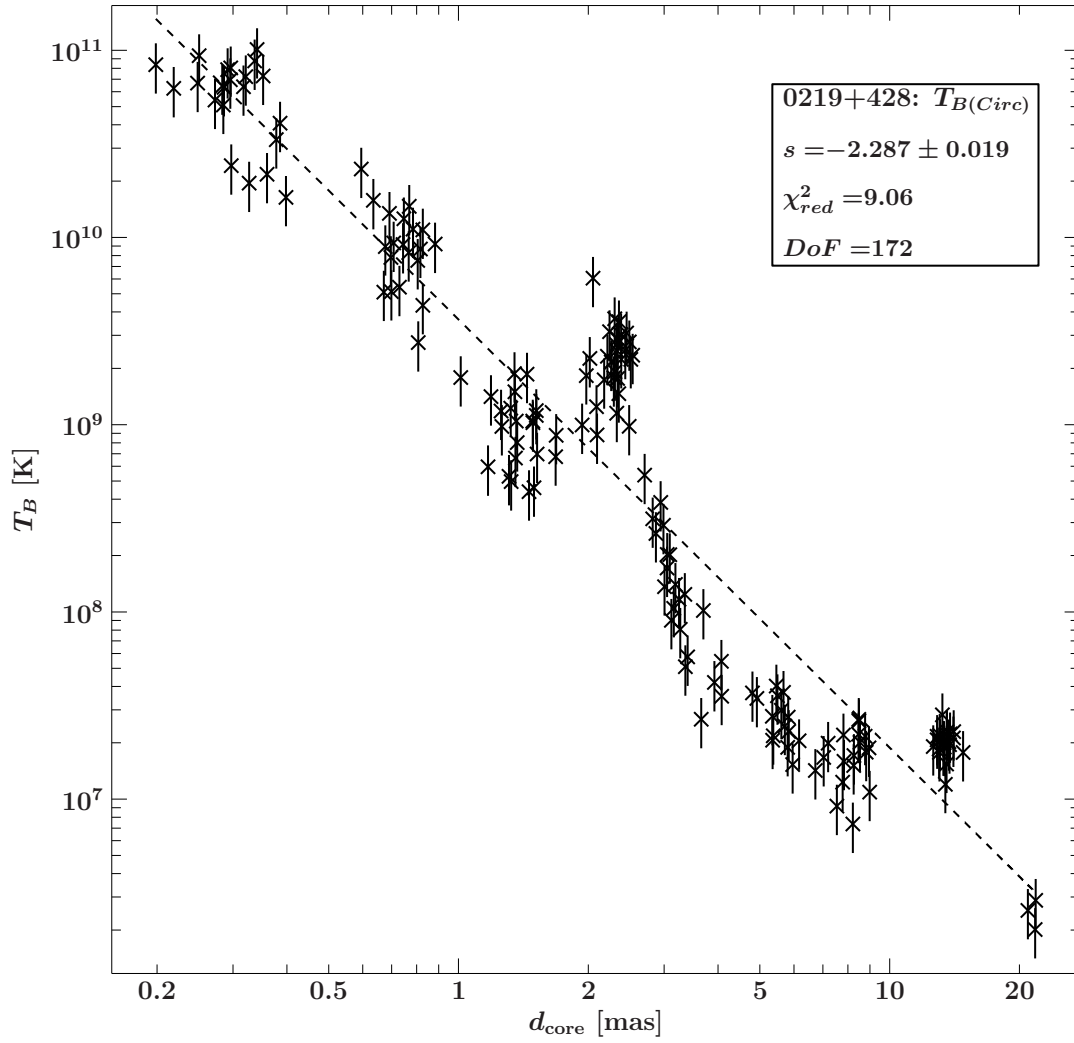


**Figure A.9.:** Brightness temperature gradient of the circular model, measured at 15GHz of 0219+428 fitted with a pure power law included excess by Till Steinbring, with power law index  $s$ ,  $\chi^2_{red}$ : reduced chi-squared, DoF: Degrees of freedom

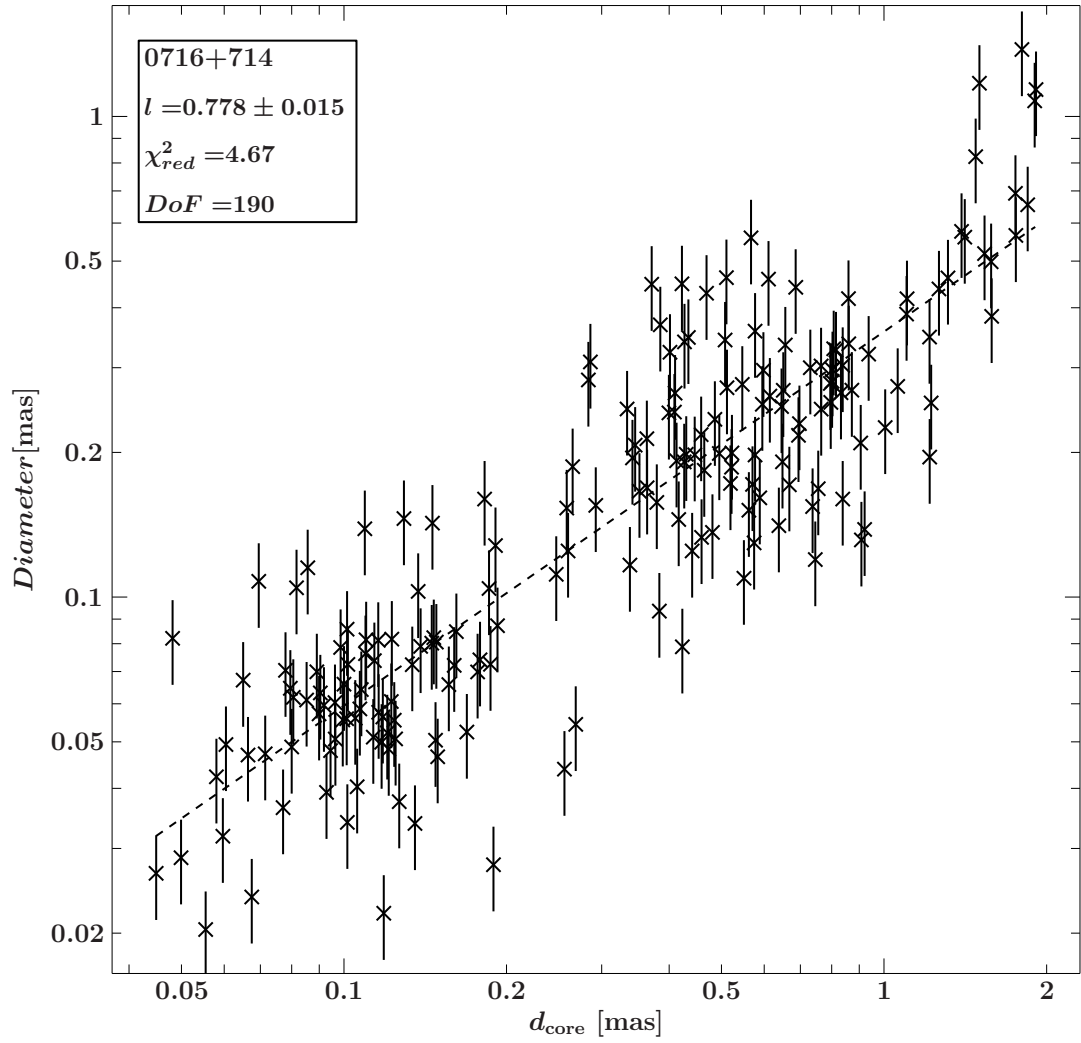


**Figure A.10.:** Diameter gradient of 0716+714 fitted with a pure power law, with power law index  $l$ ,  $\chi^2_{red}$ : reduced chi-squared, DoF: Degrees of freedom

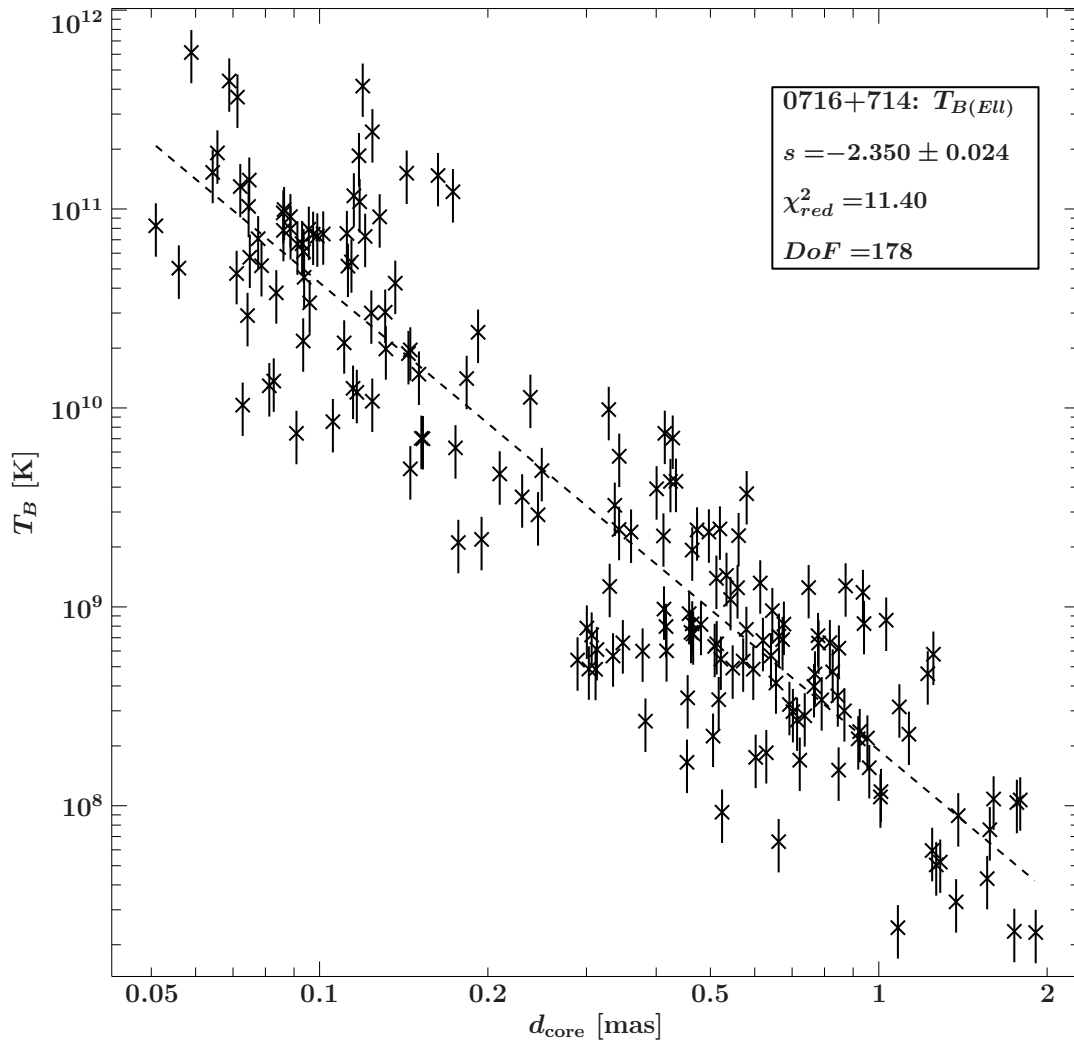


**Figure A.11.:** Brightness temperature gradient of the elliptic model of 0716+714 fitted with a pure power law, with power law index  $s$ ,  $\chi^2_{red}$ : reduced chi-squared, DoF: Degrees of freedom

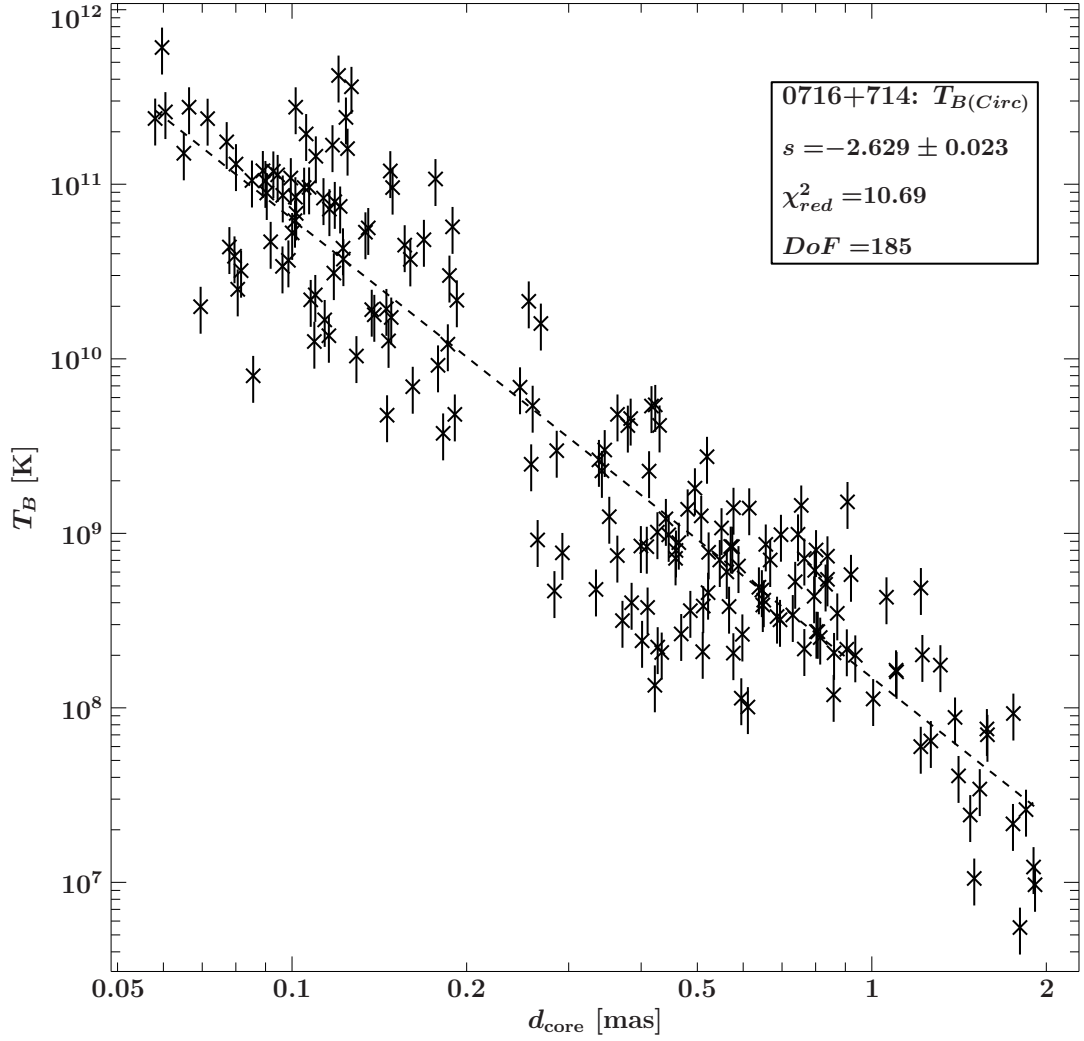


**Figure A.12.:** Brightness temperature gradient of the circular model of 0716+714 fitted with a pure power law, with power law index  $s$ ,  $\chi^2_{red}$ : reduced chi-squared, DoF: Degrees of freedom

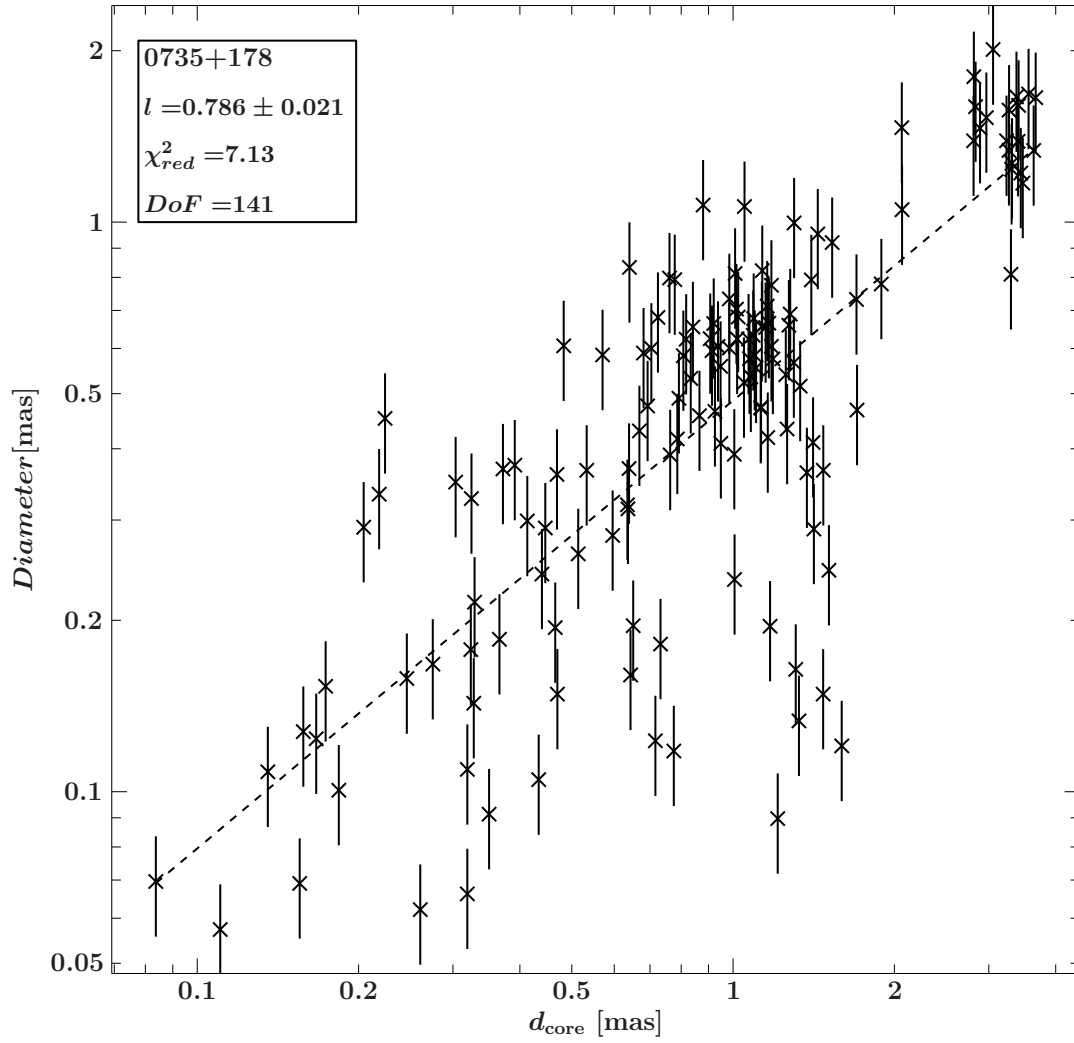


**Figure A.13.:** Diameter gradient of 0735+178 fitted with a pure power law, with power law index  $l$ ,  $\chi^2_{red}$ : reduced chi-squared, DoF: Degrees of freedom

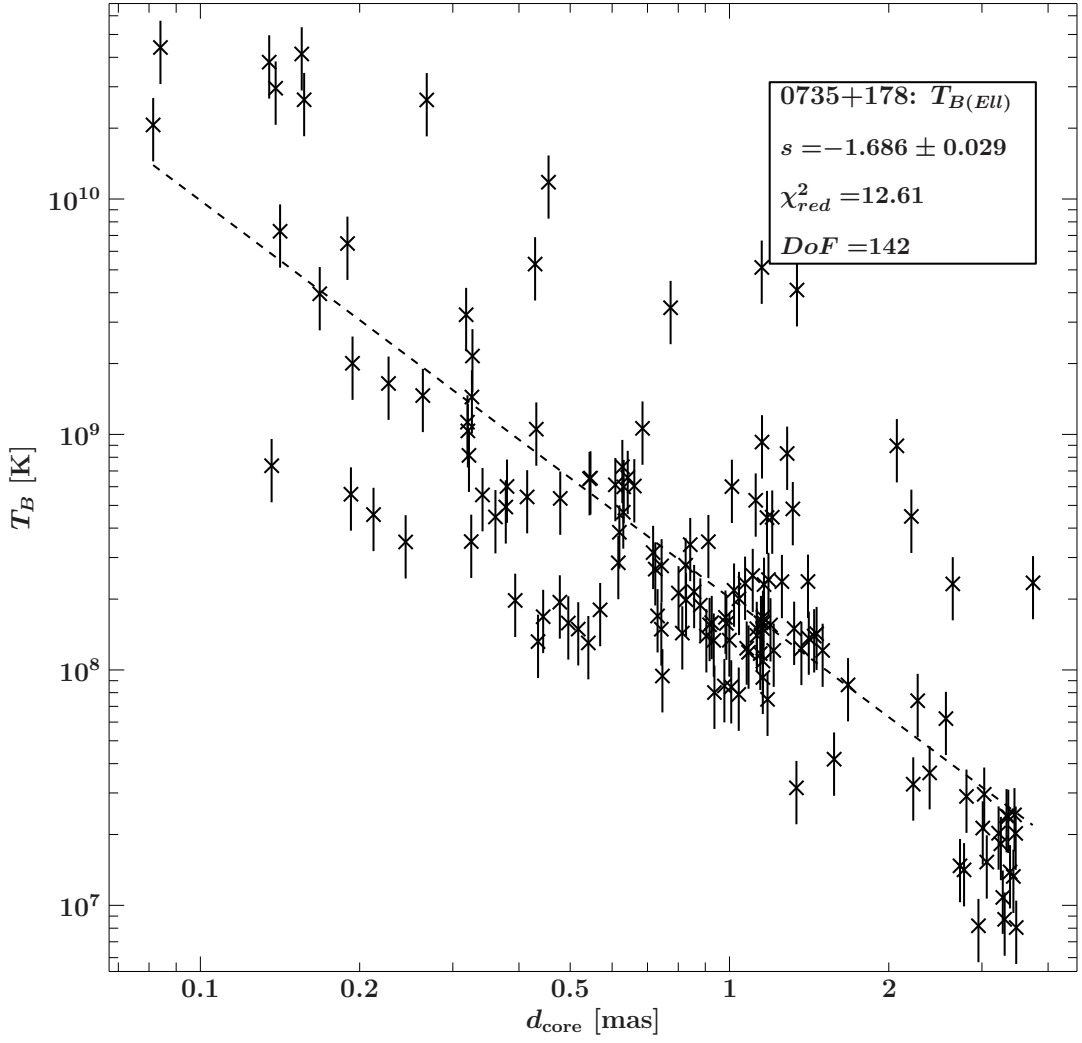


**Figure A.14.:** Brightness temperature gradient of the elliptical model of 0735+178 fitted with a pure power law, with power law index  $s$ ,  $\chi^2_{red}$ : reduced chi-squared, DoF: Degrees of freedom

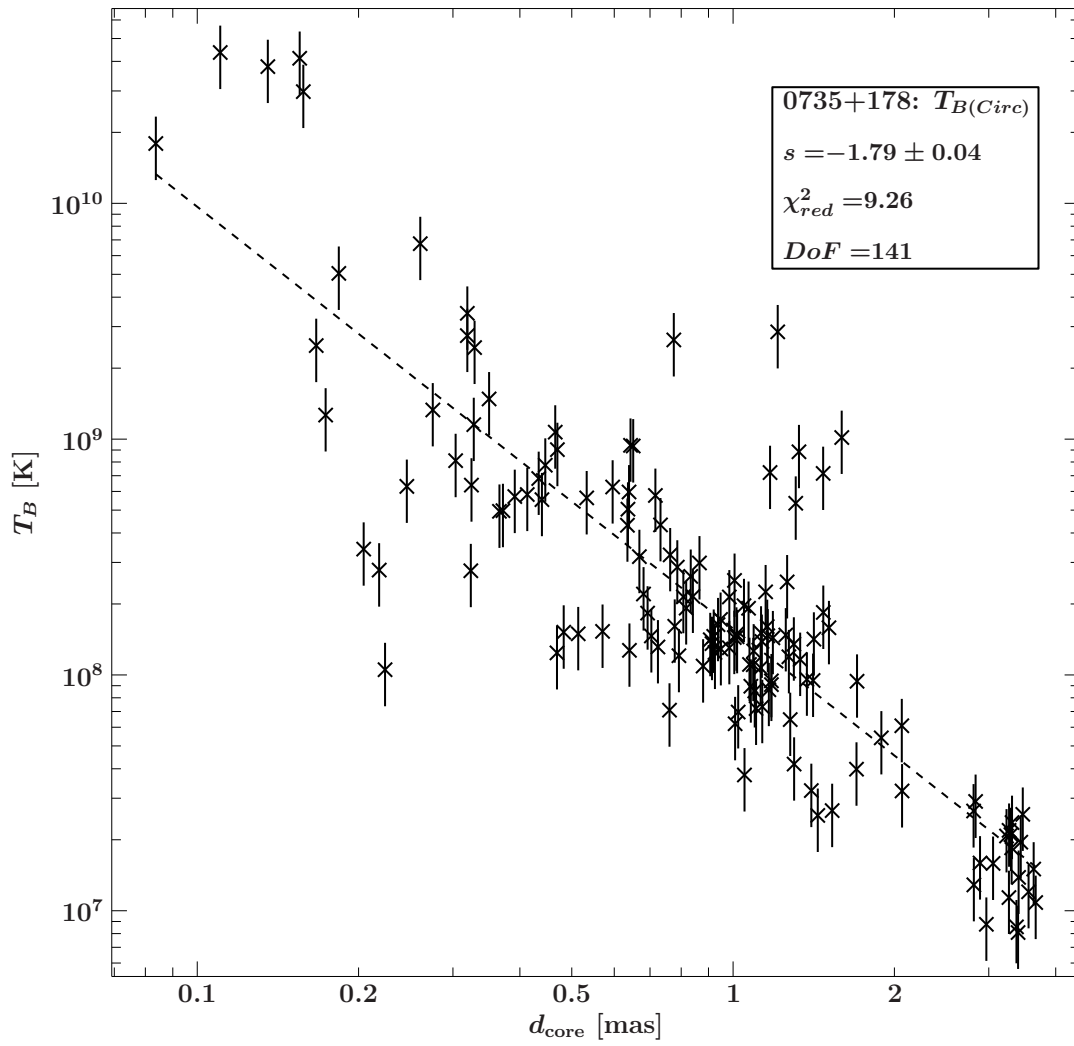


**Figure A.15.:** Brightness temperature gradient of the circular model of 0735+178 fitted with a pure power law, with power law index  $s$ ,  $\chi^2_{red}$ : reduced chi-squared, DoF: Degrees of freedom

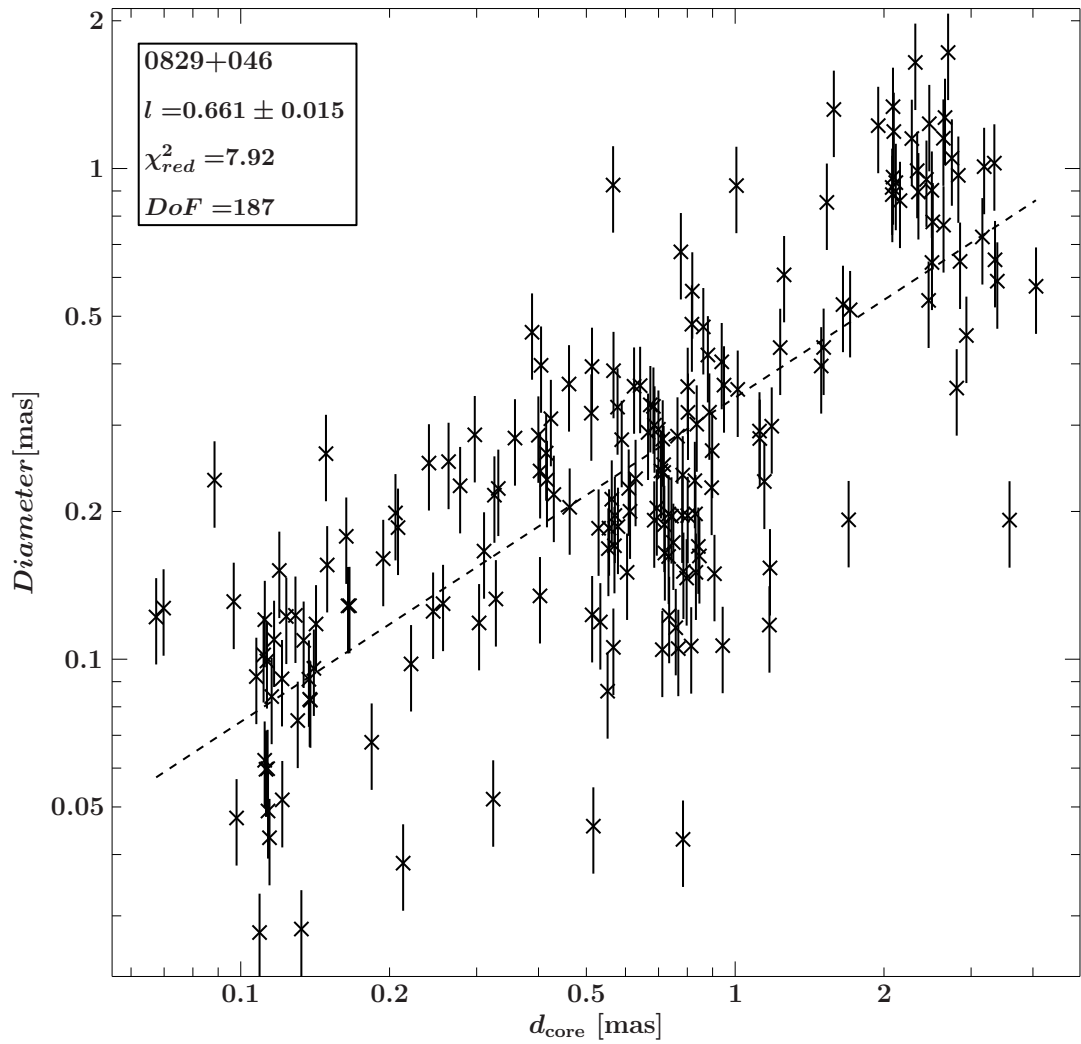


**Figure A.16.:** Diameter gradient of 0829+046 fitted with a pure power law, with power law index  $l$ ,  $\chi^2_{red}$ : reduced chi-squared, DoF: Degrees of freedom

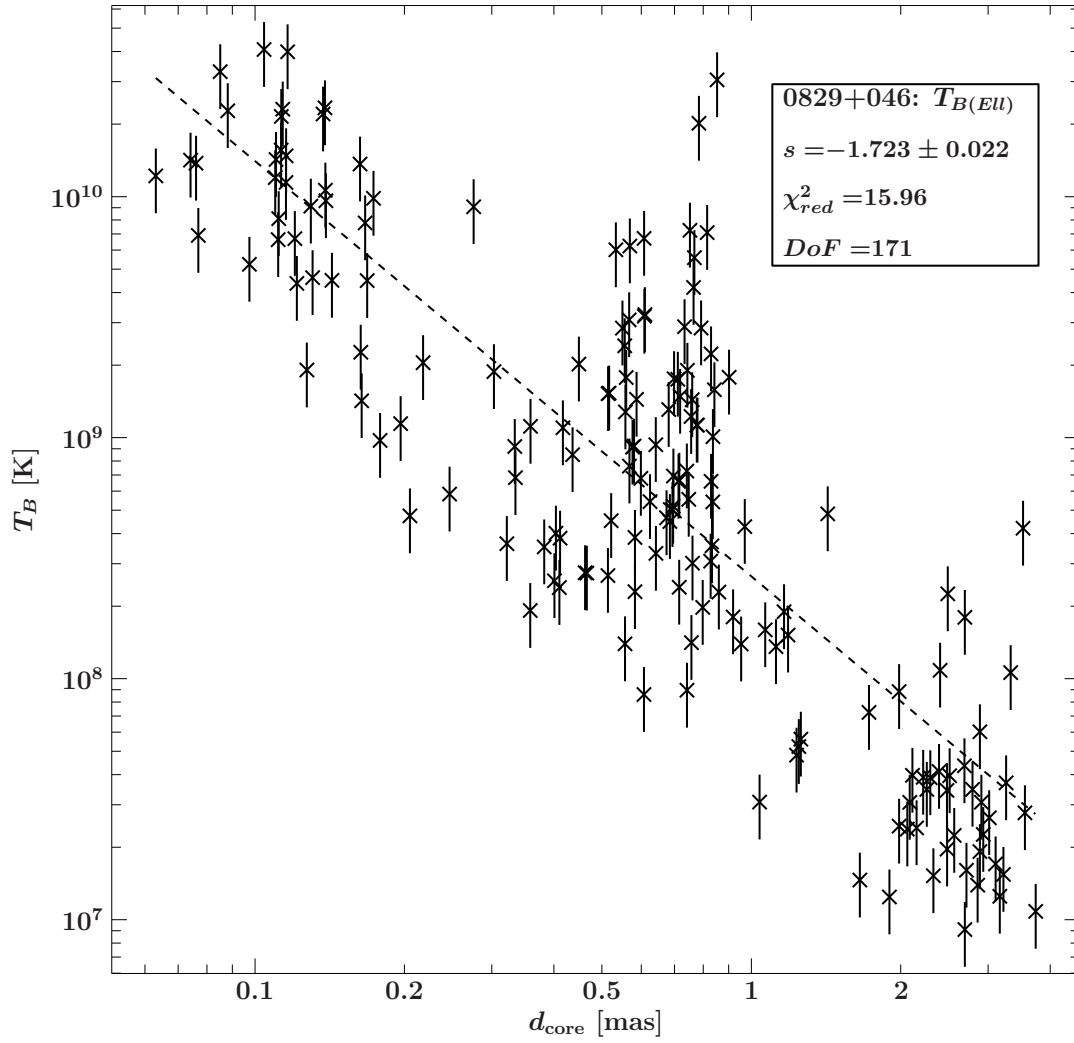


**Figure A.17.:** Brightness temperature gradient of the elliptic model of 0829+046 fitted with a pure power law, with power law index  $s$ ,  $\chi^2_{red}$ : reduced chi-squared, DoF: Degrees of freedom

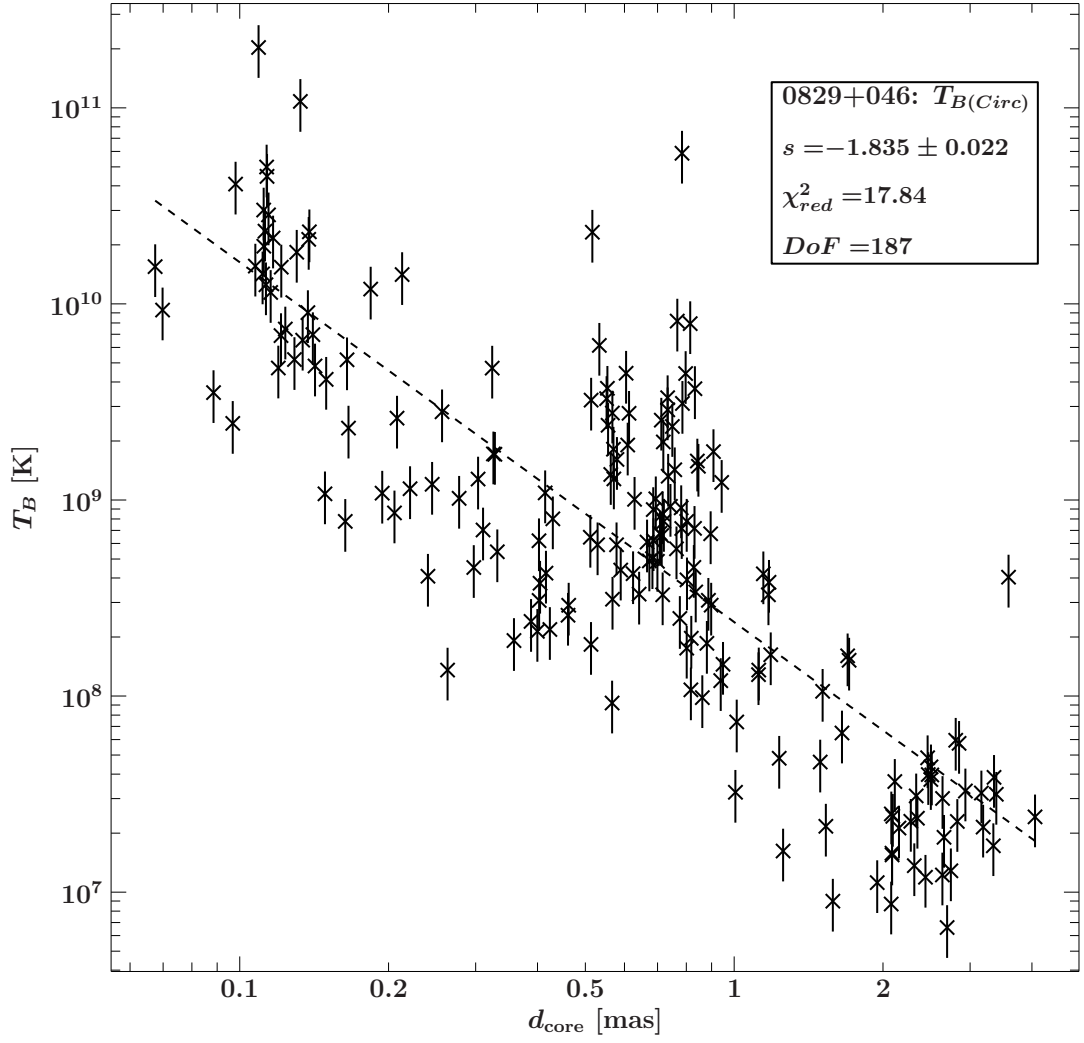


**Figure A.18.:** Brightness temperature gradient of the circular model of 0829+046 fitted with a pure power law, with power law index  $s$ ,  $\chi^2_{red}$ : reduced chi-squared, DoF: Degrees of freedom

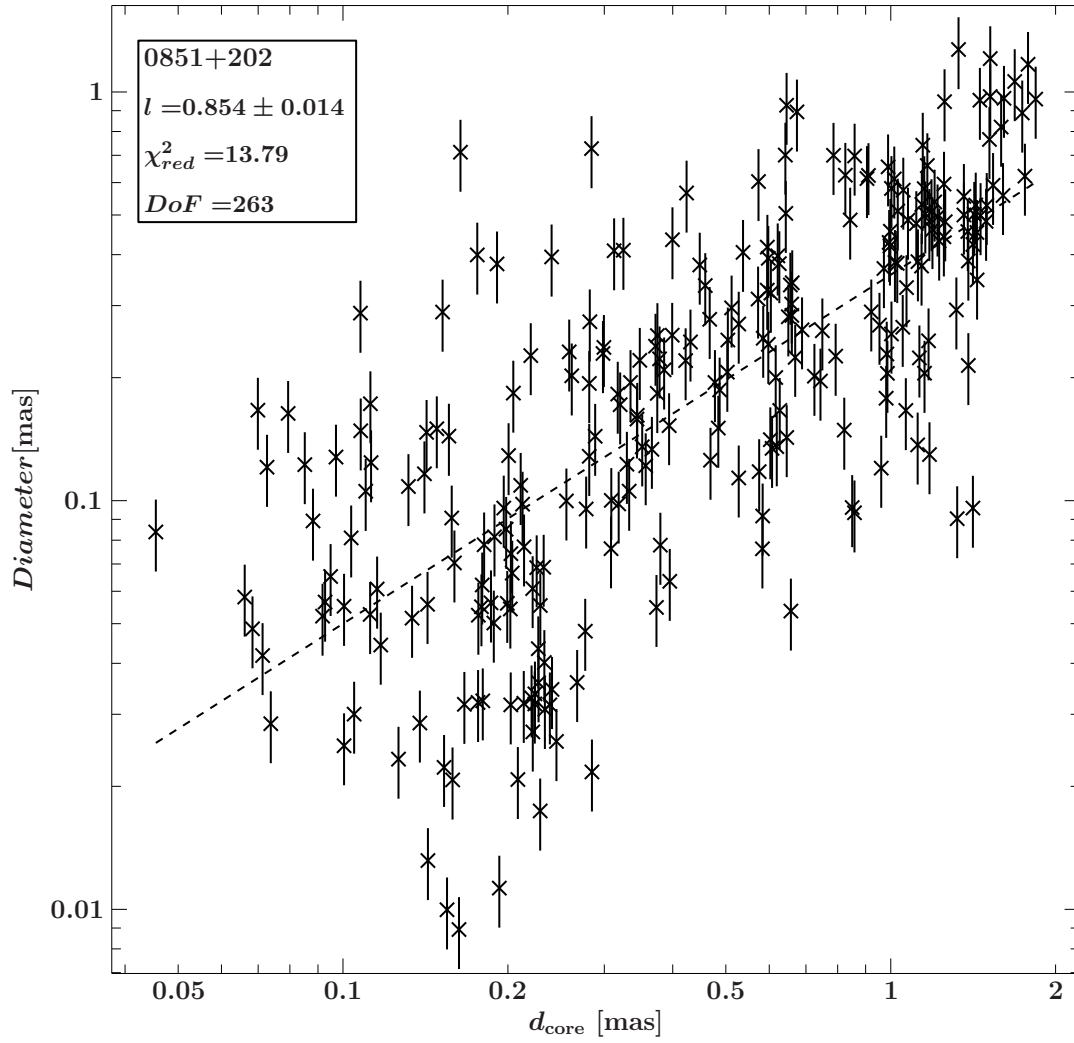


**Figure A.19.:** Diameter gradient of 0851+202 fitted with a pure power law, with power law index  $l$ ,  $\chi^2_{red}$ : reduced chi-squared, DoF: Degrees of freedom

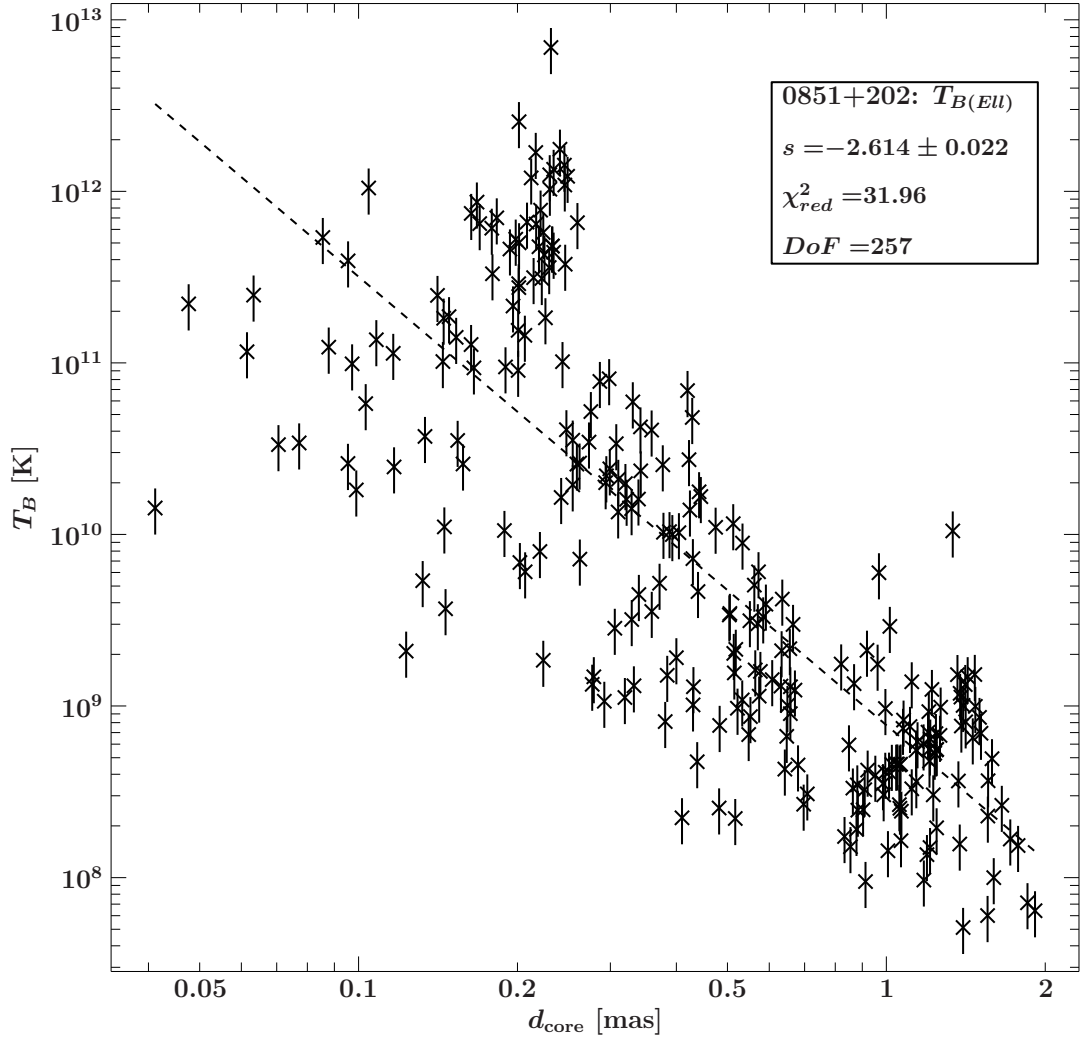


**Figure A.20.:** Brightness temperature gradient of the elliptical model of 0851+202 fitted with a pure power law, with power law index  $s$ ,  $\chi^2_{red}$ : reduced chi-squared, DoF: Degrees of freedom

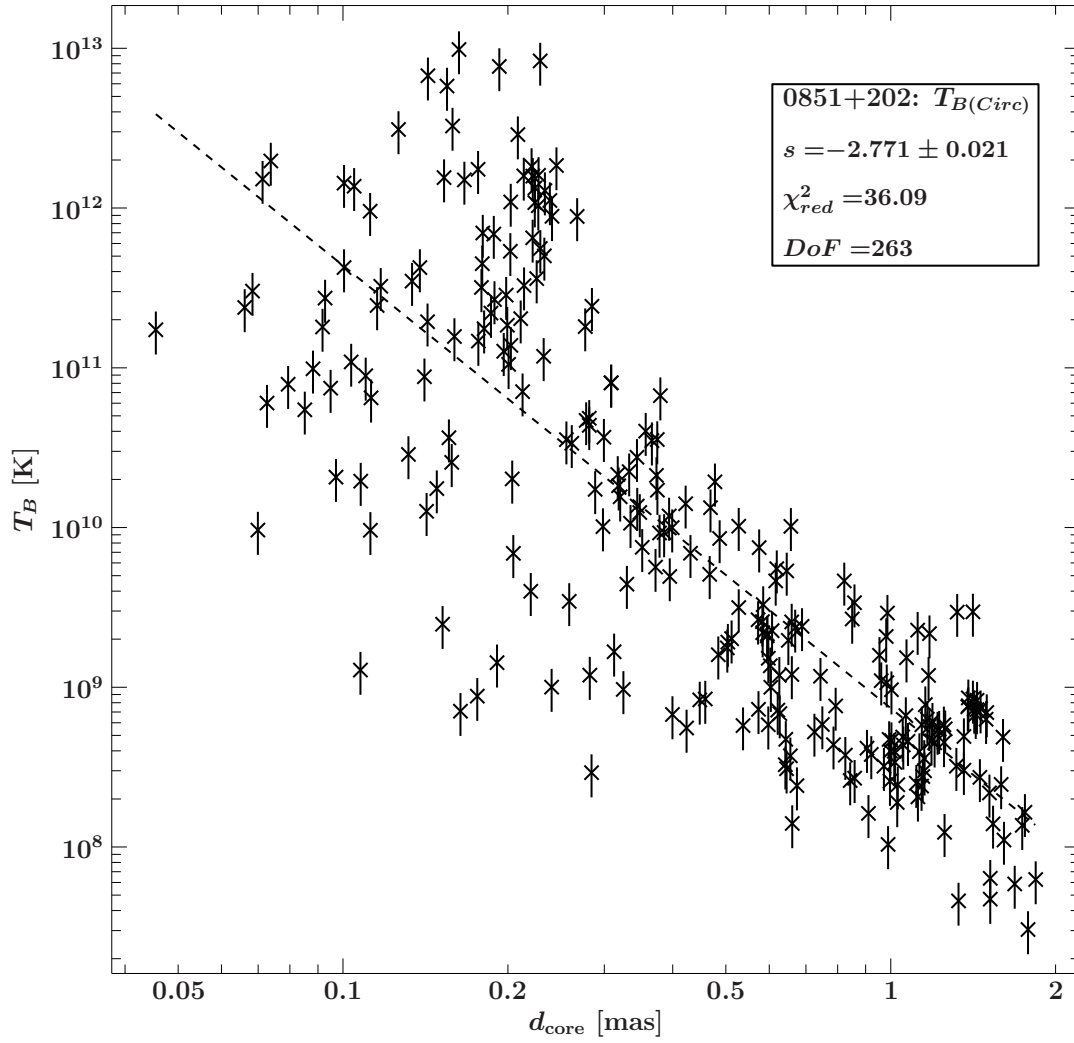


**Figure A.21.:** Brightness temperature gradient of the circular model of 0851+202 fitted with a pure power law, with power law index  $s$ ,  $\chi^2_{red}$ : reduced chi-squared, NDoF: Degrees of freedom

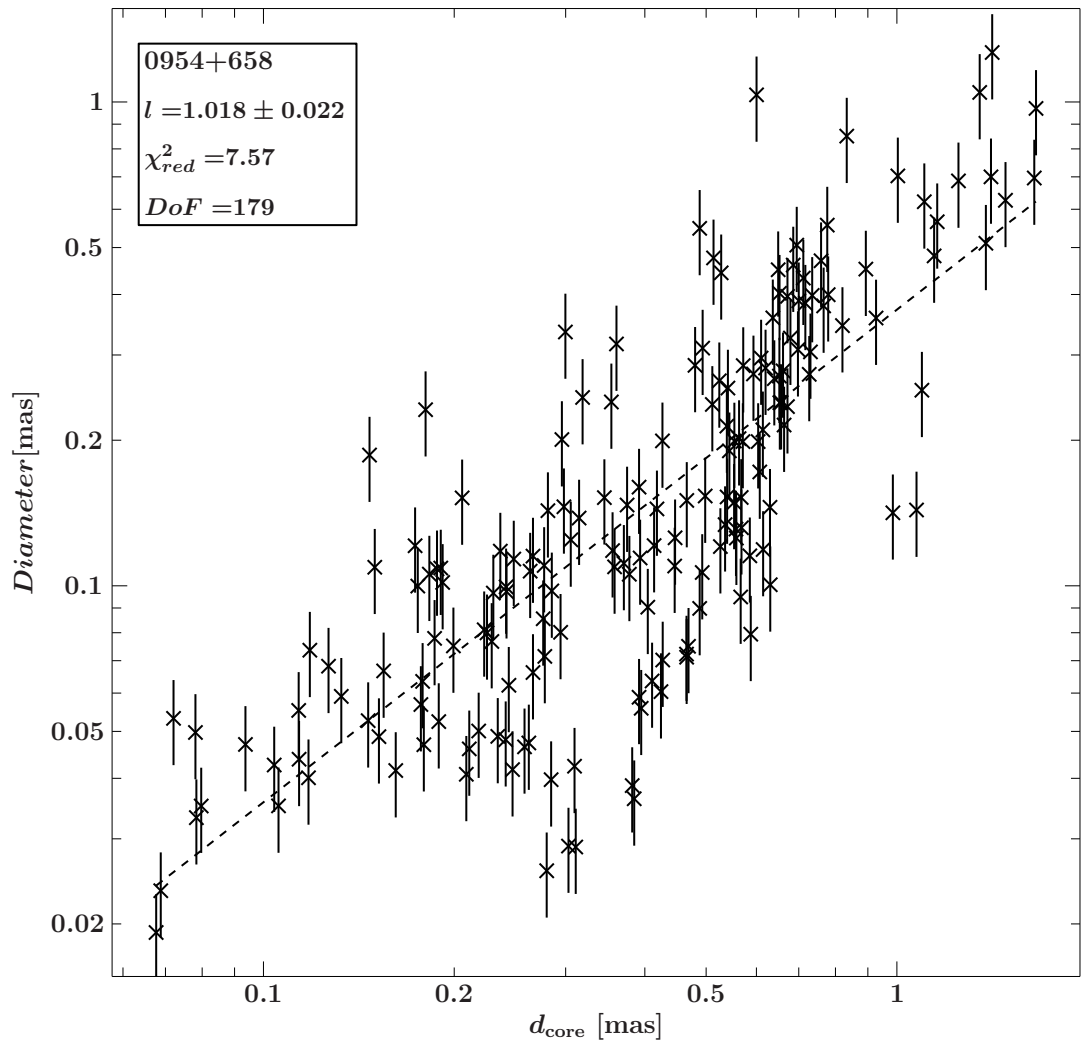


**Figure A.22.:** Diameter gradient of 0954+658 fitted with a pure power law, with power law index  $l$ ,  $\chi^2_{red}$ : reduced chi-squared, DoF: Degrees of freedom

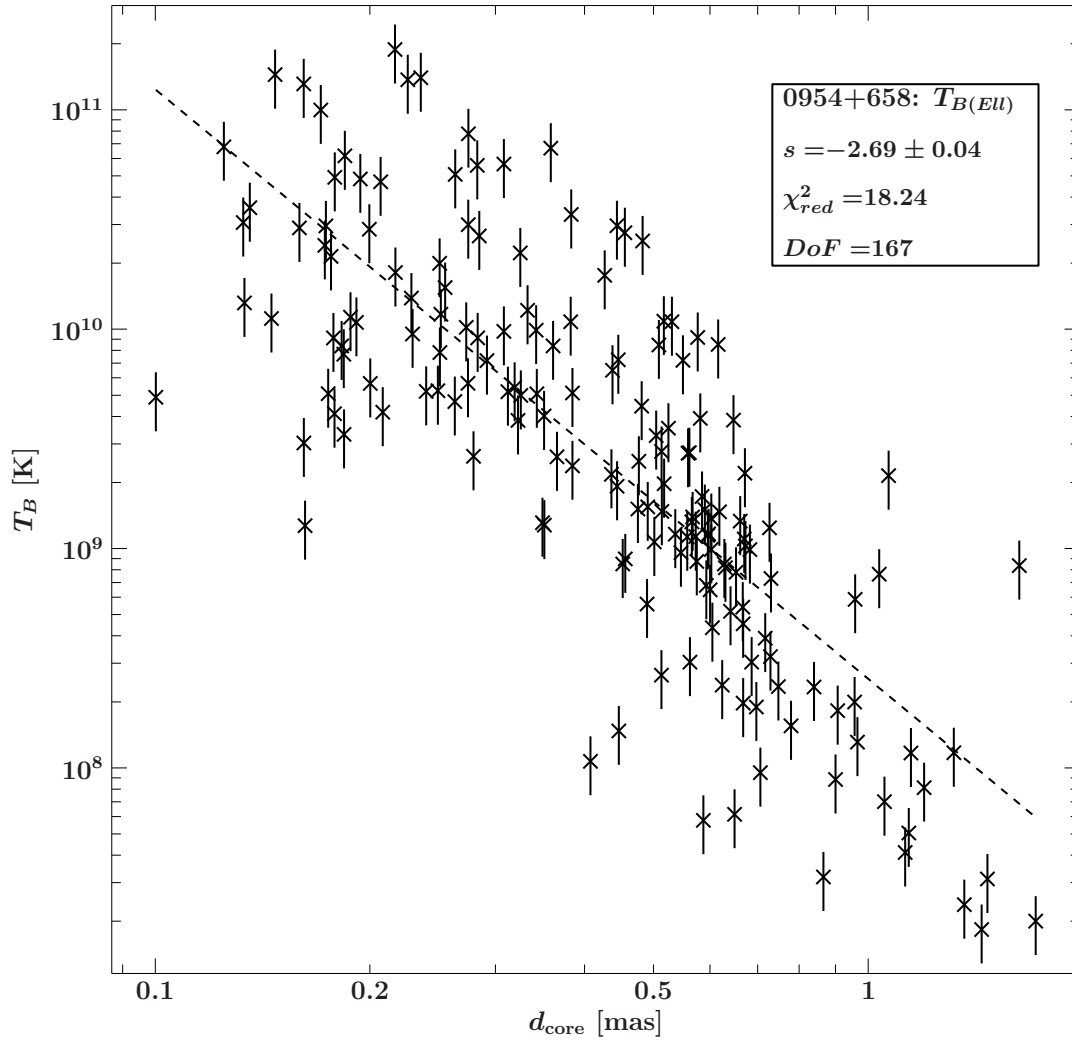


**Figure A.23.:** Brightness temperature gradient of the elliptical model of 0954+658 fitted with a pure power law, with power law index  $s$ ,  $\chi^2_{red}$ : reduced chi-squared, DoF: Degrees of freedom

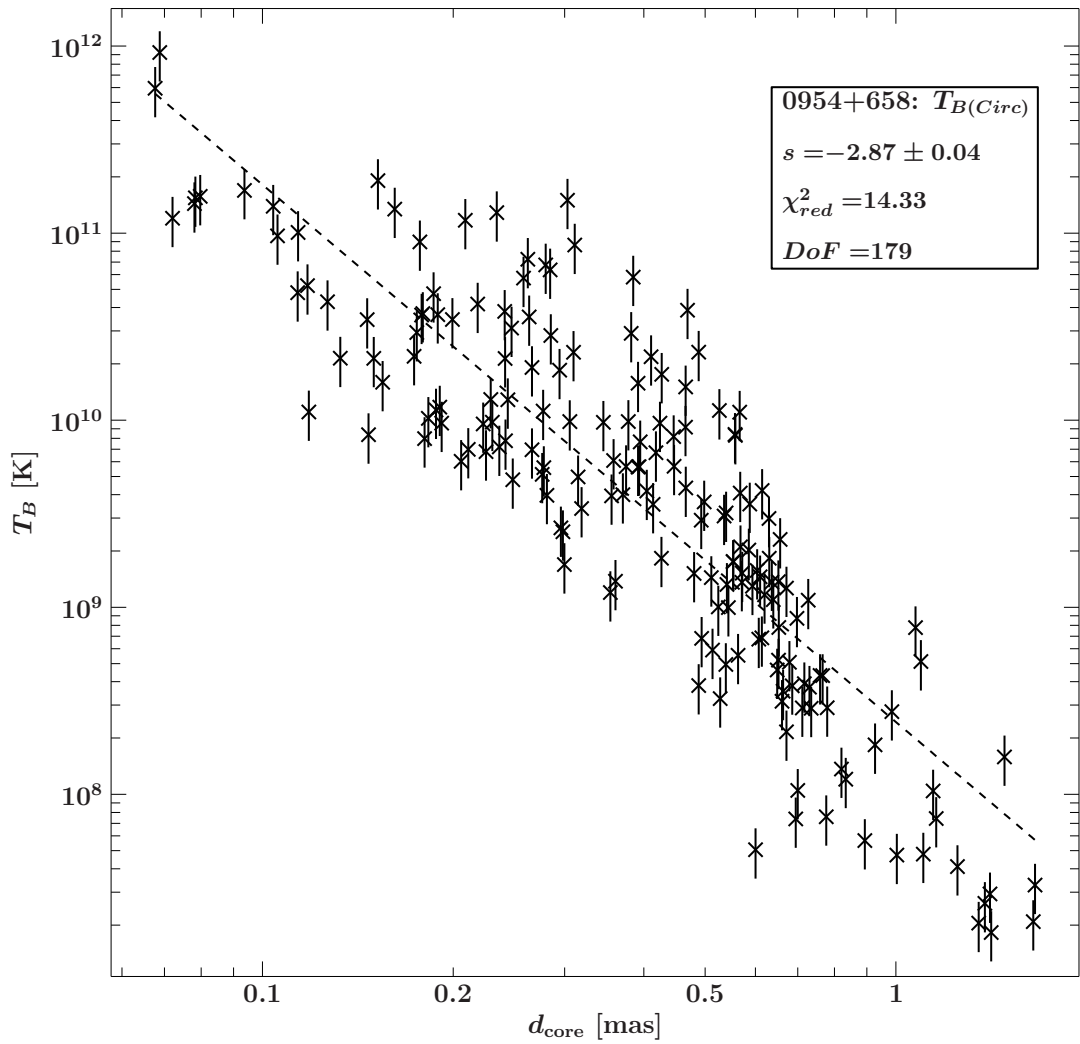


**Figure A.24.:** Brightness temperature gradient of the circular model of 0954+658 fitted with a pure power law, with power law index  $s$ ,  $\chi^2_{red}$ : reduced chi-squared, DoF: Degrees of freedom

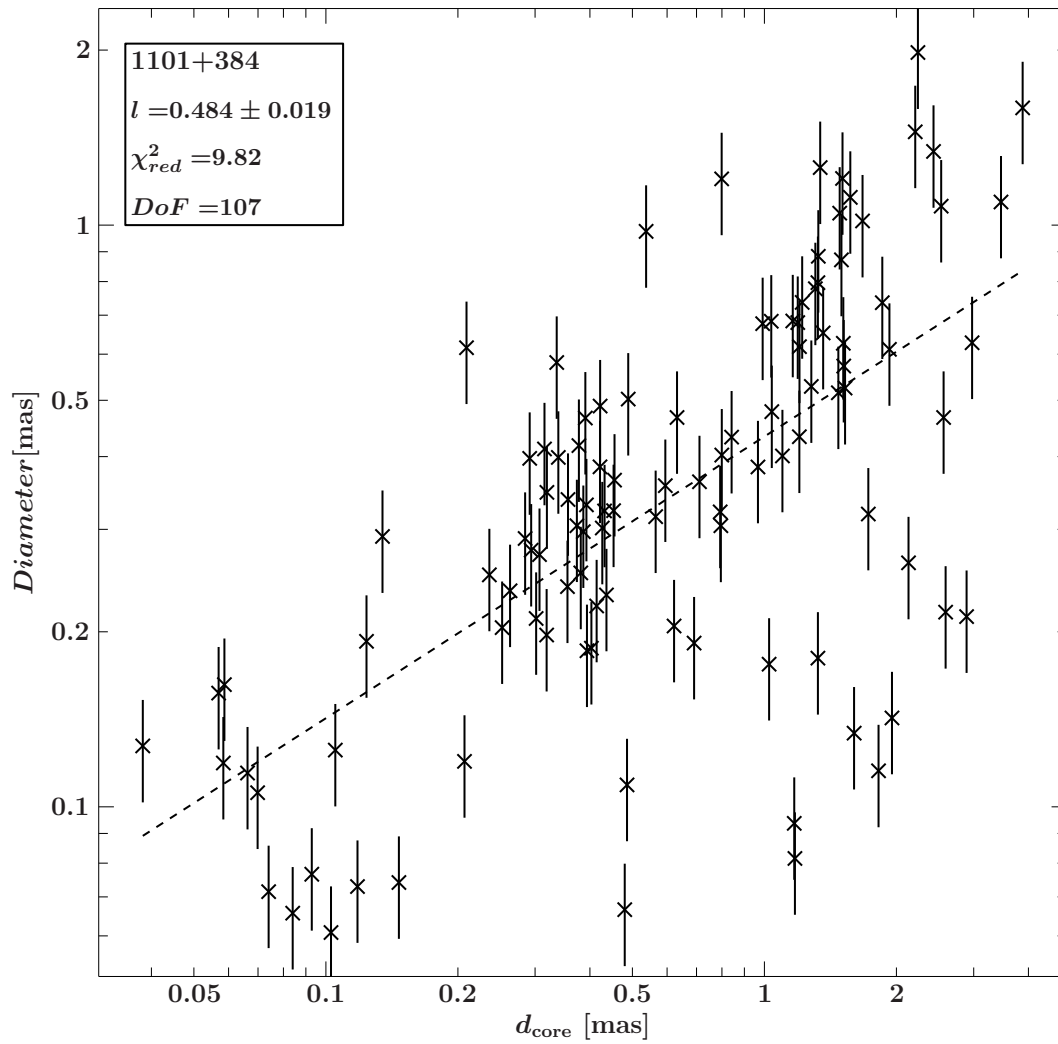


**Figure A.25.:** Diameter gradient of 1101+384 measured at 43 GHz and fitted with a pure power law, with power law index  $l$ ,  $\chi^2_{\text{red}}$ : reduced chi-squared, DoF: Degrees of freedom

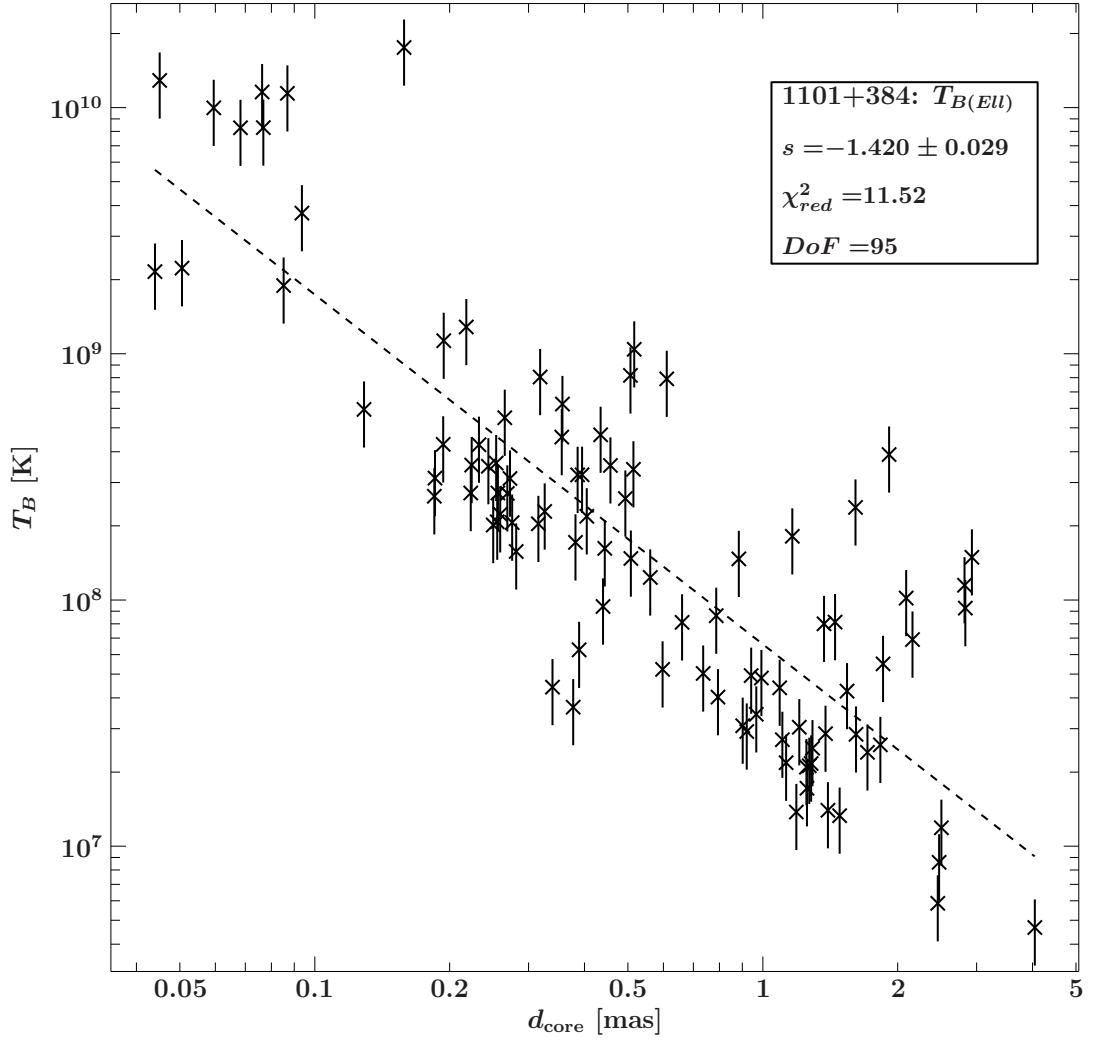


**Figure A.26.:** Brightness temperature gradient of the elliptic model of 1101+384 measured at 43 GHz and fitted with a pure power law, with power law index  $s$ ,  $\chi^2_{red}$ : reduced chi-squared, DoF: Degrees of freedom

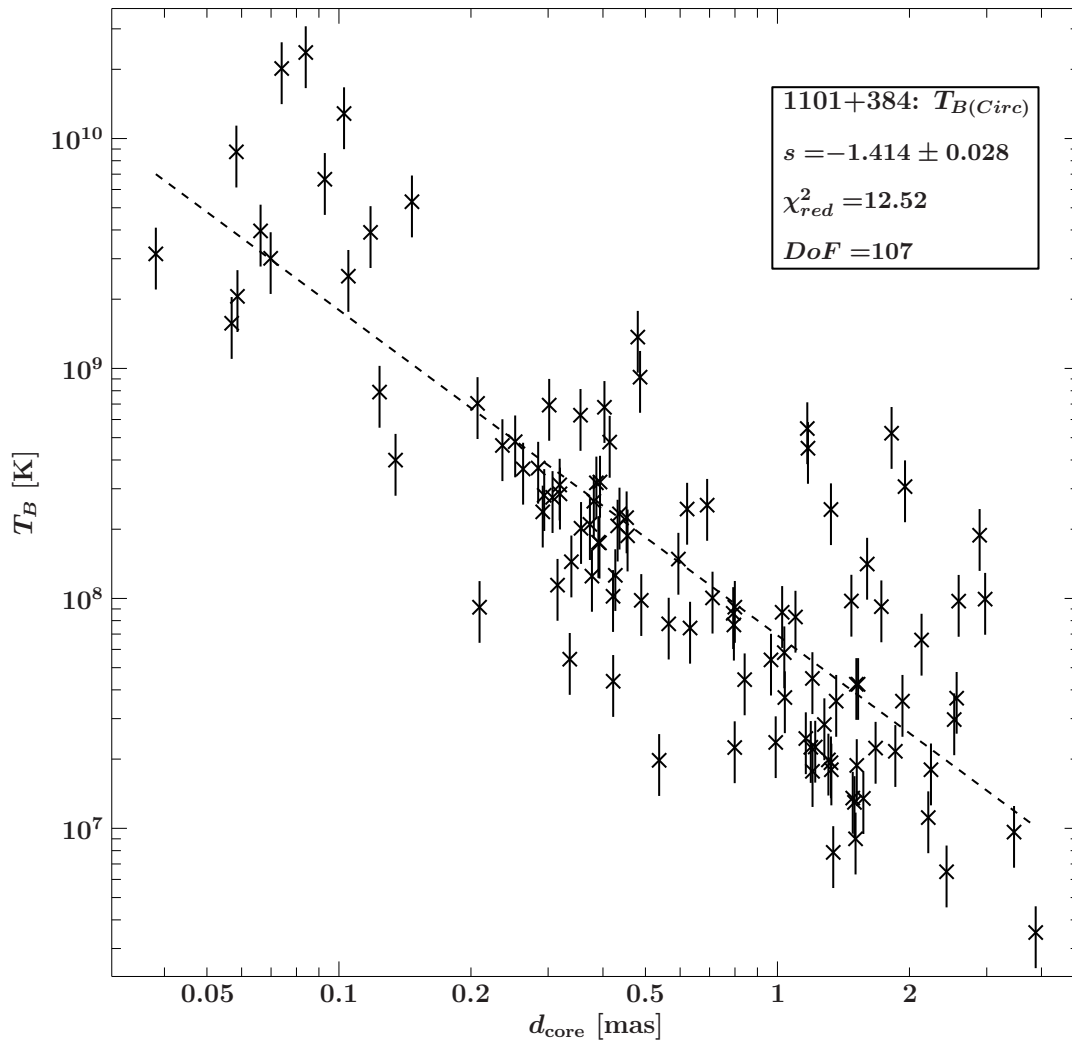


**Figure A.27.:** Brightness temperature gradient of the circular model of 1101+384 measured at 43 GHz and fitted with a pure power law, with power law index  $s$ ,  $\chi^2_{red}$ : reduced chi-squared, DoF: Degrees of freedom

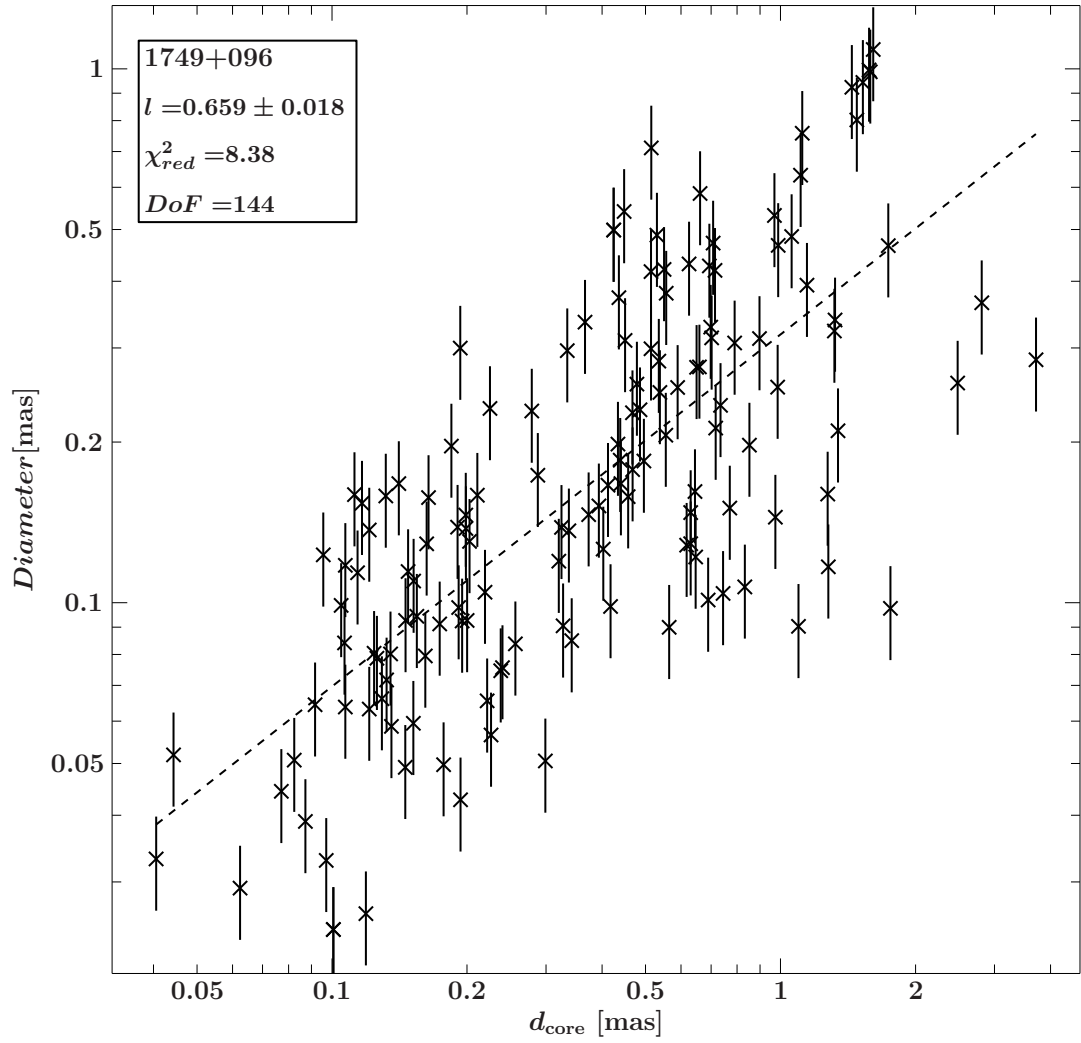


**Figure A.28.:** Diameter gradient of 1749+096 fitted with a pure power law, with power law index  $l$ ,  $\chi^2_{red}$ : reduced chi-squared, DoF: Degrees of freedom

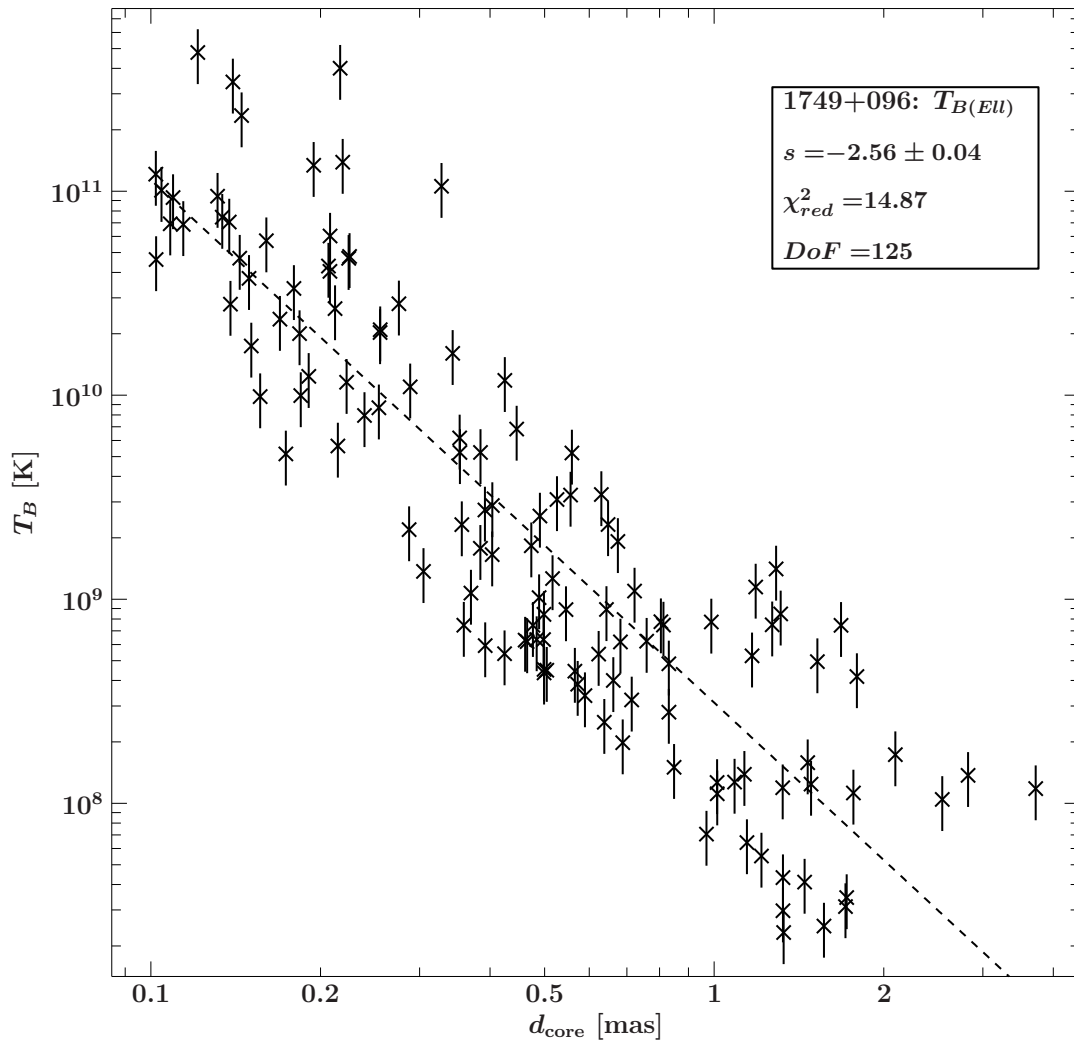


**Figure A.29.:** Brightness temperature gradient of the elliptical model of 1749+096 fitted with a pure power law, with power law index  $s$ ,  $\chi^2_{red}$ : reduced chi-squared, DoF: Degrees of freedom

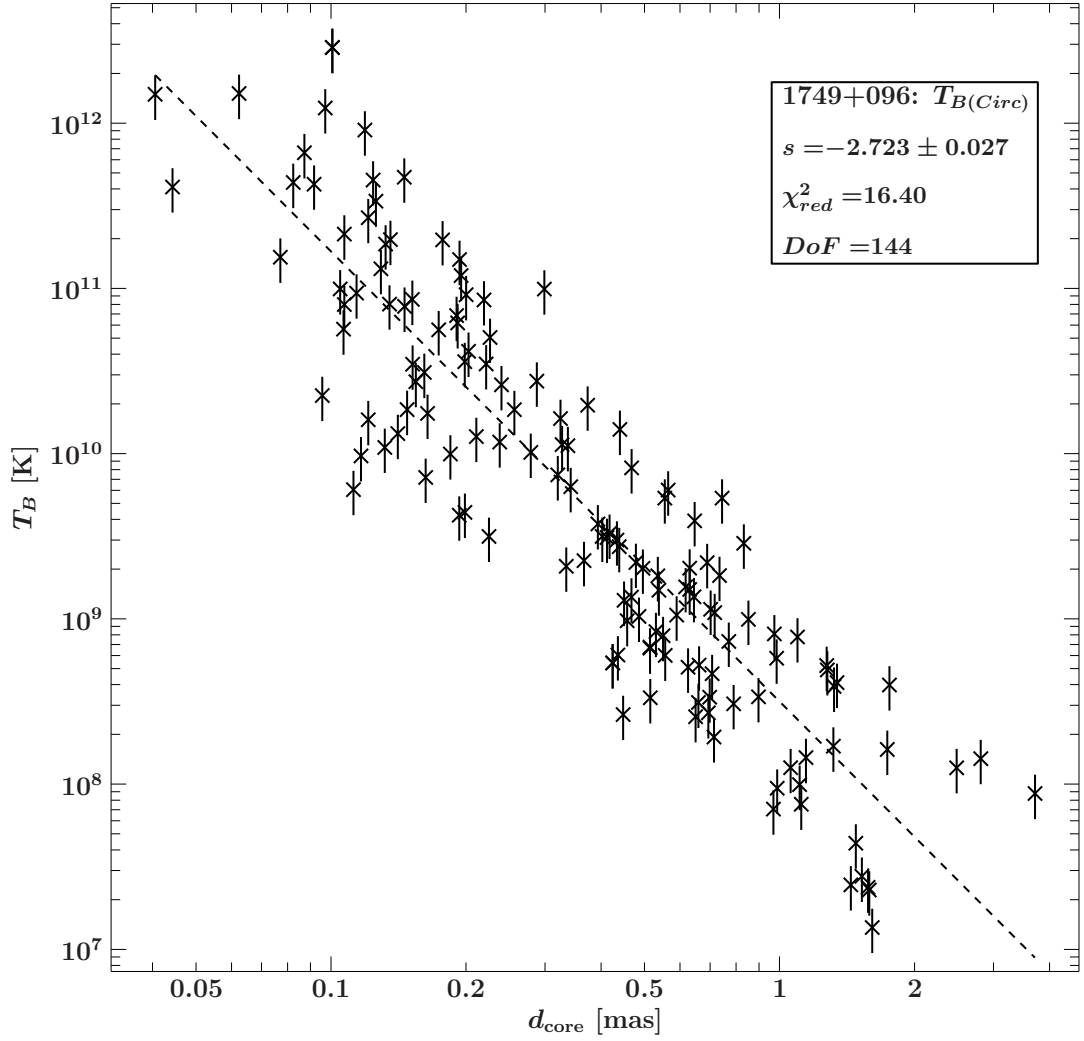


**Figure A.30.:** Brightness temperature gradient of the circular model of 1749+096 fitted with a pure power law, with power law index  $s$ ,  $\chi^2_{red}$ : reduced chi-squared, DoF: Degrees of freedom

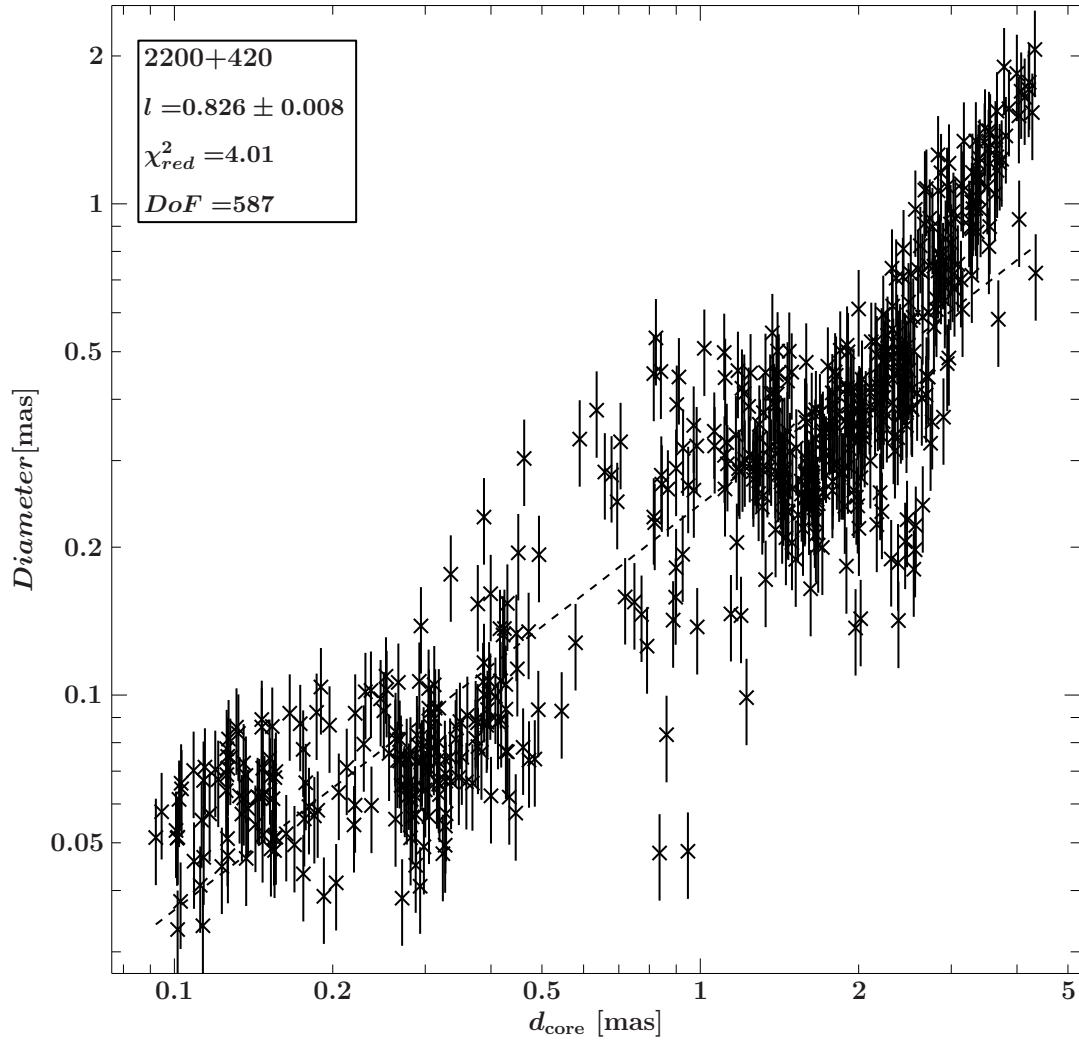


**Figure A.31.:** Diameter gradient of 2200+420 measured at 43 GHz and fitted with a pure power law, with power law index  $l$ ,  $\chi^2_{red}$ : reduced chi-squared, DoF: Degrees of freedom

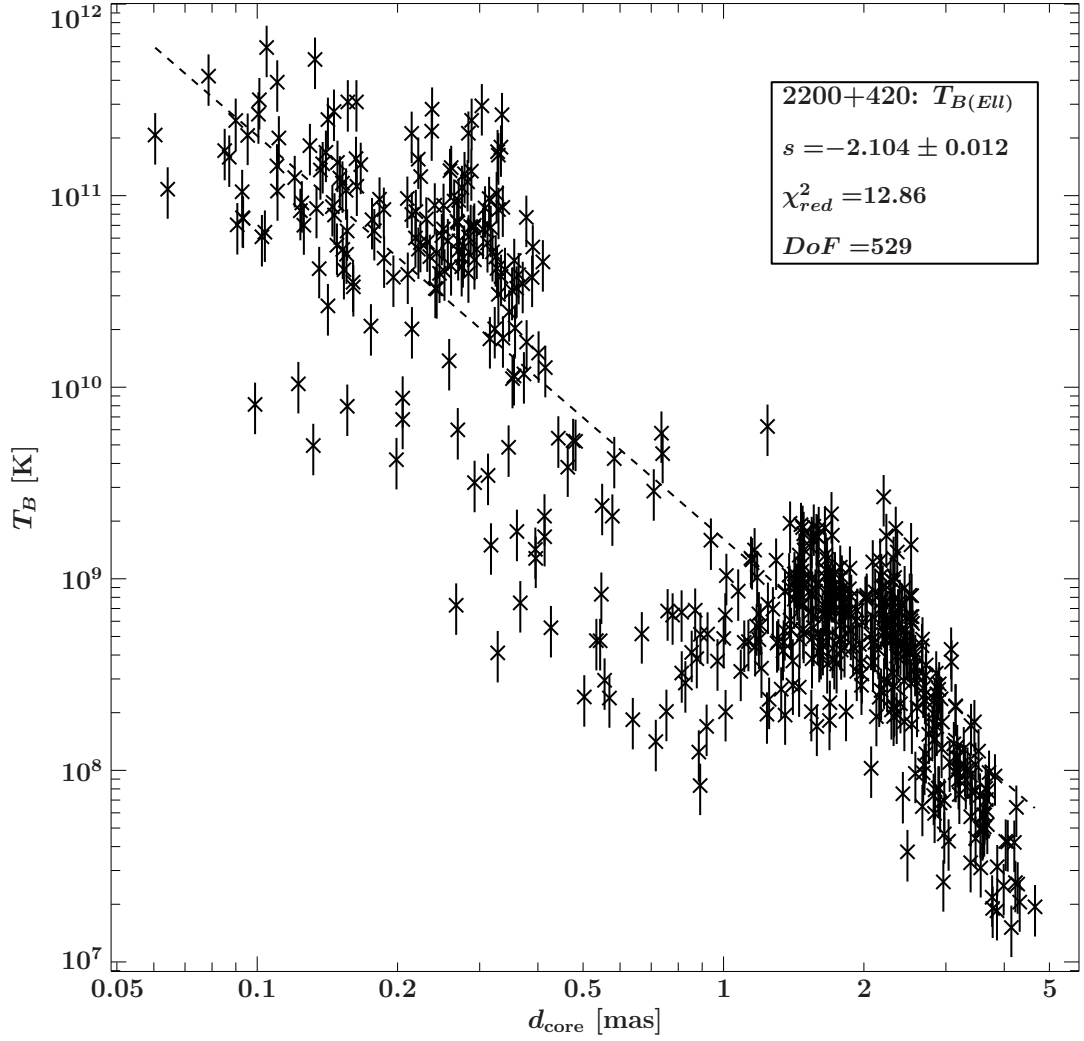


**Figure A.32.:** Brightness temperature gradient of the elliptical model of 2200+420 measured at 43 GHz and fitted with a pure power law, with power law index  $s$ ,  $\chi^2_{red}$ : reduced chi-squared, DoF: Degrees of freedom

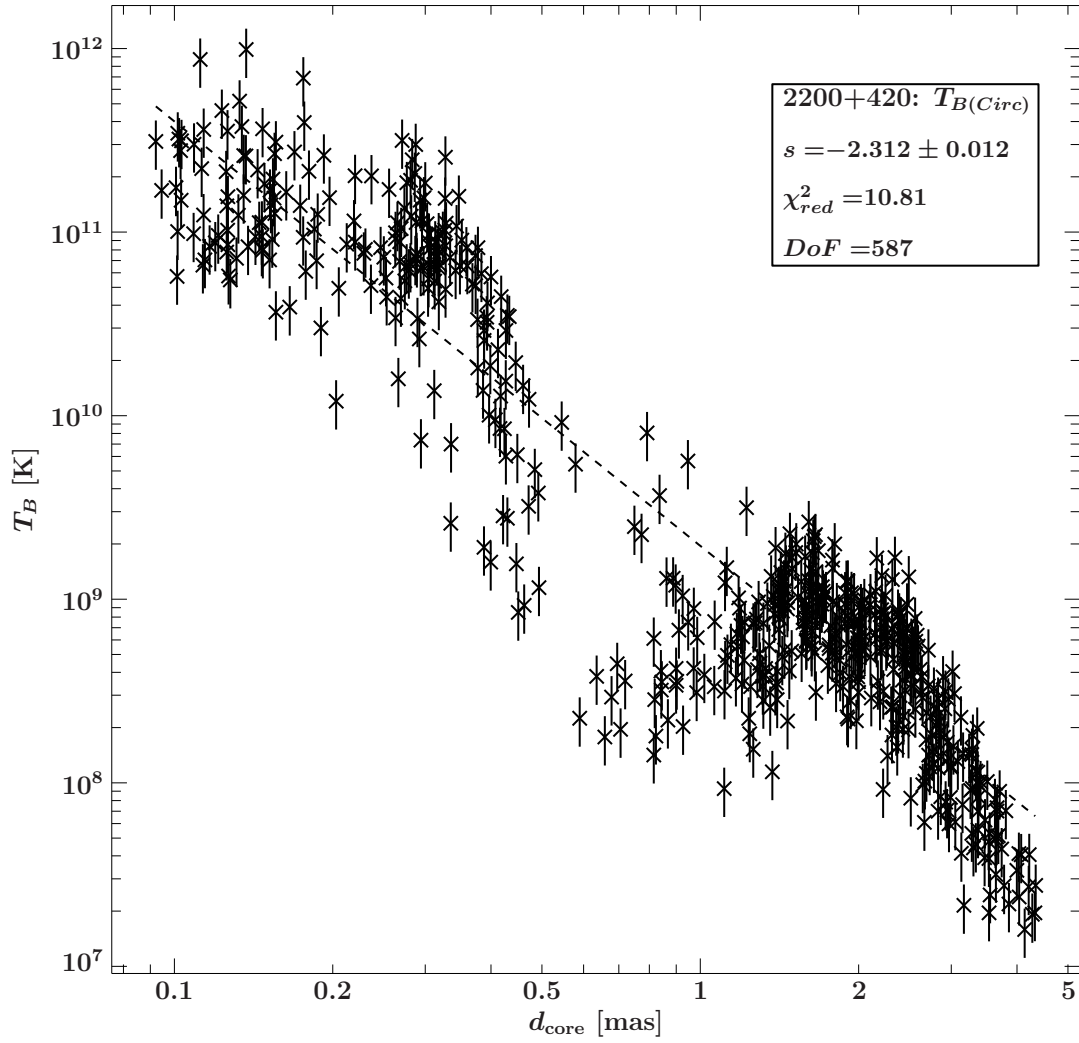


**Figure A.33.:** Brightness temperature gradient of the circular model of 2200+420 measured at 43 GHz and fitted with a pure power law, with power law index  $s$ ,  $\chi^2_{red}$ : reduced chi-squared, DoF: Degrees of freedom

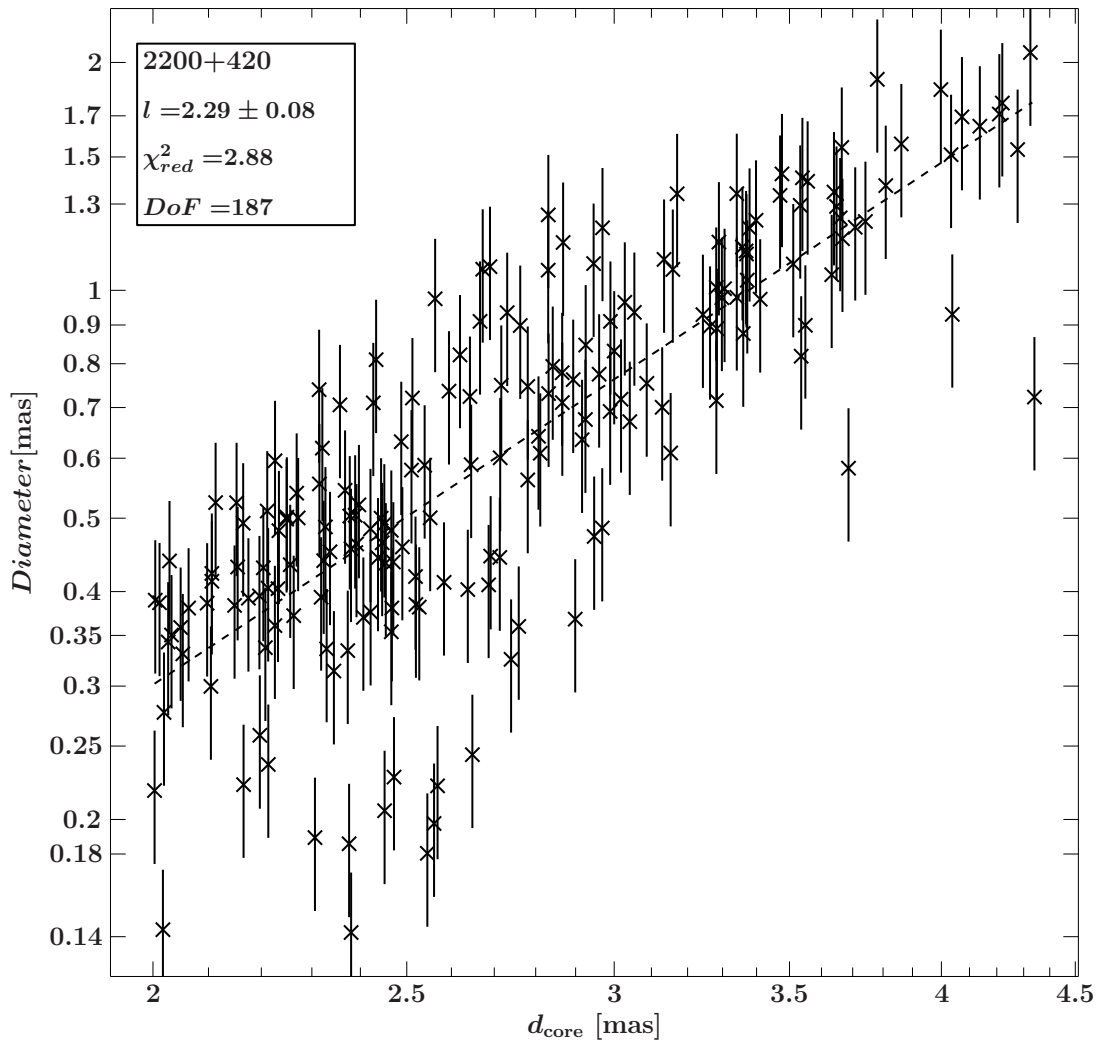


**Figure A.34.:** Diameter gradient of 2200+420 measured at 43 GHz starting at c distance 2mas and fitted with a pure power law, with power law index  $l$ ,  $\chi^2_{\text{red}}$ : reduced chi-squared, DoF: Degrees of freedom

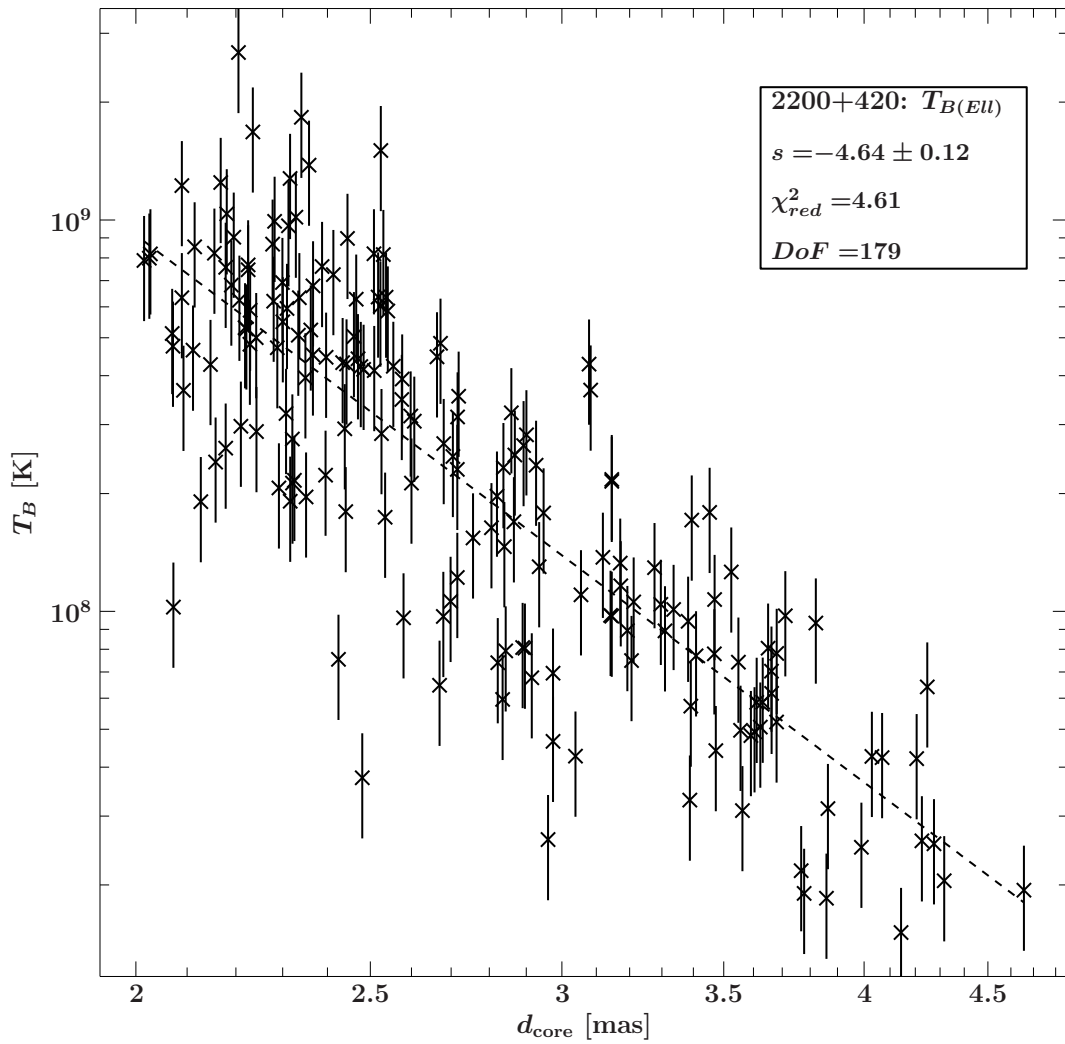


**Figure A.35.:** Brightness temperature gradient starting of the elliptic model of 2200+420 starting at c distance 2mas fitted with a pure power law, with power law index  $s$ ,  $\chi^2_{red}$ : reduced chi-squared, DoF: Degrees of freedom

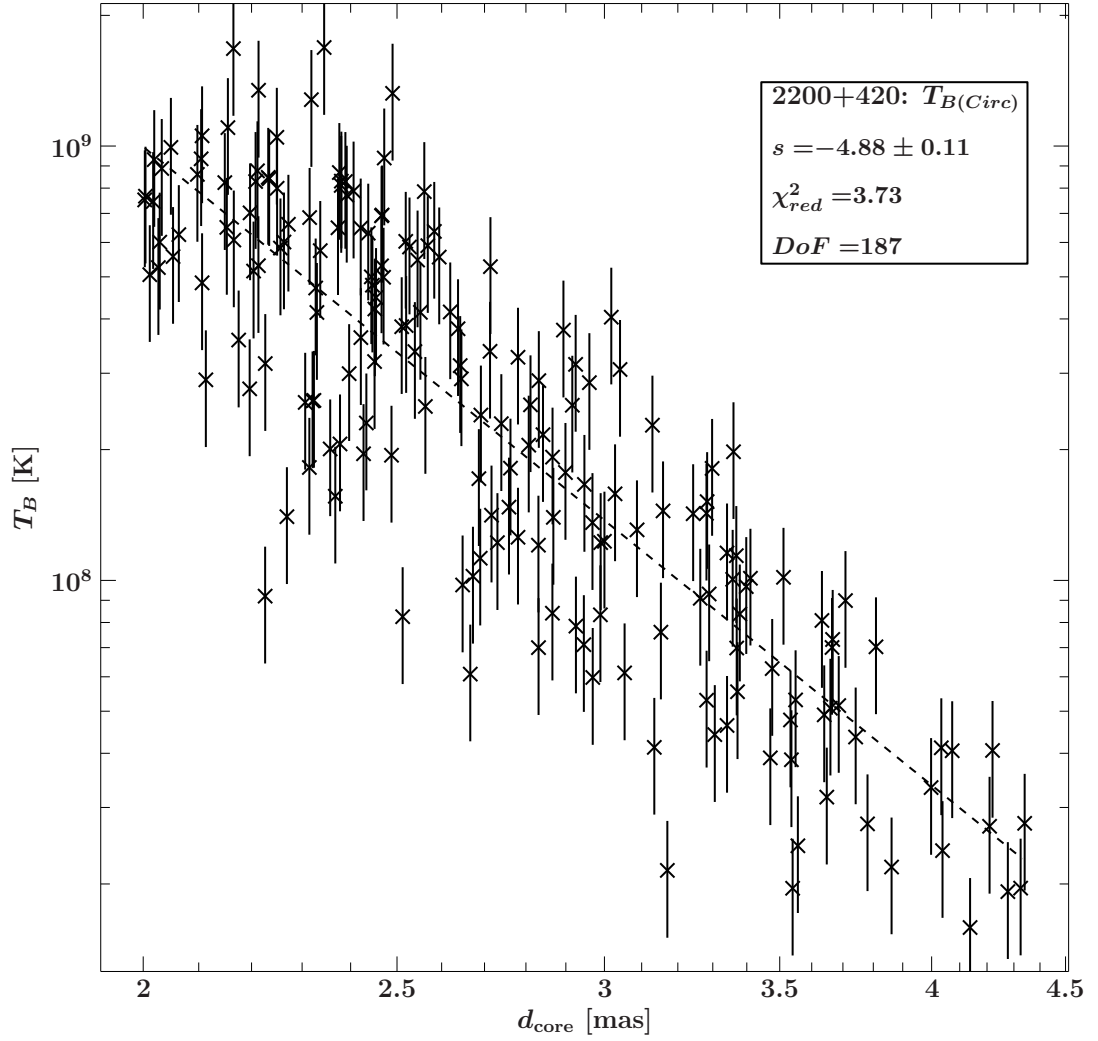


**Figure A.36.:** Brightness temperature gradient of the circular model of 2200+420 starting at c distance 2mas fitted with a pure power law, with power law index  $s$ ,  $\chi^2_{red}$ : reduced chi-squared, DoF: Degrees of freedom

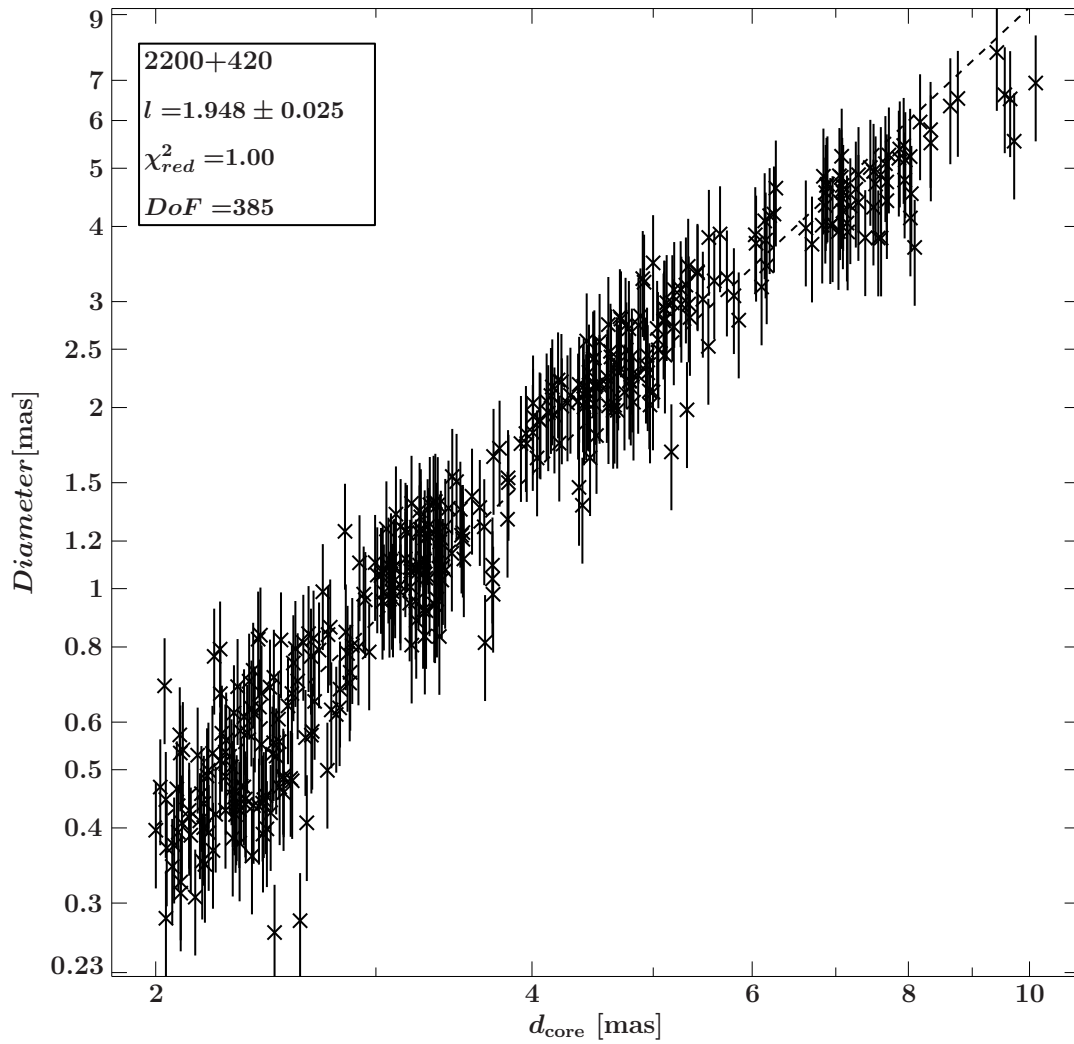


**Figure A.37.:** Diameter gradient of 2200+420, measured at 15GHz and modelfitted by Till Steinbring, starting at core distance of 2 mas fitted with a pure power law, with power law index  $l$ ,  $\chi^2_{red}$ : reduced chi-squared, DoF: Degrees of freedom

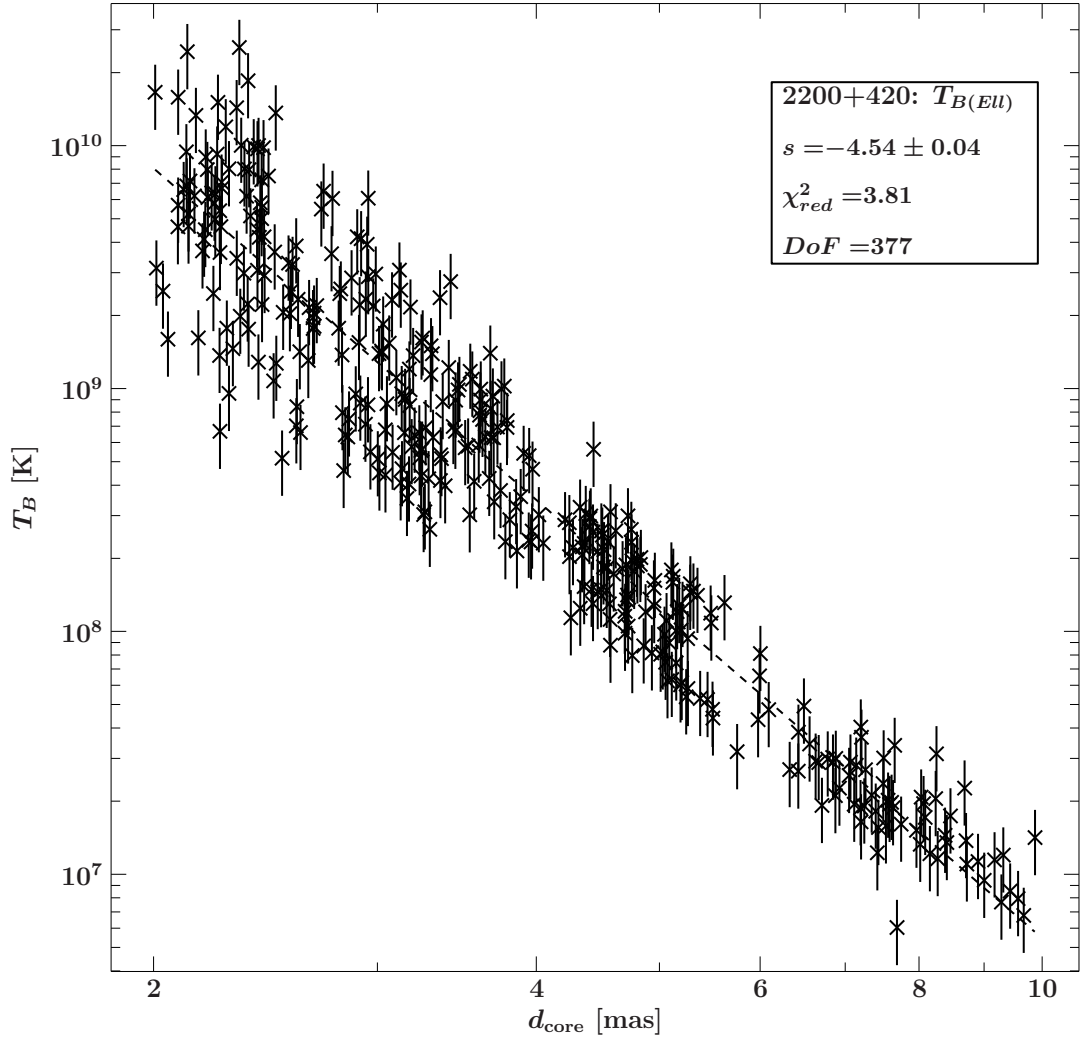


**Figure A.38.:** Brightness temperature gradient of the elliptical model of 2200+420, measured at 15GHz and model-fitted by Till Steinbring, starting at  $c$  distance 2mas fitted with a pure power law, with power law index  $s$ ,  $\chi_{red}^2$ : reduced chi-squared, DoF: Degrees of freedom

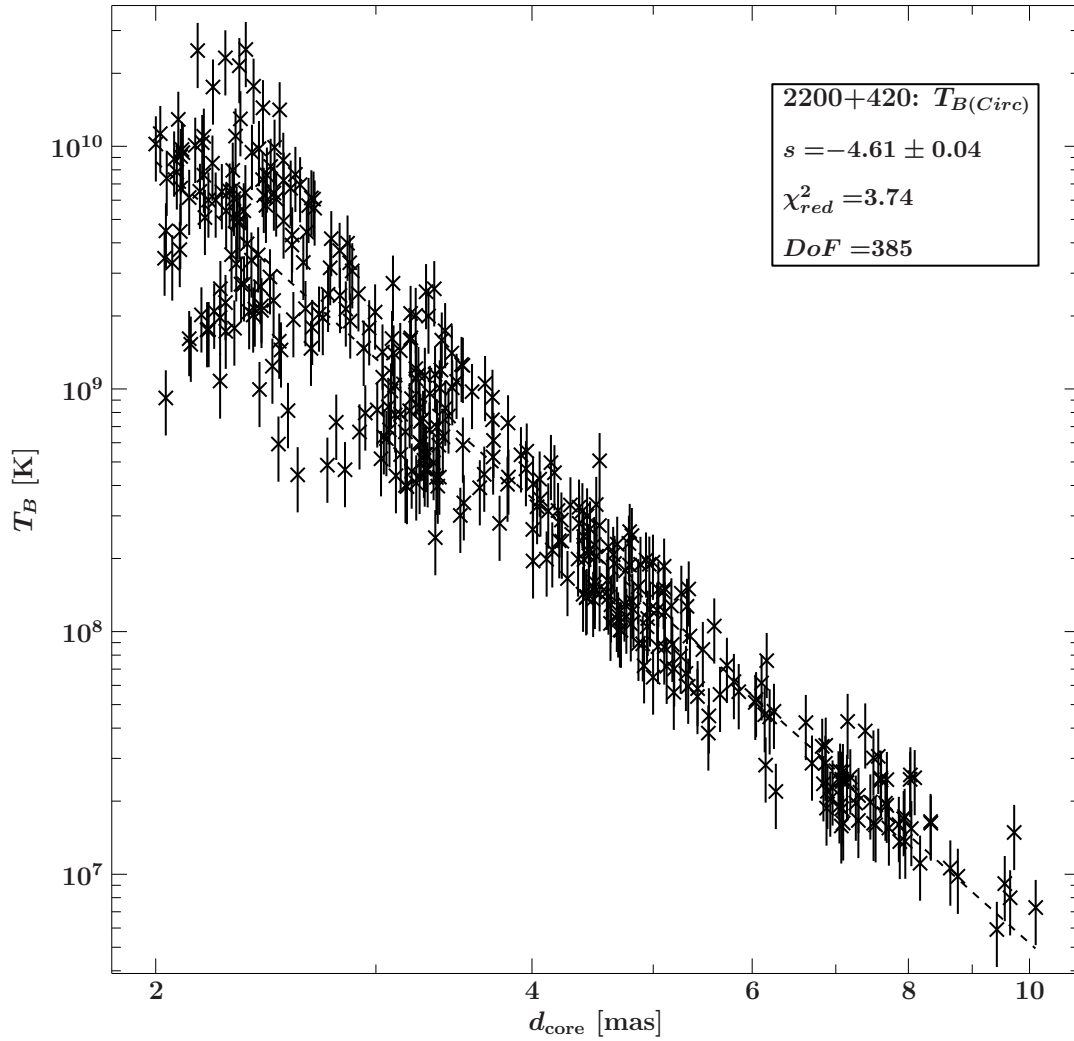


**Figure A.39.:** Brightness temperature gradient of the circular model of 2200+420, measured at 15GHz and model-fitted by Till Steinbring, starting at  $c$  distance 2mas fitted with a pure power law, with power law index  $s$ ,  $\chi^2_{red}$ : reduced chi-squared, DoF: Degrees of freedom

## A.2. Tables

**Table A.1.:** the first 10 components of 0219+428 for the circular model and elliptical model are listed with model type, the date (yyyy-mm-dd), core distance, brightness temperature, diameter. The whole table is saved as a digital version

Model type	Date	$d_{core}$ (mas)	$T_b$ (K)	Major axis (mas)
circular	0	0.00E+000	1.77E+011	3.89E-002
	2008-10-22	2.20E+000	1.82E+008	3.59E-001
		1.47E-001	1.35E+010	9.39E-002
		1.47E+000	1.49E+008	3.03E-001
		8.59E-001	5.60E+008	2.09E-001
		4.32E-001	1.90E+009	1.71E-001
		2.58E+000	5.59E+007	5.93E-001
		1.83E+000	1.12E+008	2.45E-001
	2008-10-25	0.00E+000	1.18E+011	4.79E-002
		1.67E-001	2.11E+010	6.67E-002
elliptical	2008-10-22	2.01E+000	1.38E+008	1.10E+000
		0.00E+000	5.06E+022	6.17E-008
		9.76E-002	1.33E+010	1.93E-001
		7.45E-001	3.91E+008	7.59E-001
		4.12E-001	1.26E+009	2.14E-001
		2.35E+000	4.10E+008	1.75E-001
		2.52E+000	9.45E+007	1.79E+000
	2008-10-25	0.00E+000	2.19E+022	9.77E-008
		1.23E-001	1.44E+010	1.97E-001
	6.32E-001	5.86E+009	3.94E-002	

**Table A.2.:** the first 10 components of 0716+714 for the circular model and elliptical model are listed with model type, the date (yyyy-mm-dd), core distance, brightness temperature, diameter. The whole table is saved as a digital version

Model type	Date	$d_{core}$ (mas)	$T_b$ (K)	Major axis (mas)
circular	0	1.21E+000	4.87E+008	1.96E-001
	2007-06-14	1.39E-001	1.79E+010	7.90E-002
		0.00E+000	6.47E+012	1.40E-002
		0.00E+000	6.18E+011	4.34E-002
	2007-07-12	0.00E+000	6.18E+011	4.34E-002
	2007-08-06	5.75E-001	8.39E+008	1.30E-001
		1.16E-001	1.36E+010	8.13E-002
		0.00E+000	1.48E+012	2.41E-002
	2007-08-30	4.22E-001	1.35E+008	4.48E-001
		1.35E-001	5.63E+010	3.38E-002
0.00E+000		2.74E+012	2.00E-002	
elliptical	2007-06-14	1.22E+000	4.61E+008	2.00E-001
		1.31E-001	1.98E+010	1.46E-001
		0.00E+000	8.46E+013	3.85E-003
	2007-07-12	5.80E-001	7.70E+008	1.28E-001
		3.83E-002	1.41E+010	1.98E-001
		0.00E+000	1.58E+026	2.18E-009
	2007-08-06	1.29E+000	5.21E+007	2.43E+000
		0.00E+000	2.11E+024	2.21E-008
		9.34E-002	2.17E+010	1.57E-001
	2007-08-30	5.59E-001	1.25E+009	1.67E-001

**Table A.3.:** the first 10 components of 0735+178 for the circular model and elliptical model are listed with model type, the date (yyyy-mm-dd), core distance, brightness temperature, diameter. The whole table is saved as a digital version

Model type	Date	$d_{core}$ (mas)	$T_b$ (K)	Major axis (mas)
circular	2007-06-13	0.00E+000	3.12E+010	1.08E-001
	2007-07-12	0.00E+000	1.11E+010	1.68E-001
		2.07E+000	6.09E+007	1.47E+000
		1.21E+000	2.85E+009	8.97E-002
		4.66E-001	1.07E+009	1.94E-001
		0.00E+000	1.72E+010	1.26E-001
	2007-08-30	0.00E+000	6.43E+009	2.23E-001
	2007-09-29	3.29E-001	2.45E+009	2.15E-001
		0.00E+000	1.79E+010	1.15E-001
	2007-11-01	3.64E+000	1.50E+007	1.34E+000
elliptical	2007-06-13	0.00E+000	1.11E+010	2.62E-001
	2007-07-12	2.27E+000	7.40E+007	1.99E+000
		1.01E+000	6.01E+008	9.76E-001
		4.55E-001	1.18E+010	5.18E-002
		0.00E+000	3.11E+010	1.43E-001
	2007-08-30	0.00E+000	6.90E+009	2.45E-001
	2007-09-29	3.27E-001	2.15E+009	2.89E-001
		0.00E+000	1.90E+010	1.11E-001
	2007-11-01	1.02E+000	2.18E+008	2.75E-001
		4.14E-001	5.43E+008	3.16E-001

**Table A.4.:** the first 10 components of 0829+046 for the circular model and elliptical model are listed with model type, the date (yyyy-mm-dd), core distance ( $d_{core}$ ), brightness temperature ( $T_b$ ), diameter. The whole table is saved as a digital version

Model type	Date	$d_{core}$ (mas)	$T_b$ (K)	Major axis (mas)
circular	2007-06-13	7.84E-001	5.87E+010	4.30E-002
		0.00E+000	5.71E+010	8.31E-002
	2007-07-12	8.96E-001	6.73E+008	2.24E-001
		0.00E+000	1.10E+011	5.31E-002
	2007-08-06	8.87E-001	3.08E+008	3.19E-001
		0.00E+000	1.65E+011	4.03E-002
	2007-08-30	8.19E-001	1.97E+008	5.63E-001
		0.00E+000	1.45E+010	1.48E-001
	2007-09-29	1.71E+000	1.52E+008	5.15E-001
		9.08E-001	1.76E+009	1.49E-001
elliptical	2007-06-13	7.84E-001	2.01E+010	7.39E-002
		0.00E+000	3.78E+010	1.81E-001
	2007-07-12	8.60E-001	2.29E+008	7.24E-001
		0.00E+000	4.92E+011	2.32E-002
	2007-08-06	1.98E+000	8.85E+007	1.43E+000
		9.02E-001	1.78E+009	1.45E-001
		4.17E-001	1.10E+009	2.63E-001
		0.00E+000	2.75E+010	9.60E-002
	2007-08-30	6.08E-001	8.60E+007	1.11E+000
		1.68E-001	4.49E+009	1.45E-001

**Table A.5.:** the first 10 components of 0851+202 for the circular model and elliptical model are listed with model type, the date (yyyy-mm-dd), core distance ( $d_{core}$ ), brightness temperature ( $T_b$ ), diameter. The whole table is saved as a digital version

Model type	Date	$d_{core}$ (mas)	$T_b$ (K)	Major axis (mas)
circular	2007-06-14	0.00E+000	1.06E+024	2.71E-008
		1.52E-001	2.48E+009	2.89E-001
		7.44E-001	1.17E+009	1.96E-001
		1.36E+000	3.03E+008	5.00E-001
	2007-07-12	0.00E+000	3.72E+011	4.63E-002
		2.40E-001	1.00E+009	3.95E-001
		7.50E-001	5.85E+008	2.60E-001
		1.18E+000	2.17E+009	1.30E-001
	2007-08-06	0.00E+000	2.05E+025	5.45E-009
		1.91E-001	1.42E+009	3.80E-001
elliptical	2007-06-14	0.00E+000	2.51E+012	1.78E-002
		1.23E-001	2.09E+009	2.64E-001
		4.83E-001	7.71E+008	1.33E+000
		1.37E+000	3.66E+008	3.98E-001
	2007-07-12	0.00E+000	2.77E+014	1.37E-003
		1.31E-001	7.75E+024	5.99E-009
		2.24E-001	1.85E+009	6.47E-001
		1.11E+000	7.60E+008	3.54E-001
	2007-08-06	0.00E+000	2.66E+011	1.79E-001
		2.63E-001	7.18E+009	1.12E-001

**Table A.6.:** the first 10 components of 0954+658 for the circular model and elliptical model are listed with model type, the date (yyyy-mm-dd), core distance ( $d_{core}$ ), brightness temperature ( $T_b$ ), diameter. The whole table is saved as a digital version

Model type	Date	$d_{core}$ (mas)	$T_b$ (K)	Major axis (mas)
circular	2007-06-14	0.00E+000	2.34E+011	4.96E-002
		3.19E-001	3.37E+009	2.45E-001
	2007-07-12	0.00E+000	9.63E+011	2.83E-002
		2.47E-001	3.11E+010	4.17E-002
		4.47E-001	5.67E+009	1.26E-001
	2007-08-06	0.00E+000	1.67E+012	2.20E-002
		1.18E-001	1.11E+010	7.36E-002
		4.14E-001	3.55E+009	1.21E-001
		5.88E-001	3.56E+009	7.94E-002
	2007-08-30	0.00E+000	6.84E+011	3.83E-002
elliptical	2007-06-14	0.00E+000	2.42E+024	1.37E-008
		1.84E-001	7.69E+009	4.60E-001
		5.46E-001	9.57E+008	7.84E-001
	2007-07-12	0.00E+000	1.82E+012	2.04E-002
		3.43E-001	5.07E+009	3.72E-001
	2007-08-06	0.00E+000	2.60E+012	3.60E-002
		1.00E-001	4.89E+009	1.50E-001
		3.59E-001	6.68E+010	1.80E-002
		5.13E-001	2.77E+009	2.53E-001
	2007-08-30	0.00E+000	6.84E+011	3.83E-002

**Table A.7.:** the first 10 components of 1055+018 for the circular model and elliptical model are listed with model type, the date (yyyy-mm-dd), core distance ( $d_{core}$ ), brightness temperature ( $T_b$ ), diameter. The whole table is saved as a digital version

Model type	Date	$d_{core}$ (mas)	$T_b$ (K)	Major axis (mas)	
circular	2011-08-23	0.00E+000	2.96E+011	1.45E-001	
		2.02E+000	4.75E+008	4.67E-001	
	2011-10-16	1.27E+000	6.06E+009	8.64E-002	
		1.91E-001	1.22E+010	1.25E-001	
		0.00E+000	1.36E+012	5.44E-002	
		1.24E-001	2.01E+011	1.14E-001	
		5.41E-001	4.33E+008	7.35E-001	
		1.94E+000	3.48E+008	5.90E-001	
	2012-01-27	0.00E+000	1.32E+012	5.07E-002	
		1.34E-001	1.78E+011	9.96E-002	
elliptical	2011-08-23	0.00E+000	3.92E+011	1.61E-001	
		0	1.96E+000	6.90E+008	3.82E-001
	2011-10-16	1.23E+000	2.36E+009	1.59E-001	
		1	0.00E+000	8.44E+011	9.32E-002
		1	1.25E-001	2.03E+011	1.17E-001
		1	2.28E-001	9.60E+008	1.27E+000
		1	1.97E+000	3.63E+008	7.47E-001
		2012-01-27	0.00E+000	1.44E+012	7.32E-002
	2	1.22E-001	2.58E+011	1.32E-001	
	2	1.93E+000	8.67E+008	6.25E-001	

**Table A.8.:** the first 10 components of 1101+384 for the circular model and elliptical model are listed with model type, the date (yyyy-mm-dd), core distance ( $d_{core}$ ), brightness temperature ( $T_b$ ), diameter. The whole table is saved as a digital version

Model type	Date	$d_{core}$ (mas)	$T_b$ (K)	Major axis (mas)
circular	2010-02-11	0.00E+000	8.32E+010	3.35E-002
		3.94E-001	3.21E+008	1.86E-001
	2010-03-06	0.00E+000	1.84E+010	8.85E-002
		6.32E-001	7.43E+007	4.67E-001
	2010-04-07	0.00E+000	6.43E+009	1.44E-001
		2.09E-001	9.15E+007	6.16E-001
		1.33E+000	1.80E+007	8.84E-001
	2010-04-10	2.89E+000	1.88E+008	2.12E-001
		0.00E+000	1.16E+010	1.02E-001
		4.36E-001	2.33E+008	2.31E-001
elliptical	2010-02-11	0.00E+000	8.22E+010	3.37E-002
		3.95E-001	3.23E+008	2.02E-001
	2010-03-06	0.00E+000	2.18E+010	8.04E-002
		5.97E-001	5.22E+007	1.04E+000
	2010-04-07	0.00E+000	7.49E+009	1.52E-001
		1.86E-001	3.13E+008	7.28E-001
		1.13E+000	2.18E+007	1.95E+000
	2010-04-10	2.93E+000	1.49E+008	2.36E-001
		0.00E+000	1.30E+010	9.79E-002
		2.50E-001	2.02E+008	7.41E-001

**Table A.9.:** the first 10 components of 1219+285 for the circular model and elliptical model are listed with model type, the date (yyyy-mm-dd), core distance ( $d_{core}$ ), brightness temperature ( $T_b$ ), diameter. The whole table is saved as a digital version

Model type	Date	$d_{core}$ (mas)	$T_b$ (K)	Major axis (mas)	
circular	2010-04-07	9.05E-001	7.39E+007	5.28E-001	
		3.18E-001	9.72E+008	1.13E-001	
		0.00E+000	2.10E+009	1.51E-001	
		1.70E-001	6.55E+009	1.42E-001	
	2010-04-10	1.55E-001	1.36E+008	3.64E-001	
		0.00E+000	1.66E+009	9.94E-002	
		2.64E-001	4.98E+008	2.01E-001	
		2.28E-001	5.61E+009	1.13E-001	
	2010-04-15	1.01E+000	3.24E+009	4.19E-002	
		2.50E-001	6.67E+008	2.40E-001	
elliptical	2010-04-07	9.56E-001	6.47E+008	7.44E-001	
		0	3.15E-001	4.92E+008	1.66E-001
		0	0.00E+000	2.85E+009	1.43E-001
		0	1.59E-001	7.25E+009	1.47E-001
	2010-04-10	2.40E-001	1.48E+009	5.65E-001	
		1	0.00E+000	1.19E+009	1.40E-001
		1	2.69E-001	6.50E+008	1.86E-001
		1	2.39E-001	6.38E+009	1.21E-001
	2010-04-15	9.90E-001	3.58E+009	4.01E-002	
		2	2.04E-001	1.15E+009	3.88E-001

**Table A.10.:** the first 10 components of 1749+096 for the circular model and elliptical model are listed with model type, the date (yyyy-mm-dd), core distance ( $d_{core}$ ), brightness temperature ( $T_b$ ), diameter. The whole table is saved as a digital version

Model type	Date	$d_{core}$ (mas)	$T_b$ (K)	Major axis (mas)	
circular	2009-04-01	7.17E-001	1.09E+009	2.12E-001	
		0.00E+000	6.38E+026	2.09E-009	
		1.41E-001	1.18E+009	4.30E-001	
		1.05E-001	9.92E+010	9.88E-002	
	2009-05-30	4.24E-001	5.41E+008	4.99E-001	
		1.01E-001	2.87E+012	2.44E-002	
		0.00E+000	5.31E+011	5.43E-002	
		4.24E-001	5.41E+008	4.99E-001	
		1.01E-001	2.87E+012	2.44E-002	
		0.00E+000	5.31E+011	5.43E-002	
elliptical	2009-04-01	6.24E-001	5.38E+008	3.11E-001	
		0	0.00E+000	3.78E+026	2.72E-009
		0	1.30E-001	1.15E+009	5.80E-001
		0	1.04E-001	1.01E+011	9.75E-002
	2009-05-30	4.24E-001	5.41E+008	4.99E-001	
		1	1.01E-001	2.87E+012	2.44E-002
		1	0.00E+000	5.31E+011	5.43E-002
	2009-07-27	7.22E-001	1.10E+009	1.99E-001	
		0.00E+000	7.65E+011	1.06E-001	
	2009-09-16	4.77E-001	7.45E+008	2.05E-001	

**Table A.11.:** the first 10 components of 2200+420 for the circular model and elliptical model are listed with model type, the date (yyyy-mm-dd), core distance ( $d_{core}$ ), brightness temperature ( $T_b$ ), diameter. The whole table is saved as a digital version

Model type	Date	$d_{core}$ (mas)	$T_b$ (K)	Major axis (mas)
circular	2007-06-14	0.00E+000	3.10E+011	7.26E-002
		2.47E-001	8.22E+010	9.82E-002
		1.22E+000	3.16E+009	9.88E-002
		2.01E+000	5.06E+008	3.87E-001
		1.52E+000	1.80E+009	1.89E-001
	2007-07-13	2.99E+000	8.33E+007	6.92E-001
		2.03E-001	1.20E+010	4.15E-002
		0.00E+000	5.14E+027	5.77E-010
		1.26E-001	3.55E+011	5.10E-002
		2.88E-001	3.00E+011	4.50E-002
elliptical	2007-06-14	0.00E+000	2.54E+011	1.11E-001
		2.40E-001	8.92E+010	1.59E-001
		1.24E+000	6.24E+009	5.91E-002
		1.69E+000	7.96E+008	7.50E-001
		2.82E+000	7.39E+007	8.39E-001
	2007-07-13	2.05E-001	6.78E+009	4.58E-002
		0.00E+000	2.24E+026	2.57E-009
		1.10E-001	3.92E+011	8.06E-002
		2.88E-001	2.47E+011	5.15E-002
		8.92E-001	5.13E+008	2.16E-001

# List of Figures

1.1.	The figure shows the Fanaroff Riley Class 1 object 3C 272P1 observed with the VLA at a wavelength of 6 cm. The data were imaged by Laing & Bridle (1987). Here the red color describes high flux and blue one low flux. One can regard the high flux in the core (red) and the plumes at the end of the jet (blue) . . . . .	6
1.2.	The figure shows the Fanaroff Riley Class 2 object 3C 175 observed 1996 with the VLA at a wavelength of 6 cm and a resolution of 0.35 arcsec. Image courtesy of NRAO/AUI and investigated by Bridle et al. (1994). One can regard the bright lobes at the end of the jet and one narrow jet . . . . .	7
1.3.	shows the Unification model by Urry & Padovani (1995) with modifications from Matthias Kadler. The upper part illustrate the case of a radio loud AGN and the lower side shows a radio quiet AGN. Here BH is the black hole, BLR is the broad line region, NLR means the narrow line region, Sey1 and Sey2 are the Seyfert 1 and Seyfert 2 galaxies, BLRG and NLRG are the broad line and narrow line radio galaxies . . . . .	9
1.4.	Figure 6.2. from Rybicki & Lightman (1979), beamed radiation of synchrotron radiation . . . . .	12
1.5.	Figure 5.2 of Burke & Graham-Smith (2010). Here the geometry of a two element Michelson interferometer is presented. $b_\lambda$ is the baseline between the two telescopes normalized with respect to the observed wavelength. $S$ is the vector pointing in the source direction, $\tau_g$ is the geometrical path delay. The delay box represents an additional delay $\tau_i$ , which can insert technical in the signal circuit. . . . .	20
1.6.	Figure 5.5 of Burke & Graham-Smith (2010). Here the relationship of an interferometer, a source on the sky and the u,v-plane is demonstrated. $x,y$ are the coordinate components of the offset vector $\sigma$ to the source center, with $x$ parallel to $u$ . NCP is the north celestial pole. $w$ is parallel to $S$ . . . . .	20
2.1.	Her a random picked image of each considered source of my sample is pictured with its name and the date of observation. Dec is the declination and RA is the right ascension. The images were taken from the homepage of Boston University Blazar group ( <a href="http://www.bu.edu/blazars/VLBAproject.html">http://www.bu.edu/blazars/VLBAproject.html</a> ) . . . . .	26

2.2.	residual maps for the several fitting steps including the fitted circular components. The time line is from left to right . . . . .	27
2.3.	Clean map of 2200+420 for the epoch 2012-07-05, with the fitted model components . . . . .	28
3.1.	The brightness temperature gradients for all considered sources of my sample are shown. The brightness temperature gradient is fitted using elliptical components. All gradients were measured at 43 GHz and were fitted assuming a pure power law with a power law index $s_{ell}$ . . . . .	31
3.2.	The brightness temperature gradients for all considered sources of my sample are shown. The brightness temperature gradient is fitted using circular components. All gradients were measured at 43 GHz and were fitted assuming a pure power law with a power law index $s_{circ}$ . . . . .	32
3.3.	The diameter gradients for all considered sources of my sample are shown. The diameter gradient is fitted using circular components. All gradients were measured at 43 GHz and were fitted assuming a pure power law with a power law index $l$ . . . . .	33
3.4.	The distribution of the power law index $l$ is pictured. The binning is 0.25	34
3.5.	The distribution of the power law index $s_{circ}$ is pictured. The binning is 0.5 . . . . .	35
3.6.	The distribution of the power law index $s_{ell}$ is pictured. The binning is 0.5	36
3.7.	From left to right: The first plot shows the fitted diameter gradient measured at 43 GHz, the second the diameter gradient measured at 43 GHz, here the excess at $\approx 2.5$ mas is excluded. The third shows the fitted brightness temperature gradient for the elliptic model with the excess and the fourth without the excess, both measured at 43 GHz. The fifth plot shows the fitted brightness temperature gradient for the circular model with the excess and the sixth without the excess, both measured at 43 GHz. Picture 7 shows the fitted diameter gradient, picture 8 the brightness temperature gradient for the elliptical model and picture 9 the brightness temperature gradient for the circular model, all measured at 15 GHz and model fitted by Till Steinbring. The excess in the brightness temperature gradient as well as the dip in the gradient of the diameter at $\approx 2.5$ mas can clearly be seen at both frequencies . . . . .	39
3.8.	Stacked image of 0219+428. The data are taken from the MOJAVE homepage ( <a href="http://www.physics.purdue.edu/MOJAVE/allsources.html">http://www.physics.purdue.edu/MOJAVE/allsources.html</a> ). The stacked image was generated with a stack of 21 15 GHz epochs between 2003-06-21 and 2013-8-12. The intensity is color coded. . . . .	40

---

3.9.	The plot shows the separation from the radio core as a function of the time of individual epochs with a linear fit for each component. The pink data points and the pink line illustrate the separation of a slowly moving component at around 2 mas that could for our purpose be treated as a stationary feature. This might explain the excess in the brightness temperature gradient as well as the dip in the diameter gradient. The tracking analyzes were done with 15 GHz VLBI data of the MOJAVE sample and was taken from the MOJAVE homepage ( <a href="http://www.physics.purdue.edu/MOJAVE/allsources.html">http://www.physics.purdue.edu/MOJAVE/allsources.html</a> ).	41
3.10.	From left to right. The first three plots include the power law fits of the diameter gradient and the two brightness temperature gradients measured at 43 GHz. The second three plots include the power law fits of the diameter gradient and the two brightness temperature gradients all started at $d_{core} = 2$ mas and measured at 43 GHz. The last three plots include the power law fits of the diameter gradient and the two brightness temperature gradients all started at $d_{core} = 2$ mas and measured at 15 GHz, model fitted by Till Steinbring.	43
3.11.	Stacked image of 2200+420. The data are taken from the MOJAVE homepage ( <a href="http://www.physics.purdue.edu/MOJAVE/allsources.html">http://www.physics.purdue.edu/MOJAVE/allsources.html</a> ). The stacked image was generated with a stack of 125 epochs between 1995-04-07 and 2013-8-20. The intensity is color coded.	44
A.1.	Diameter gradient, measured at 43GHz of 0219+428 fitted with a pure power law included excess, with power law index 1, $\chi_{red}^2$ : reduced chi-squared, DoF: Degrees of freedom	47
A.2.	Diameter gradient, measured at 43GHz of 0219+428 fitted with a pure power law excluded excess, with power law index 1, $\chi_{red}^2$ : reduced chi-squared, DoF: Degrees of freedom	48
A.3.	Brightness temperature gradient of the elliptic model, measured at 43GHz of 0219+428 fitted with a pure power law included excess, with power law index s, $\chi_{red}^2$ : reduced chi-squared, DoF: Degrees of freedom	49
A.4.	Brightness temperature gradient of the elliptic model, measured at 43GHz of 0219+428 fitted with a pure power law excluded excess, with power law index s, $\chi_{red}^2$ : reduced chi-squared, DoF: Degrees of freedom	50
A.5.	Brightness temperature gradient of the circular model, measured at 43GHz of 0219+428 fitted with a pure power law included excess, with power law index s, $\chi_{red}^2$ : reduced chi-squared, DoF: Degrees of freedom	51
A.6.	Brightness temperature gradient of the circular model, measured at 43GHz of 0219+428 fitted with a pure power law excluded excess, with power law index s, $\chi_{red}^2$ : reduced chi-squared, DoF: Degrees of freedom	52

A.7. Diameter gradient, measured at 15GHz of 0219+428 fitted with a pure power law included excess, with power law index l by Till Steinbring, $\chi_{red}^2$ : reduced chi-squared, DoF: Degrees of freedom . . . . .	53
A.8. Brightness temperature gradient of the elliptic model, measured at 15GHz of 0219+428 fitted with a pure power law included excess by Till Steinbring, with power law index s, $\chi_{red}^2$ : reduced chi-squared, DoF: Degrees of freedom . . . . .	54
A.9. Brightness temperature gradient of the circular model, measured at 15GHz of 0219+428 fitted with a pure power law included excess by Till Steinbring, with power law index s, $\chi_{red}^2$ : reduced chi-squared, DoF: Degrees of freedom . . . . .	55
A.10. Diameter gradient of 0716+714 fitted with a pure power law, with power law index l, $\chi_{red}^2$ : reduced chi-squared, DoF: Degrees of freedom . . . . .	56
A.11. Brightness temperature gradient of the elliptic model of 0716+714 fitted with a pure power law, with power law index s, $\chi_{red}^2$ : reduced chi-squared, DoF: Degrees of freedom . . . . .	57
A.12. Brightness temperature gradient of the circular model of 0716+714 fitted with a pure power law, with power law index s, $\chi_{red}^2$ : reduced chi-squared, DoF: Degrees of freedom . . . . .	58
A.13. Diameter gradient of 0735+178 fitted with a pure power law, with power law index l, $\chi_{red}^2$ : reduced chi-squared, DoF: Degrees of freedom . . . . .	59
A.14. Brightness temperature gradient of the elliptic model of 0735+178 fitted with a pure power law, with power law index s, $\chi_{red}^2$ : reduced chi-squared, DoF: Degrees of freedom . . . . .	60
A.15. Brightness temperature gradient of the circular model of 0735+178 fitted with a pure power law, with power law index s, $\chi_{red}^2$ : reduced chi-squared, DoF: Degrees of freedom . . . . .	61
A.16. Diameter gradient of 0829+046 fitted with a pure power law, with power law index l, $\chi_{red}^2$ : reduced chi-squared, DoF: Degrees of freedom . . . . .	62
A.17. Brightness temperature gradient of the elliptic model of 0829+046 fitted with a pure power law, with power law index s, $\chi_{red}^2$ : reduced chi-squared, DoF: Degrees of freedom . . . . .	63
A.18. Brightness temperature gradient of the circular model of 0829+046 fitted with a pure power law, with power law index s, $\chi_{red}^2$ : reduced chi-squared, DoF: Degrees of freedom . . . . .	64
A.19. Diameter gradient of 0851+202 fitted with a pure power law, with power law index l, $\chi_{red}^2$ : reduced chi-squared, DoF: Degrees of freedom . . . . .	65
A.20. Brightness temperature gradient of the elliptic model of 0851+202 fitted with a pure power law, with power law index s, $\chi_{red}^2$ : reduced chi-squared, DoF: Degrees of freedom . . . . .	66

---

A.21. Brightness temperature gradient of the circular model of 0851+202 fitted with a pure power law, with power law index $s$ , $\chi_{red}^2$ : reduced chi-squared, NDoF: Degrees of freedom . . . . .	67
A.22. Diameter gradient of 0954+658 fitted with a pure power law, with power law index $l$ , $\chi_{red}^2$ : reduced chi-squared, DoF: Degrees of freedom . . . . .	68
A.23. Brightness temperature gradient of the elliptic model of 0954+658 fitted with a pure power law, with power law index $s$ , $\chi_{red}^2$ : reduced chi-squared, DoF: Degrees of freedom . . . . .	69
A.24. Brightness temperature gradient of the circular model of 0954+658 fitted with a pure power law, with power law index $s$ , $\chi_{red}^2$ : reduced chi-squared, DoF: Degrees of freedom . . . . .	70
A.25. Diameter gradient of 1101+384 measured at 43 GHz and fitted with a pure power law, with power law index $l$ , $\chi_{red}^2$ : reduced chi-squared, DoF: Degrees of freedom . . . . .	71
A.26. Brightness temperature gradient of the elliptic model of 1101+384 measured at 43 GHz and fitted with a pure power law, with power law index $s$ , $\chi_{red}^2$ : reduced chi-squared, DoF: Degrees of freedom . . . . .	72
A.27. Brightness temperature gradient of the circular model of 1101+384 measured at 43 GHz and fitted with a pure power law, with power law index $s$ , $\chi_{red}^2$ : reduced chi-squared, DoF: Degrees of freedom . . . . .	73
A.28. Diameter gradient of 1749+096 fitted with a pure power law, with power law index $l$ , $\chi_{red}^2$ : reduced chi-squared, DoF: Degrees of freedom . . . . .	74
A.29. Brightness temperature gradient of the elliptic model of 1749+096 fitted with a pure power law, with power law index $s$ , $\chi_{red}^2$ : reduced chi-squared, DoF: Degrees of freedom . . . . .	75
A.30. Brightness temperature gradient of the circular model of 1749+096 fitted with a pure power law, with power law index $s$ , $\chi_{red}^2$ : reduced chi-squared, DoF: Degrees of freedom . . . . .	76
A.31. Diameter gradient of 2200+420 measured at 43 GHz and fitted with a pure power law, with power law index $l$ , $\chi_{red}^2$ : reduced chi-squared, DoF: Degrees of freedom . . . . .	77
A.32. Brightness temperature gradient of the elliptic model of 2200+420 measured at 43 GHz and fitted with a pure power law, with power law index $s$ , $\chi_{red}^2$ : reduced chi-squared, DoF: Degrees of freedom . . . . .	78
A.33. Brightness temperature gradient of the circular model of 2200+420 measured at 43 GHz and fitted with a pure power law, with power law index $s$ , $\chi_{red}^2$ : reduced chi-squared, DoF: Degrees of freedom . . . . .	79
A.34. Diameter gradient of 2200+420 measured at 43 GHz starting at $c$ distance 2mas and fitted with a pure power law, with power law index $l$ , $\chi_{red}^2$ : reduced chi-squared, DoF: Degrees of freedom . . . . .	80

A.35. Brightness temperature gradient starting of the elliptic model of 2200+420 starting at c distance 2mas fitted with a pure power law, with power law index $s$ , $\chi_{red}^2$ : reduced chi-squared, DoF: Degrees of freedom . . . . .	81
A.36. Brightness temperature gradient of the circular model of 2200+420 starting at c distance 2mas fitted with a pure power law, with power law index $s$ , $\chi_{red}^2$ : reduced chi-squared, DoF: Degrees of freedom . . . . .	82
A.37. Diameter gradient of 2200+420, measured at 15GHz and modelfitted by Till Steinbring, starting at core distance of 2mas fitted with a pure power law, with power law index $l$ , $\chi_{red}^2$ : reduced chi-squared, DoF: Degrees of freedom . . . . .	83
A.38. Brightness temperature gradient of the elliptic model of 2200+420, measured at 15GHz and modelfitted by Till Steinbring, starting at c distance 2mas fitted with a pure power law, with power law index $s$ , $\chi_{red}^2$ : reduced chi-squared, DoF: Degrees of freedom . . . . .	84
A.39. Brightness temperature gradient of the circular model of 2200+420, measured at 15GHz and modelfitted by Till Steinbring, starting at c distance 2mas fitted with a pure power law, with power law index $s$ , $\chi_{red}^2$ : reduced chi-squared, DoF: Degrees of freedom . . . . .	85

# List of Tables

1.1. Overview: Unification Model AGN, by M. Kadler. Here RQ means radio-quiet and RL radio-loud. B stands for broad lines and N for narrow lines.	10
1.2. The canonical values of Blandford & Königl (1979) and Königl (1981) and the expansion with respect to brightness temperature by Kadler et al. (2004)	17
2.1. All sources of the sample with their B1950 name, common name, redshift and reference to the redshift	25
3.1. Power law indices $s_{ell}$ , $s_{circ}$ , $l$ with errors for all considered sources	37
3.2. The mean value the median and the standard deviation of each power law index is listed	37
3.3. Power law indices $s_{ell}$ , $s_{circ}$ , $l$ with $\chi^2_{red}$ and degrees of freedom (DoF) for BL Lac (2200+420), measured at 43 GHz and at 15 GHz using MOJAVE data model fitted by Till Steinbring	45
A.1. the first 10 components of 0219+428 for the circular model and elliptical model are listed with model type, the date (yyyy-mm-dd), core distance, brightness temperature, diameter. The whole table is saved as a digital version	86
A.2. the first 10 components of 0716+714 for the circular model and elliptical model are listed with model type, the date (yyyy-mm-dd), core distance, brightness temperature, diameter. The whole table is saved as a digital version	87
A.3. the first 10 components of 0735+178 for the circular model and elliptical model are listed with model type, the date (yyyy-mm-dd), core distance, brightness temperature, diameter. The whole table is saved as a digital version	88
A.4. the first 10 components of 0829+046 for the circular model and elliptical model are listed with model type, the date (yyyy-mm-dd), core distance ( $d_{core}$ ), brightness temperature ( $T_b$ ), diameter. The whole table is saved as a digital version	89
A.5. the first 10 components of 0851+202 for the circular model and elliptical model are listed with model type, the date (yyyy-mm-dd), core distance ( $d_{core}$ ), brightness temperature ( $T_b$ ), diameter. The whole table is saved as a digital version	90

A.6. the first 10 components of 0954+658 for the circular model and elliptical model are listed with model type, the date (yyyy-mm-dd), core distance ( $d_{core}$ ), brightness temperature ( $T_b$ ), diameter. The whole table is saved as a digital version . . . . .	91
A.7. the first 10 components of 1055+018 for the circular model and elliptical model are listed with model type, the date (yyyy-mm-dd), core distance ( $d_{core}$ ), brightness temperature ( $T_b$ ), diameter. The whole table is saved as a digital version . . . . .	92
A.8. the first 10 components of 1101+384 for the circular model and elliptical model are listed with model type, the date (yyyy-mm-dd), core distance ( $d_{core}$ ), brightness temperature ( $T_b$ ), diameter. The whole table is saved as a digital version . . . . .	93
A.9. the first 10 components of 1219+285 for the circular model and elliptical model are listed with model type, the date (yyyy-mm-dd), core distance ( $d_{core}$ ), brightness temperature ( $T_b$ ), diameter. The whole table is saved as a digital version . . . . .	94
A.10.the first 10 components of 1749+096 for the circular model and elliptical model are listed with model type, the date (yyyy-mm-dd), core distance ( $d_{core}$ ), brightness temperature ( $T_b$ ), diameter. The whole table is saved as a digital version . . . . .	95
A.11.the first 10 components of 2200+420 for the circular model and elliptical model are listed with model type, the date (yyyy-mm-dd), core distance ( $d_{core}$ ), brightness temperature ( $T_b$ ), diameter. The whole table is saved as a digital version . . . . .	96

# Bibliography

- Abazajian K., Adelman-McCarthy J.K., Agüeros M.A., et al., 2005, AJ 129, 1755
- Antonucci R., 1993, ARA&A 31, 473
- Antonucci R.R.J., Miller J.S., 1985, ApJ 297, 621
- Bass M., 1995, Handbook of Optics: Devices, measurements, and properties, Handbook of Optics, McGraw-Hill
- Blandford R.D., Königl A., 1979, ApJ 232, 34
- Blasi M.G., Lico R., Giroletti M., et al., 2013, A&A 559, 11
- Blumenthal G., Gould R., 1970, Rev. Mod. Phys. 42, 237
- Bridle A.H., Hough D.H., Lonsdale C.J., et al., 1994, AJ 108, 766
- Bridle A.H., Perley R.A., 1984, ARA&A 22, 319
- Burd P.R., 2014, Bachelor thesis, Julius-Maximilian-Universität Würzburg
- Burke B.F., Graham-Smith F., 2010, An Introduction to Radio Astronomy, Cambridge University Press
- Fanaroff B.L., Riley J.M., 1974, MNRAS 167, 31P
- Furniss A., Fumagalli M., Danforth C., et al., 2013, ApJ 766, 35
- Ghisellini G., 2011, In: Aharonian F.A., Hofmann W., Rieger F.M. (eds.) American Institute of Physics Conference Series, Vol. 1381. American Institute of Physics Conference Series, p.180
- Kadler M., Ros E., Lobanov, A. P. and Falcke H., Zensus J.A., 2004, A&A 426, 481
- Kellermann K.I., Pauliny-Toth I.I.K., 1969, ApJL 155, L71
- Kellermann K.I., Sramek R., Schmidt M., et al., 1989, AJ 98, 1195
- Königl A., 1981, ApJ 243, 700
- Kovalev Y.Y., Kellermann K.I., Lister M.L., et al., 2005, AJ 130, 2473

- Laing R.A., Bridle A.H., 1987, MNRAS 228, 557
- Lister M.L., Aller H.D., Aller M.F., et al., 2009, AJ 137, 3718
- Mannheim K., 1993, A&A 269, 67
- Nilsson K., Pursimo T., Sillanpää A., et al., 2008, A&A 487, L29
- Nilsson K., Pursimo T., Villforth C., et al., 2012, A&A 547, A1
- Rector T.A., Stocke J.T., 2001, AJ 122, 565
- Rees M.J., 1967, MNRAS 137, 429
- Robson I., 1996, Active galactic nuclei, Wiley-Praxis series in astronomy and astrophysics, Wiley
- Rybicki G.B., Lightman A.P., 1979, Radiative processes in astrophysics, New York, Wiley-Interscience
- Seyfert C.K., 1943, ApJ 97, 28
- Shaw M.S., Romani R.W., Cotter G., et al., 2012, ApJ 748, 49
- Shaw M.S., Romani R.W., Cotter G., et al., 2013, ApJ 764, 135
- Sheikhnezami S., Fendt C., Porth O., et al., 2012, AJ 757, 165
- Stein W.A., Odell S.L., Strittmatter P.A., 1976, ARA&A 14, 173
- Stickel M., Fried J.W., Kuehr H., 1988, A&A 191, L16
- Stickel M., Fried J.W., Kuehr H., 1989, A&AS 80, 103
- Sulentic J.W., Marziani P., Dultzin-Hacyan D., 2000, ARA&A 38, 521
- Taylor G., 1997, The Difmap Cookbook available from <ftp://ftp.astro.caltech.edu/pub/difmap/cookbook.ps.Z>
- Ulrich M.H., Kinman T.D., Lynds C.R., et al., 1975, ApJ 198, 261
- Urry C.M., Padovani P., 1995, PASP 107, 803
- Vermeulen R.C., Ogle P.M., Tran H.D., et al., 1995, ApJL 452, L5
- Williamson K.E., Jorstad S.G., Marscher A.P., et al., 2014, ApJ 789, 20
- Wilson A.S., Colbert E.J.M., 1995, ApJ 438, 62

## Danksagung

An dieser Stelle möchte ich mich ganz herzlich bei all den Leuten bedanken ohne die diese Arbeit niemals möglich gewesen wäre.

Als erstes möchte ich mich bei meinem Betreuer Matthias Kadler bedanken, der mein Interesse in der Vorlesung Atmosphären- und Weltraumphysik für die Arbeit in der Astronomie geweckt hat und dass er mir die Möglichkeit gegeben hat an diesem Projekt zu arbeiten. Seine Vorlesung zu extragalaktischen Jets und die Diskussionen über meine Arbeit haben mich immer inspiriert und motiviert.

Zudem möchte ich mich bei Till Steinbring für die hervorragende Betreuung bedanken und dass ich in diesem Projekt mitarbeiten durfte. Er hat mich sehr gut in das Thema eingeführt und war immer da, wenn ich Fragen hatte.

Außerdem will ich mich bei Paul Burd bedanken, zu dem ich immer kommen konnte, wenn ich Fragen zu dem Projekt hatte Danke für die vielen hilfreichen Diskussionen die mir immer sehr weiter geholfen haben und für die freundschaftliche Unterstützung in dieser Zeit.

Danke auch an Jonas Trüstedt und Robert Schulz, die mir immer bei Problemen mit ISIS und Latex weiter geholfen haben.

Überdies möchte ich mich bei allen Leuten des Lehrstuhls für Astronomie bedanken, die mich immer unterstützt haben und mich hier herzlich aufgenommen hab.

Ganz besonders möchte ich mich auch bei meinen Eltern und meiner Schwester danken die mich in allen Dingen in meinem Studium unterstützen und einfach in jeder Situation für mich da sind.

This study makes use of 43 GHz VLBA data from the VLBA-BU Blazar Monitoring Program (VLBA-BU-BLAZAR; <http://www.bu.edu/blazars/VLBAproject.html>), funded by NASA through the Fermi Guest Investigator Program. The VLBA is an instrument of the National Radio Astronomy Observatory. The National Radio Astronomy Observatory is a facility of the National Science Foundation operated by Associated Universities, Inc.

This research has made use of data from the MOJAVE database that is maintained by the MOJAVE team [Lister et al. \(2009\)](#).

This research has made use of ISIS functions provided by ECAP/Remeis observatory and MIT (<http://www.sternwarte.uni-erlangen.de/isis/>).

## **Selbstständigkeitserklärung**

Der Verfasser erklärt, dass er die vorliegende Arbeit selbständig, ohne fremde Hilfe und ohne Benutzung anderer als der angegebenen Hilfsmittel angefertigt hat. Die aus fremden Quellen (einschließlich elektronischer Quellen) direkt oder indirekt übernommenen Gedanken sind ausnahmslos als solche kenntlich gemacht. Die Arbeit ist in gleicher oder ähnlicher Form oder auszugsweise im Rahmen einer anderen Prüfung noch nicht vorgelegt worden.

---

Würzburg, 22. Dezember 2014